Doctoral program in Environmental Engineering

Universitat Politècnica de Catalunya

Doctoral Thesis

Modeling the dust life cycle and its associated meteorological processes from global to regional scales

Author:

Lluís Vendrell Miguel

Advisor:	Co-advisor:	Tutor:
Dr. Oriol Jorba	**Dr. Sara Basart**	**Dr. María Gonçalves**

Barcelona, November 2017

Per a l'Hannah

“Los caminos más duros dejan cicatrices en el alma,
pero también una bella historia que contar”

Acknowledgements

Firstly, I would like to thank my advisor Dr. Sara Basart. Her infinite patience, feedback, corrections, and advice about my work have been very helpful and necessary during this journey. I thank my thesis advisor Dr. Oriol Jorba and my former thesis advisor Dr. José María Baldasano for helping me with everything that they could. Kim Serradell, Francesc Martínez, and Miguel Castillo were indispensable for the technical support they offered to solve any problem with my desktop, the supercomputer facilities and even errors from model runs. Thanks, also, to Francesco Benincasa for his help in developing my Python scripts.

Special thanks go to my past and present workmates (and lunchmates) from the "Ph.D. area" for their friendship and necessary support: Rubén Cruz, Bianca Mezzina, Aleix Bou, Jaime Benavides, Vincenzo Obiso, Daniel Rodríguez, Niti Mishra, Víctor Valverde, Sama K. Mohammed, Sergio Natan Gonzalez, George Markomanolis, Antonis Gkikas, Michele Spada and Alba Badía. Moreover, of course, thanks to all who have collaborated in this work with comments and corrections such as Florian Pantillon and María Gonçalvez.

I would like to acknowledge the people involved in the AERONET, AMMA, METAR, ISH and PHOTONS for their effort in establishing and maintaining them, as well as the MSG and MODIS mission scientists and associated EUMETSAT and NASA personnel for the production of the data used in this thesis.

Thanks to everyone who worked and are working on the NMMB-MONARCH model for developing the model and contributing to a really useful tool for modeling and forecasting aerosols, particularly Carlos Pérez García-Pando and Oriol Jorba who have put much effort into improving the model in many ways. I thank "the Obra Social Fundación la Caixa" that funded my time at Barcelona Supercomputing Center (BSC) and gave me the opportunity to develop my Ph.D. thesis here. I also acknowledge the contributions of the "Supercomputación and e-ciencia" project (CSD2007-0050) from the Consolider-Ingenio 2010 program, the CICYT project (CGL2013-46736) and Severo Ochoa (SEV-2011-00067) program of the Spanish Government to this work. All model simulations included in the present research manuscript were performed on the MareNostrum supercomputer hosted by BSC.

Finally, I want to thank my parents for supporting all of my decisions, whether good or bad, during this journey and my life in general. I am sorry for not being able to spend time with them due to work, although I am sure that they would forgive me for that. Last, but not least, I want to thank my awesome wife who supported me through everything, even the bad moments and helped me deal with psychological stress. Thanks again to everyone who I named and I apologize to those that I forgot to mention. Goodbye and good luck to everyone!

Abstract

Mineral dust largely contributes to the atmospheric aerosol mass load which affects air quality, human health, socio-economic activities, ecosystems, weather and climate. To better understand the dust cycle processes, which occur in a wide range of spatiotemporal scales, observations and dust numerical models are required. However, ground-based observations remain sparse over dust emission areas. In this framework, dust model results are necessary not only because they complement observations but also because they can simulate or predict the dust cycle. A proper representation of the dust cycle, from dust emission to transport and deposition, requires a better understanding of how models reproduce dust processes and at which scales.

The present Ph.D. thesis **aims to test the ability of a non-hydrostatic multiscale mineral dust model to reproduce the physical processes associated with the dust cycle at meteorological scales ranging from synoptic to mesoscale** (from 100 to 1 km spatial resolution) over the geographical regions of Northern Africa, the Middle East and Europe (NAMEE). Within this framework, the main tool used in this thesis is the NMMB/BSC-Dust model, the mineral dust module of the Multiscale Online Non-hydrostatic AtmospheRe CHemistry model (NMMB-MONARCHv1.0), developed at Barcelona Supercomputing Center (BSC) in collaboration with several international institutions.

Within the general objective of this thesis, three specific modeling experiments have been performed for investigating the model's ability to reproduce dust processes in a wide range of spatial scales. The first experiment aims to address the consistency of the model in resolving the dust cycle and its major involved processes, from synoptic to mesoscale (from 100 to 10 km spatial resolution), over a whole year (2011) over NAMEE. For that purpose, three model configurations are used at global and regional scales and compared to ground-based observations (surface weather sites, in-situ PM10 stations and sun-photometers) and aerosol satellite products (MISR and MODIS). The model reproduces the large-scale processes involved in the seasonality of the dust transport in comparison with satellite aerosol products, a behavior that remains consistent between the studied meteorological scales. In comparison with ground-based observations, the model shows a great ability to resolve the long-range dust transport. The model underestimates dust concentrations in the Western and Central Sahara-Sahel in summer. These underestimations are linked to a systematic wind speed underestimation, the low dust emission over Mali-Mauritania sources and omitting convective dust storms (i.e. haboobs). Otherwise, model overestimations in the Central Sahara-Sahel in spring and wintertime (from October to March) are linked to an overestimation of the Harmattan winds. In the Middle East, the model underestimates the dust concentration fields. This is partly linked to topographical features and meteorological small-scale processes that are not well resolved in the proposed configurations. A more accurate representation of the spatiotemporal variability of dust fields is found in the regional configurations. Finer scales enhance the development of the low-level jets and

the topographic effects that locally produce channeling effects (e.g. the Bodélé Depression), and also, the topographic effects reduce the emissions in coastal regions (e.g. Western Sahara and Oman) provoked by blocking large-scale sea breezes. The analysis demonstrates the model's consistency between global and regional scales.

The second experiment addresses how the model reproduces topographic effects on dust transport over complex topography. For that purpose, two regional model runs (30 and 3 km spatial resolution) covered two synoptic dust storms that occurred on 17–20 March 2012 in the Middle East. In comparison with observations from surface weather stations, sun-photometers, and satellite aerosol products (Aqua/MODIS and MSG/SEVIRI), the model successfully reproduces these two dust storms despite differences in the magnitude of the simulated dust fields. Differences between both simulations arise in Southwestern Saudi Arabia, Yemen and Oman where the topography (with peaks higher than 3000 m) alters the meteorology and the transported dust fields by channeling the dust flow through valleys or by blocking on the windward side of the mountain ranges. In this sense, the dust simulation using a higher horizontal resolution reproduced the dust transport better in the vicinity of complex terrain.

Finally, the third experiment investigates the model's ability to resolve convective dust storms with a set of five runs at different (horizontal and vertical) spatial resolutions for both parameterized and explicit convection. The analysis focuses on a convective situation on 14 July 2011 in Western Africa. Parameterized runs are limited in resolving haboobs properly because they tend to remove atmospheric instability, especially under orographic convective events. This results in an earlier and more abundant rainfall than compared to explicit runs. Haboobs and their associated processes, such as moist convection, cold pools and density currents, are well-developed in the explicit runs at 3 km, but at coarser resolutions (e.g. 10 km) those processes are less intense, and the vertical development of the haboob's front edge is poorly resolved.

Publication derived from the thesis:

- Basart, S., Vendrell, L. and Baldasano, J. M. 2016. High-resolution dust modeling over complex terrains in West Asia. Aeolian Research, 23, pp.37–50.

Other publications related to the Ph.D. thesis:

- Gkikas, A., Obiso, V., Pérez García-Pando, C., Jorba., O., Hatzianastassiou, N., Vendrell, L., Basart, S., Gassó, S. and Baldasano, J. M. 2017. Direct radiative effects of intensive Mediterranean desert dust outbreaks (In preparation).

Conference contributions:

- Vendrell, L., Basart, S., Jorba, O., and Baldasano, J. M. Does horizontal resolution produce better dust predictions? Evolution of the NMMB/BSC-Dust model for northern Africa, the Middle East, and Europe. EAC 2015, Milan (Italy), 6th – 11th September 2015.
- Gkikas, A., Obiso, V., Vendrell, L., Basart, S., Jorba, O., Pérez García-Pando, C., Hatzianastassiou, N., Gassó, S., and Baldasano, J. M. Direct radiative effects induced by intense desert dust outbreaks over the broader Mediterranean basin. EGU 2016, Vienna (Austria), 17th – 22nd April 2016.
- Vendrell, L., Basart, S., Jorba, O. and Baldasano, J. M. Study of a Sharan Haboob. 8th International Workshop on Sand/Duststorms and Associated Dustfall, Lisbon (Portugal), 1st - 4th May 2016. **This poster was awarded as the best poster presentation**.
- Gkikas, A., Obiso, V., Vendrell, L., Basart, S., Jorba, O., Pérez García-Pando, C., Hatzianastassiou, N., Gassó, S., and Baldasano, J. M. Mediterranean Desert Dust Outbreaks' Direct Radiative Effects based on Regional Model Simulations. 8th International Workshop on Sand/Duststorms and Associated Dustfall, Lisbon (Portugal), 1st – 4th May 2016.
- Vendrell, L., Basart, S., and Baldasano, J. M. Effect of Terrain Relief on Dust Transport over Complex Terrains in West Asia. 4th BSC Severo Ochoa Doctoral Symposium, Barcelona (Spain), 2nd – 4th May 2017.

Table of Contents

List of Acronyms

AAI	Absorbing Aerosol Index
AE	Ångström Exponent
AEMET	Spanish Meteorological Agency
AEROCOM	AEROsol model interCOMparison initiative
AERONET	AEROsol RObotics NETwork
AMMA	African Monsoon Multidisciplinary Analysis
AOD	Aerosol Optical Depth
BDFC	Barcelona Dust Forecast Center
BMJ	Bells-Miller-Janjic
BSC	Barcelona Supercomputing Center
CAPE	Convective Available Potential Energy
DOD	Dust Optical Depth
ECMWF	European Centre for Medium-Range Weather Forecasts
EU	European Union
EUMETSAT	European Organization for the Exploitation of Meteorological Satellites
FNL	Final Analysis
ICAP	International Cooperative for Aerosol Prediction
IPCC	Intergovernmental Panel on Climate Change
IR	Infrared
ISH	Integrated Surface Hourly
ITCZ	Inter-tropical Convergence Zone
LISS	Land Ice Sea Surface
LLJ	Low-Level Jet
MB	Mean Bias
MCS	Mesoscale Convective System
METAR	Meteorological aerodrome report
Meteosat	European Geostationary Meteorological Satellites
MISR	Multi-angle Imaging Spectro-Radiometer
MODIS	Moderate Resolution Imaging Spectro-Radiometer
MONARCH	Multiscale Online Non-hydrostatic AtmospheRe CHemistry model
MSG	Meteosat Second Generation
Mslp	Mean sea level pressure
NAMEE	Northern Africa, the Middle East, and Europe
NASA	National Aeronautics and Space Administration
NCEP	National Centers for Environmental Prediction
NDVI	Normalized Difference Vegetation Index
NLLJ	Nocturnal Low-Level Jet
NMMB	Non-hydrostatic Multiscale Model on the B-grid
NOAA	National Oceanic and Atmospheric Administration
PBL	Planetary Boundary Layer
PM	Particulate Matter
PM2.5	Particulate Matter with diameter lesser than or equal to 2.5 μm
PM10	Particulate Matter with diameter lesser than or equal to 10 μm
r	Correlation coefficient
RGB	Red Green Blue
RMSE	Root Mean Square Error
RRTM	Rapid Radiative Transfer Model
SEVIRI	Spinning Enhanced Visible and Infrared Imager
SDS	Sand and Dust Storm
SDS-WAS	Sand and Dust Storm Warning Advisory and Assessment System
SYNOP	Surface Synoptic Observations
USGS	United States Geological Survey
WHO	World Health Organization
WMO	World Meteorological Organization
WRF	Weather Research and Forecasting

Chapter 1

1 Introduction

1.1 Atmospheric aerosols

Atmospheric aerosols are liquid or solid particles that originate from both natural and anthropogenic sources. Aerosols classify as primary or secondary. Primary aerosols are directly emitted as particles into the atmosphere under mechanical processes mainly from natural sources such as sea salt from sea spray, mineral dust from dust storms, sulfate from volcanoes, and organic aerosols and black carbon from biomass burning and even from anthropogenic industrial emissions. Secondary aerosols form in the atmosphere through gas-to-particle conversion processes from precursor gases (e.g. H_2SO_4, NH_3, NO_x), which have both natural (e.g. volcano eruptions) and anthropogenic origin (e.g. from fossil fuel combustion), to particles by nucleation processes, and by condensation and coagulation processes of these particles (Seinfeld and Pandis, 2016). The most abundant secondary aerosol species are sulfate, nitrate, ammonium, and secondary organic aerosols, which have increased since the last century due to the rapid growth of population, urban areas and industrial activities. Secondary aerosols remain a low contributor to the total atmospheric aerosol mass in comparison with primary aerosols (IPCC, 2013).

Four of the most abundant aerosols to the total atmospheric aerosol mass (IPCC, 2013) such as sea salt, mineral dust, smoke (including black carbon and organic aerosols), and sulfate have different origins and propagations and are not homogeneously distributed in the world (Figure 1.1).

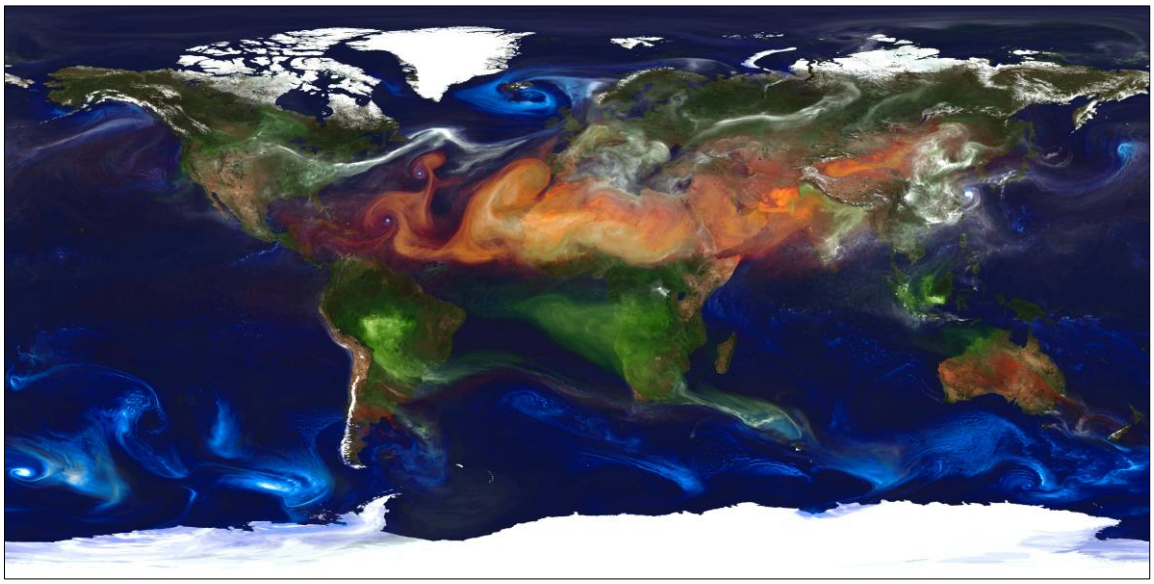

Figure 1.1: *Global NASA GEOS-5 simulation at a 10 km horizontal resolution for mineral dust (orange), sea salt (blue), smoke (green) and sulfate (white). Source: http://geos5.org*

Aerosols, depending on their diameter (D), can also be classified as fine (D < 1 μm) and coarse (D > 1 μm) particles. Primary aerosols are usually found in the coarse mode (D > 1 μm), while secondary aerosols are more predominant in the nucleation (D < 20 nm), Aitken (20 nm < D < 100 nm) and accumulation (D ~ 0.1-1 μm) modes (Seinfeld and Pandis, 2016).

In environmental sciences, aerosols are mainly measured in terms of PM10, PM2.5 and PM1 concentrations, which are defined as Particulate Matter (PM) that pass through a selective inlet for an aerodynamic diameter of 10, 2.5 and 1 μm, respectively, with 50% efficiency. Coarse particle fractions are found in the range of 2.5 to 10 μm in diameter (PM10-PM2.5), and fine particle fractions are defined as up to 2.5 μm in diameter (PM2.5). Aerosols can affect human health since their small size allows them to penetrate deep into the lungs and cause illnesses. The 2005 "WHO Air quality guidelines" (WHO, 2005) offer global guidance on thresholds and limits for key air pollutants that pose health risks to its state members. For PM, in addition to guideline values for PM10 (of 20 $\mu g/m^3$ (annual) and 50 $\mu g/m^3$ (24-h)) and for PM2.5 (of 10 $\mu g/m^3$ (annual) and 25 $\mu g/m^3$ (24-h)), the Air Quality Guidelines provide interim targets for concentrations of PM10 and PM2.5 aimed at promoting a gradual shift from high to lower concentrations. These values are guidelines that the state members transpose to their national legislation. For example, the European Commission (EC, 2008) establishes a legal limit for PM10 of 40 $\mu g/m^3$ (annual) and 50 $\mu g/m^3$ (24-h, which must not be exceeded more than 35 times per year) and for PM2.5 of 25 $\mu g/m^3$ (annual).

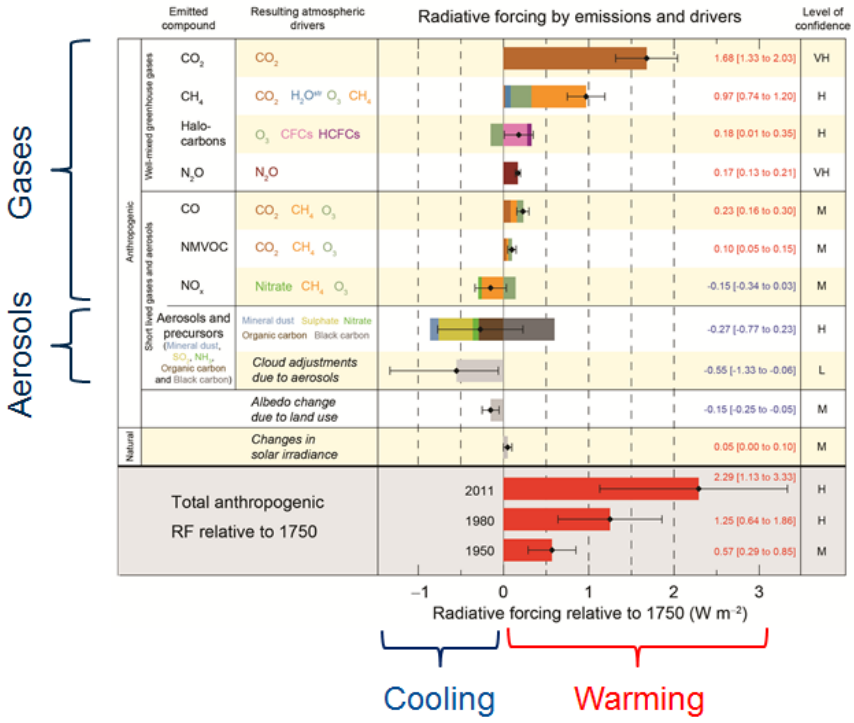

Figure 1.2: *Radiative forcing estimates in 2011 relative to 1750 and aggregated uncertainties for the main drivers of climate change (IPCC, 2013).*

Aerosol impacts also extend to atmospheric chemistry and air quality, but the radiative effects of aerosols have been identified by the Intergovernmental Panel on Climate Change (IPCC) as the largest uncertainty in radiative forcing of climate change. Aerosols alter the atmosphere's radiative balance by scattering and absorbing solar and terrestrial radiation (direct effects) and by changing cloud microphysics and precipitation processes acting as cloud condensation nuclei/ice nuclei (indirect effects). The global radiative impacts of aerosols cause a cooling effect, estimated as a net Radiative Forcing (RF) of -0.9 (-1.9 to -0.1) Wm^{-2} (IPCC 2013; see Figure 1.2).

In recent years, the mineral dust has emerged as one of the most studied aerosol species in the research field of Earth sciences due to its several specific and significant impacts on weather, climate, air quality, human health, ecosystems and socio-economic activities (Knippertz and Stuut, 2014).

1.2 Desert dust in the Earth system

1.2.1 Overview of worldwide desert dust sources: location and variability

The world's major dust sources are located in the Northern Hemisphere in an area called the "dust belt" (i.e. Northern Africa, the Middle East, East Asia and North America), while in the Southern Hemisphere (with less land mass than the Northern Hemisphere), dust sources are of smaller spatial extension and are located in Australia, South America, and South Africa (Figure 1.3).

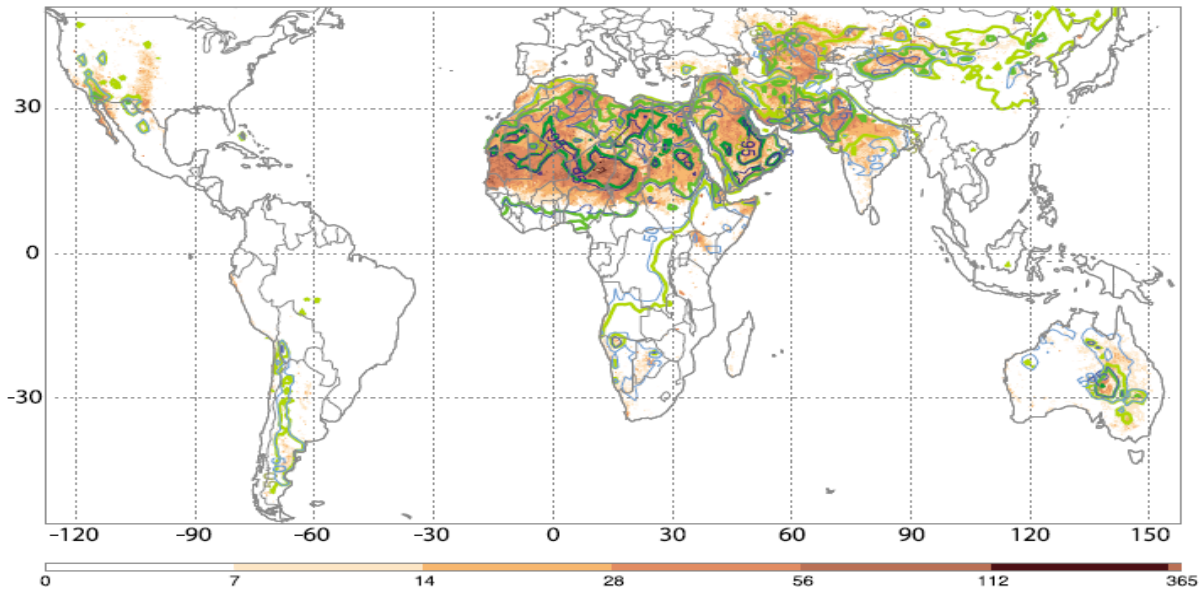

Figure 1.3: *Annual mean frequency distribution of MODIS Deep Blue (2003–2009) Dust Optical Depth (DOD) > 0.2 (brown color scale), TOMS (1980–1991) Aerosol Index (AI) > 0.5 (blue contour lines), and OMI (2004–2006) AI > 0.5 (green contour lines). Extracted from Ginoux et al. (2012).*

Mineral dust is usually considered as natural when wind processes generate it over arid or semi-arid regions characterized by sparse vegetation, and the main large dust source regions correspond with mostly topographically low and natural dried paleolakes (Ginoux et al., 2001, 2012; Prospero, 2002). On the other hand, mineral dust is considered anthropogenic when human activities affect dust emission directly by altering land properties and uses such as road dust, increase in agricultural surfaces or grazing practices, or indirectly with climate change such as changes in wind and precipitation patterns. The total global dust emissions are 75% from natural origins and 25% from anthropogenic origins, principally from agriculture (Ginoux et al., 2012). In that total global dust emission budget, hydrologic dust sources (e.g. ephemeral water bodies) make a significant contribution and account for 31%, which is also divided into dust sources from natural and anthropogenic origins (15% and 85%, respectively) (Ginoux et al. 2012).

Global annual dust emissions from natural and anthropogenic origins are still uncertain. Based on the global models participating in the AEROsol model interCOMparison (AEROCOM) initiative, emission estimates quantified natural dust emissions as varying between 1000 and 4000 Tg (IPCC, 2013), whereas a climate-aerosol model (ECHAM6-HAM2) estimates anthropogenic sources' contribute at between 729 and 912 Tg globally (Stanelle et al., 2014). Moreover, according to Stanelle et al. (2014), global annual dust emissions have increased by 25% between the late nineteenth century and today. About 56% of this change is attributed to climate change and 40% to anthropogenic land cover changes (e.g. agricultural expansion). However, regional patterns may differ significantly from global estimates.

Dust emissions from their worldwide sources and their atmospheric dust transport reveal seasonal and spatial variability (Tegen et al. 2002; see Figure 1.4), which are mainly characterized by variations in meteorological conditions in the low troposphere and by global circulation patterns, such as the seasonal displacement of the Inter-tropical Convergence Zone (ITCZ) (Schepanski et al. 2009) and monsoons (Bou Karam et al., 2008; Cuesta et al., 2010; Vinoj et al., 2014). Also, interannual variation in dust patterns are presented, such as in the Northern African dust transport which has been linked to drought conditions in the Sahel and the North Atlantic Oscillation (NAO) (Prospero & Lamb 2003; Chiapello et al. 2005), the El Niño/Southern Oscillation (ENSO) in summer (DeFlorio et al. 2016), and surface temperatures over the Sahara (Wang et al. 2015). Although these interannual variabilities and relationships are not yet fully understood, all of them reveal the connection between dust and climate.

Among all global dust sources, Northern Africa is the world's largest dust source (Figure 1.3), composed of the Sahara Desert in the north and center and the semi-arid Sahel in the south. Northern Africa contributes to more than half of global dust emissions (e.g. Prospero et al. 2002; Huneeus et al. 2011; Ginoux et al. 2012). Based on MODIS Deep Blue satellite observations (Ginoux et al., 2012), Northern Africa accounts for 55% of global dust emissions, with only 8% being anthropogenic,

although it contributes to 20% of global anthropogenic emissions, mostly from the semi-arid Sahel (Ginoux et al., 2012). Despite the increase in anthropogenic dust sources, most of the Northern African dust activity over the past decades (up to 16%) seems to be dominated by climate change (Stanelle et al., 2014).

In Northern Africa, emission estimates based on global models (AEROCOM) widely range from 400 to 2200 Tg/yr (Huneeus et al., 2011). The large uncertainty in dust emission estimates is partly linked to the lack of detailed information on dust sources and not accounting for small-scale features that could potentially be responsible for a large fraction of the global dust emissions (Ginoux et al., 2012; Knippertz and Todd, 2012). The largest single dust source in Northern Africa (and in the world) is the Bodélé Depression located to the north of Lake Chad (Ginoux et al., 2001, 2012; Prospero, 2002). With the other depressions and the gaps on the downwind side of the Saharan mountains (mainly between 15ºN and 20ºN in latitude), these sources combined can contribute about 85% of all Northern African dust emissions (Evan et al., 2015).

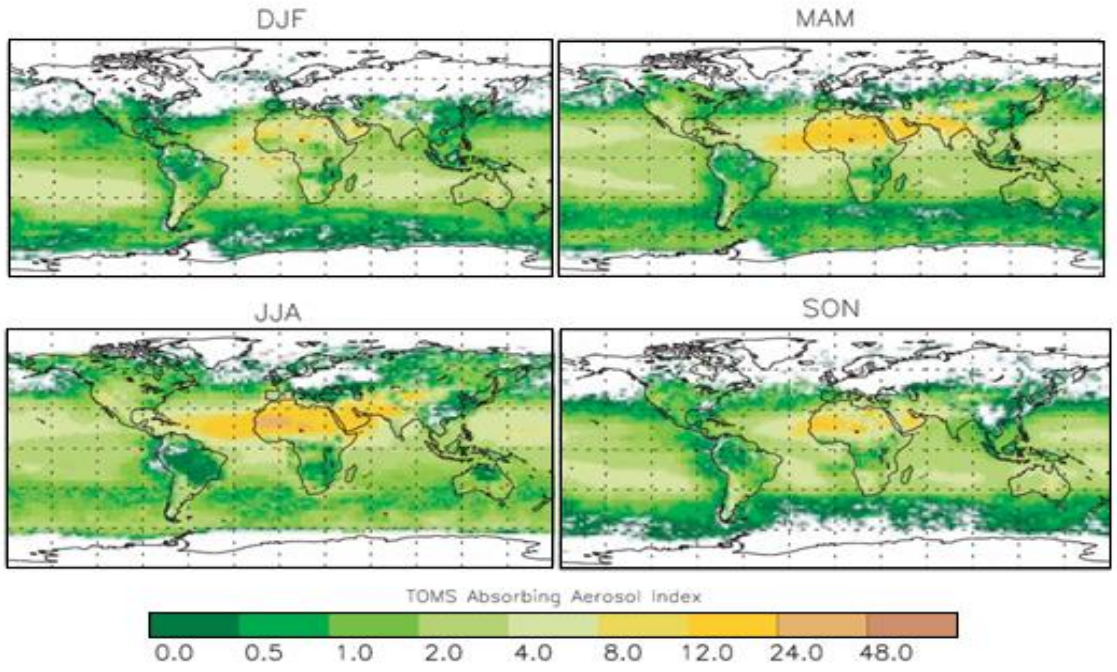

Figure 1.4: *Global seasonal Absorbing Aerosol Index (AAI) based on TOMS satellite, averaged for 5 years (1986-1990). High AAI shows the presence of dust particles. Extracted from Tegen et al. (2002).*

As shown in Figure 1.4, dust activity is associated with a marked seasonality and shifts throughout the year from winter, when it is more pronounced in low latitudes, to summer, when it is observed at higher latitudes (Tegen et al., 2002, 2013; Schepanski et al., 2007). Northern African dust is mainly transported along three main pathways: (1) westwards over the North Atlantic Ocean to the Americas (Prospero, 2002; Marticorena et al., 2010; Gama et al., 2015), revealing its maximum occurrence

between June and July and the minimum from December to February (Prospero, 1996; Basart et al., 2009; Tsamalis et al., 2013); (2) northwards towards the Mediterranean and Southern Europe and, on exceptional outbreaks, dust particles can be transported to Scandinavia and the Baltics (Barkan et al., 2004; Papayannis et al., 2005; Basart et al., 2009; Pey et al., 2013; Gkikas et al., 2016), which has a higher occurrence during spring and summer and lower in winter (Basart et al. 2009; Pey et al. 2013; Gkikas et al. 2016); and (3) eastwards (from East Africa), which is more frequent in spring and summer towards the Middle East (Goudie and Middleton, 2006; Kalenderski and Stenchikov, 2016) but also possibly as far as the Himalayas (Carrico et al., 2003).

In the Middle East, the main dust sources are located in the Arabian Peninsula, such as the Rub' Al Khali desert, which is one of the largest sand deserts in the world (Ginoux et al., 2012). Other important dust sources are located in Iraq, Pakistan, and parts of Iran and Afghanistan (Goudie and Middleton, 2006; Ginoux et al., 2012; Rezazadeh et al., 2013). Emission estimates for the Middle East vary from 26 to 526 Tg/yr (Huneeus et al., 2011). The seasonal dust activity varies depending on the region. Dust activity is at a maximum in the west of the region during the winter months and shifts to the east from spring to summer when the southwest monsoon is well developed (Prospero, 2002). The severest dust storms are associated with the summer Shamal (northwest winds), which can lift large amounts of dust from their sources and transport them over large distances towards the Indian Ocean (Li and Ramanathan, 2002). In winter, dust storms are mainly caused by the coupling of mid-latitude cold front systems (with winds from the north) and the extent of the southern wind from the Red Sea uplifting dust from many sources at once (Jiang et al., 2009; Kalenderski et al., 2013; Jish Prakash et al., 2015). The maximum number of dust events are observed over the Sistan Basin, in Eastern Iran and Western Afghanistan, as a result of strong north winds, commonly known as the "wind of 120 days" (Alizadeh-Choobari et al., 2014). Based on visibility measurements, Pakistan is considered as one of the places with a higher mean dust concentration (Rezazadeh et al., 2013). Sea breezes across the coastal areas (e.g. the Persian Gulf) and thunderstorms, make an important contribution to the dust emissions in the Middle East (Miller et al., 2008). Moreover, in recent years the frequency of dust storms over the region has been increasing by about 9% (Stanelle et al., 2014), mainly caused by changes in land cover, with an anthropogenic contribution of about 30% of the total dust sources (Ginoux et al., 2012). Additional factors in this anthropogenic contribution include the ongoing conflict in the region (Gleick, 2014) and climate change in recent years (Stanelle et al. 2014; Parolari et al. 2016), which is mainly identified by several drought periods (Kelley et al., 2015; Notaro et al., 2015; Klingmüller et al., 2016) and is even leading to more severe dust storms (Solomos et al. 2017).

In East Asia, the largest natural sources are located in Northern China (i.e. Taklamakan, Badain Jaran, Tengger, and Ulan Buh Deserts) and Mongolia (i.e. Gobi Desert). Dust storms are more frequent and severe in spring (Ginoux et al., 2012), and dust particles are mainly carried eastwards from China and Mongolia to East Asia, Japan, Korea (Hong et al., 2010), across the North Pacific Ocean to the western

part of North America (Fairlie et al., 2007), and even to the Arctic (Fan, 2013). East Asia also presents large anthropogenic dust sources (25% of the total; Ginoux et al. 2012), which are mostly identified in India and some regions of China such as the North China Plains (Ginoux et al., 2012; Stanelle et al., 2014), which contribute to a regional increase of dust activity of about 17% over the last decades (Stanelle et al., 2014).

North American dust activity is focused in the Southwestern United States (Arizona and California) and in Northwestern Mexico, where the hottest desert in North America, the Sonoran Desert, is located. The dust events over this desert area occur most frequently in spring and barely during the rest of the year with the minimum dust activity in winter (Ginoux et al., 2012). North America has also been increasing its dust activity during recent decades by up to 41% (Stanelle et al., 2014), mainly caused by its agricultural activities, with a large contribution of the High Plains (Ginoux et al., 2012).

Outside the "dust belt", Australia is the largest dust source in the Southern Hemisphere (Ginoux et al., 2012). McTainsh & Pitblado (1987) identified the five main regions characterized by high frequency of dust storms: (1) Lake Eyre basin, (2) Central Queensland, (3) the Mallee region, (4) the Nullarbor Plain, and (5) the Central Western Australian coast. Australian dust is transported across the continent along two major routes: over the Southern Pacific Ocean and the Indian Ocean (McTainsh, 1989). Ginoux et al. (2012) identified that dust storms mainly occur between September and February in most of the Australian sources. Over the last decades, Australia has been increasing its dust activity (by up to 71%) due to significant changes in its land cover (Stanelle et al., 2014). Based on some studies (Ginoux et al., 2012), Australia accounts for around 75% of dust emissions of anthropogenic origin (13% at a global scale).

South American dust sources are located in: (1) the Atacama Desert (Chile), which is known as the world's driest region, (2) Patagonia (Argentina) and (3) the Bolivian Altiplano (Bolivia), which contains the world's largest salt flat (Salar de Uyuni). The maximum occurrence of dust storms in these regions is monitored between December and February (Ginoux et al., 2012). Large anthropogenic dust sources over the region are largely found in Patagonia, which is associated with livestock grazing (Ginoux et al., 2012).

South African dust sources are identified as ephemeral inland lakes, coastal pans, and dry river valleys. Southern African dust source locations are mainly found in the following regions: (1) Etosha Basin (Namibia), (2) Makgadikgadi Basin (Botswana), (3) Namib Coastal Sources (Namibia), (4) South Western Kalahari Sources (mainly South Africa) and (5) Free State Sources (South Africa). Dust activity in the region is dominated by the Makgadikgadi and Etosha pans with weak activity detected throughout the year and an increase from summer to autumn (Ginoux et al., 2012; Vickery et al., 2013). Major anthropogenic sources are found in the north of Cape Town and Bloemhof reservoir by agriculture activities and in Southern Madagascar due to intense deforestation (Ginoux et al., 2012).

1.2.2 Dust impacts

1.2.2.1 Direct and indirect effects of dust in weather and climate

Mineral dust alters the energy balance of the Earth-Atmosphere system by absorbing, scattering and emitting shortwave (SW) and longwave (LW) radiation and by affecting many atmospheric processes (IPCC, 2013). On average, the LW effect of dust is warming at the surface, cooling of the atmospheric column, and warming at the top of the atmosphere (TOA). The SW radiative effect of dust at the TOA is generally negative, globally estimated at -0.1 (-0.3 to +0.1) $W \cdot m^{-2}$ (IPCC, 2013). The direct dust-radiation interactions impact atmospheric dynamics by affecting the temperature profiles (Pérez et al., 2006), which can also lead to reducing the planetary boundary layer (PBL) height (Pandolfi et al., 2013; Kumar et al., 2014; Marcella and Eltahir, 2014), sea surface temperature (Foltz & McPhaden 2008) and hurricane activity (Dunion and Velden, 2004; Evan et al., 2006, 2011; Bretl et al., 2015). The indirect dust-radiation impacts rely on the modification of clouds and precipitation processes (Creamean et al., 2013) acting as cloud condensation nuclei/ice nuclei (Klein et al., 2010; Nickovic et al., 2016), which reduce the number of cloud droplets and increase cloud reflectivity (Su et al., 2008), the lifetime of the clouds (Heymsfield et al., 2009; Cziczo et al., 2013), and the precipitation (Teller and Levin, 2005). The dust-radiative interactions are sensitive to several features of dust particles, such as particle size distribution, chemical composition (mixing with other aerosols and mineralogy), shape, the altitude of the dust layer, and underlying surface properties (Otto et al., 2007), which determine the dust optical properties (e.g. extinction coefficients, dust optical depth and Ångström Exponent).

1.2.2.2 Impact of dust on ecosystems

Mineral dust has both positive and negative global impacts on ecosystems by its deposition on land, which accounts for 75% of the total depositions, and the ocean, which accounts for 25% of the total depositions (Shao et al. 2011). Dust alters the biochemical cycles both of marine and terrestrial ecosystems, highlighting its important role in the Earth-Atmosphere system (Jickells et al. 2005; Figure 1.5), although these connections are complex and not yet fully understood (Knippertz and Stuut, 2014).

Dust impacts are recorded in many physiological processes of plants, including photosynthesis (Wijayratne et al., 2009; Ibrahim and El-gaely, 2012). Mineral dust is a source of nutrients such as iron and phosphorus, playing an important role in fertilization of land in such places as the Amazon rainforest (Bristow et al., 2010; Yu et al., 2015). The deposition of dust on some continental ecosystems not only impacts the vegetation but also the global carbon cycle. Deposition in the oceans can also fertilize algae or the phytoplankton (Jickells et al., 2005), which impacts marine

biogeochemical cycles (Wang et al. 2015). Dust air masses transported from Asia and Africa may negatively affect coral reefs and other downwind ecosystems in the Americas by carrying on contaminants, pesticides or trace metals that were deposited on land and in the oceans (Garrison et al., 2003).

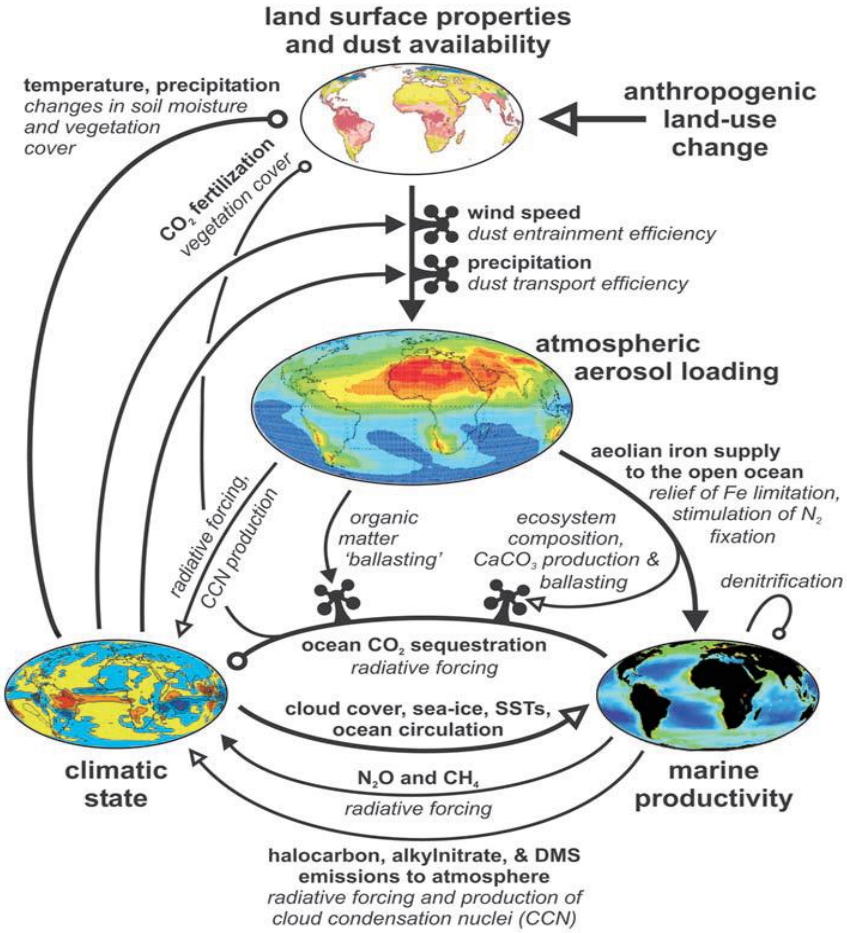

Figure 1.5*: Schematic view of global iron and dust connections. Highlighted are the four critical components (clockwise from top): the state of the land surface and dust availability, atmospheric aerosol loading, marine productivity, and some measure of climatic state (such as mean global surface temperature). The sign of the connections linking these varies: where the correlation is positive, the line terminates with a solid arrowhead. Where the correlation is negative the termination is an open circle. Connections with an uncertain sign terminate with an open arrowhead. Extracted from Jickells et al. (2005).*

1.2.2.3 Dust impact on human health and socio-economic activities

Since a substantial amount of airborne dust particles are in the respirable size range, they can penetrate into the body by inhalation and produce a wide range of human health hazards (Morman and Plumlee, 2013; Goudie, 2014; Zhang et al., 2016) that are still not completely understood (WHO, 2005). Mineral dust particles substantially contribute to PM10 and PM2.5 concentrations over many regions.

Particularly in Europe, African dust outbreaks cause the exceedance of the EU air quality thresholds for PM10 and PM2.5 (Rodríguez et al. 2001; Basart et al. 2012; Pey et al. 2013; Barnaba et al. 2017).

Otherwise, some studies have suggested that during dust episodes, mineral dust particles can transport bacteria, fungi or spores (Kellogg et al., 2004; Smith et al., 2011, 2013), biological endotoxins (Ortiz-Martínez et al., 2015), anthropogenic atmospheric pollutants and heavy metal compounds (e.g. Ni, Al and Fe) (Otani et al. 2012), and radiative material (Akata et al., 2007; Yamauchi, 2012). Various negative impacts on human health have been documented during dust episodes such as lethal meningitis (Thomson et al., 2006; Pérez García-Pando et al., 2014), eye infections (Chien et al., 2014), valley fever (Sprigg et al., 2014; Litvintseva et al., 2015), skin irritations (Otani et al., 2012), respiratory disorders (Thalib and Al-Taiar, 2012), and cardiovascular diseases (Meng and Lu, 2007; Goudie, 2014).

Atmospheric dust also has significant impacts on various social and economic activities. Dust storms can reduce visibility down to a few hundred meters, thus affecting road and air transport (Shirkhani-Ardehjani, 2012). Solar plant production can be decreased due to the extinction of solar radiation by dust aerosols (Schroedter-Homscheidt et al., 2013) as well as by the effects of dust accumulation on the solar panels (Nadh et al., 2014). Stefanski & Sivakumar (2009) reported that dust storms have many negative impacts on the agricultural sector, including reducing crop yields, the loss of plant tissue and reduced photosynthetic activity, delaying plant development, increasing end-of-season drought risk, increasing soil erosion and accelerating the process of land degradation and desertification. Nevertheless, one positive impact is the fertilization of soil minerals to terrestrial ecosystems.

1.2.2.4 International initiatives for the monitoring and forecasting of sand and dust storms

Over the past decade, there has been a growing recognition of the crucial role of sand and dust storms (SDS) on weather, climate, and ecosystems, along with their substantial adverse impacts on life, health, property, economy and other strategic sectors. Different collaborative European and international initiatives and projects have been set to better monitor and predict the dust (and aerosol in general) cycle (ICAP, AEROCOM, Aerosol-CCI or ACTRIS) and its impact on air quality (EU Life+ Diapason), health (EU Life+ MED-PARTICLES), energy (DNICast, WASCOP) and transport (Daedalus) as well as to provide products to end-users (e.g. Copernicus). Reacting to the concerns about SDS by its most affected member states, in 2007, the World Meteorological Organization (WMO) endorsed the launch of the SDS Warning Advisory and Assessment System (SDS-WAS; http://www.wmo.int/pages/prog/arep/wwrp/new/Sand_and_Dust_Storm.html). The SDS-WAS mission is to enhance the delivery of timely and quality SDS forecasts, observations, information and knowledge to users through an international partnership of research and operational communities. The

SDS-WAS is established as a federation of partners organized around regional nodes. The SDS-WAS regional centers support a node, which consists of a network of research and operational partners implementing SDS-WAS objectives in a region. At the moment three nodes are established: the Northern Africa-Middle East-Europe (NAMEE) node (hosted by Spain, http://sds-was.aemet.es), the East Asian node (hosted by China, http://sds.cma.gov.cn) and the Pan-American node (hosted by Barbados, http://sds-was.cimh.edu.bb/). In view of the demand of many national meteorological services and the achievements of the SDS-WAS regional centers, the 65th session of the WMO executive council designated Spain to create in Barcelona the first regional specialized meteorological center with activity specialization on atmospheric sand and dust forecast for NAMEE, known as the Barcelona Dust Forecast Center (BDFC; http://dust.aemet.es). The Center was created in February 2014 and its mandate is to generate and distribute operational dust forecasts. Recently, a second specialized center on atmospheric sand and dust forecasts has been approved in Beijing (China) and will soon be operative.

1.2.3 Dust cycle and associated processes

The dust cycle involves several processes such as dust emission, transport, and deposition (Figure 1.6), which occur at a wide range of spatial and temporal scales. Based on wind-tunnel experiments (Bagnold, 1941), dust particles, depending on their sizes, are released into the atmosphere through three mechanisms: (1) aggregate disintegration for rolling (or creeping) particles larger than 2 mm, (2) saltation bombardment for particles between 60 μm and 2 mm, (3) aerodynamic entrainment or suspension of particles finer than 60 μm. Despite this, emission processes are affected by several soil features such as soil moisture, soil texture, surface crust, roughness elements and vegetation (Figure 1.6).

Once strong winds emit dust particles, fine dust particles are carried by turbulent diffusion and convection to higher tropospheric levels (up to a few kilometers in height) and then large-scale winds can transport them over long distances (i.e. Prospero 1996; Goudie & Middleton 2006). Dust particles into the atmosphere scatter and absorb solar radiation and, acting as cloud condensation nuclei/ice nuclei, modify clouds and their radiative and precipitation processes (Figure 1.6). The lifetime of dust particles in the troposphere is dependent on the particle size because it takes much longer for smaller particles to deposit back on the surface than larger particles. For example, based on observations, the lifetime of dust particles with a diameter larger than 20 μm is on the order of 12 h (Ryder et al., 2013); meanwhile, finer particles can have lifetimes of up to 10-15 days, indicating a longer distance of transportation (Ginoux et al., 2001). These particles are removed from the atmosphere through dry deposition processes, including gravitational settling and turbulent transfer, and wet deposition processes including in- and below-cloud scavenging.

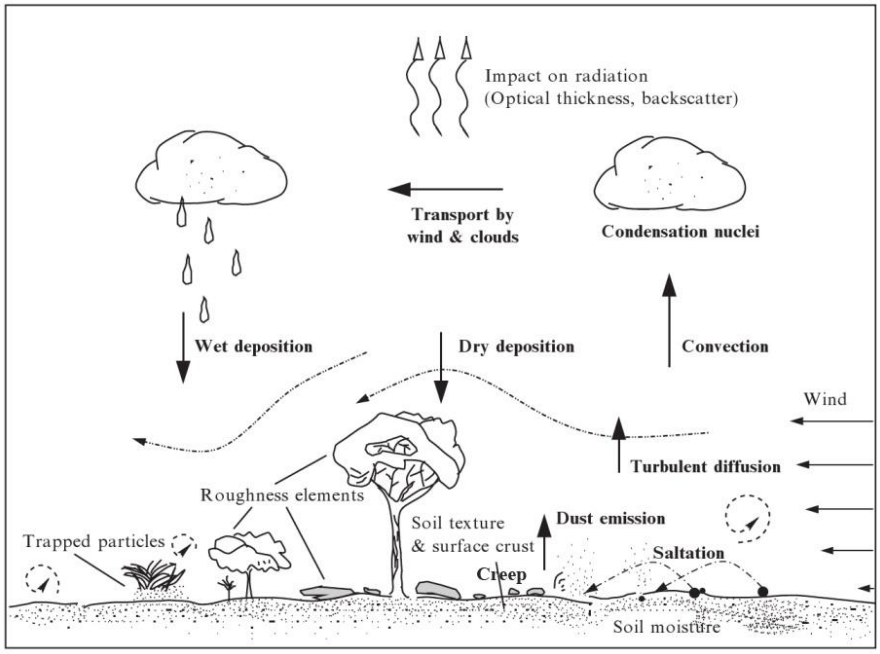

Figure 1.6: *Depiction of the dust cycle processes, their components, controlling factors and impacts on radiation and clouds. Extracted from Shao (2008).*

1.2.3.1 Meteorological mechanisms involved in dust storms

According to WMO, dust storms are generated by strong surface winds that raise a large number of dust particles into the air and reduce visibility to less than 1000 m (McTainsh and Pitblado, 1987). There are several meteorological mechanisms, each with its own diurnal and seasonal features, occurring at a wide range of spatiotemporal scales (i.e. synoptic, mesoscale and microscale) that potentially control strong winds and cause dust storms: (1) large-scale flows mainly associated with monsoon winds and frontal passages; (2) the breakdown of the nocturnal low-level jet (NLLJ) and cold pool outflows from moist convective storms associated with the haboob's formation; (3) microscale dry convection linked to the generation of dust devils and dust plumes. These processes can locally be modified by topographic effects such as blocking, channeling and forced convection. Next, a brief description of each meteorological mechanism is presented.

Large-scale flows mainly associated with monsoon circulations (Indian and West Africa), shear-lines (observed both near the ground and in jet streams), synoptic-scale systems (cyclones, anticyclones and their cold frontal passage), and thermal lows over continents (as the Saharan Heat Low, SHL, see L in Figure 1.7) affect the emission and transport of dust by strong large-scale winds over long distances (Knippertz and Todd, 2012).

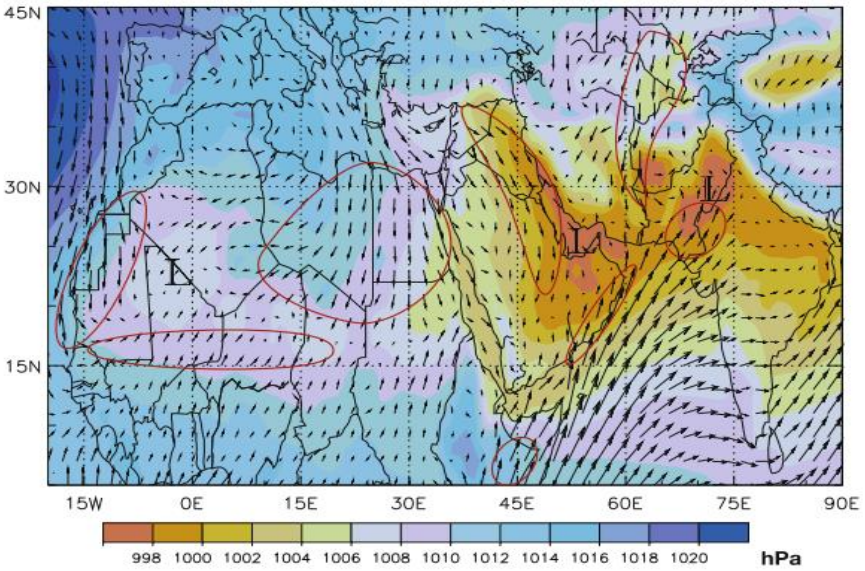

Figure 1.7: *Summer (June–August) mean sea-level pressure (shaded) and winds at 10 m (arrows). The three main continental heat lows ('L') are shown over Western Africa, the Arabian Peninsula and the Pakistan-Indian border with a strong inflow into these heat lows prone to dust generation and marked in red. This data is based on ERA-Interim reanalysis (1979–2012) from the ECMWF. Figure extracted from Knippertz & Stuut (2014).*

The breakdown of the nocturnal low-level jet (NLLJ; see Figure 1.8) is a meteorological mechanism that produces strong winds near the top of the nocturnal boundary layer and can generate near-surface peak winds due to shear-driven turbulence in the course of the night. Then, the downward mixing of momentum in the PBL can produce dust emission. The breakdown of the NLLJ tends to occur around midday (e.g. Parker et al. 2005; Fiedler et al. 2013).

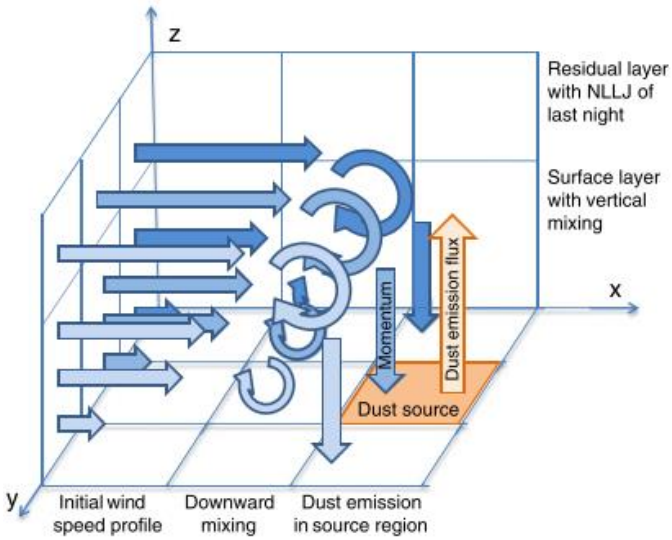

Figure 1.8: *Schematic diagram showing the morning breakdown (downward mixing) of the nocturnal low-level jet (NLLJ) momentum. Turbulent mixing transports momentum toward the surface, which leads to dust emissions (if the given threshold velocity is overcome). Figure extracted from Fiedler et al. (2013).*

Cold pool outflows from moist convection are the main drivers of convective dust storms, called haboobs (from the Arab word for wind). Cold pool outflows are downdrafts caused by the evaporation and cooling of rain from thunderstorms which, near-surface, cause gravity currents where strong winds can uplift dust. Strong winds (head) uplift a large amount of dust and generate a "wall of blowing dust" on the leading edge of the haboob (nose) where warm air is forced upward by the cold air (Figure 1.9). Haboobs may reach 1.5-4 km in height and span hundreds of kilometers over desert areas and, because of the diurnal cycle of deep moist convection, they occur from late afternoon to night, with a typical lifetime of a few hours (Knippertz and Todd, 2012; Marsham et al., 2013).

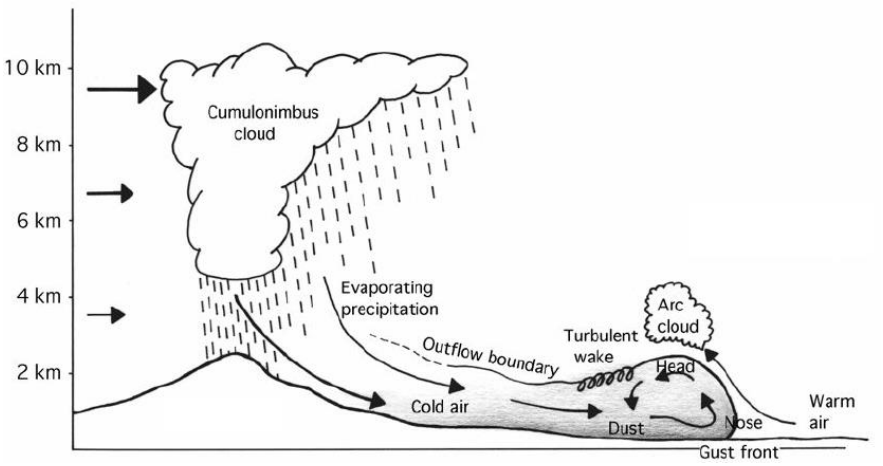

Figure 1.9: *Cross section schematic of a haboob. Extracted from Knippertz et al. (2007)*

Microscale dry convection in the daytime PBL over deserts can cause dust devils and dust plumes by turbulent circulation. The most favorable conditions for their formation are under clear skies, strong surface heating, and weak background winds. Dust devils have a lifetime from a few minutes to less than an hour and occur at spatial scales from a few to several hundred meters (Knippertz and Todd, 2012). Figure 1.10 shows a typical sequence of the dust devil's formation caused by intense surface heating, turbulent winds and microscale dry convection.

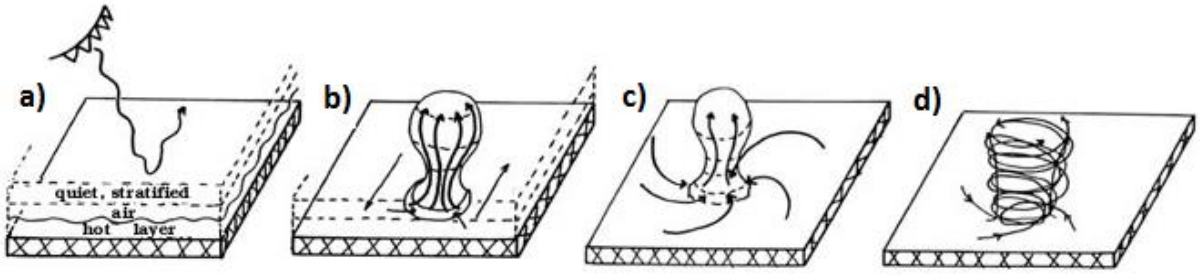

Figure 1.10: *Scheme of dust devil formation. (a) Sun heats air nearest ground, (b) wind causes hot air bubble to break through to stratified layer, (c) near surface cyclonic circulation around low-pressure zone below the newly formed air bubble, and then (d) like a tetherball, the air moves faster as it approaches the center, then spirals rapidly upward to maintain the dust devil.*

1.3 Numerical dust models

Dust impacts on the Earth's radiation balance, atmospheric dynamics, biogeochemical processes and atmospheric chemistry are only partly understood and remain largely unquantified. An assessment of the various effects and interactions of dust and climate requires a quantification of global atmospheric dust loads and their optical and microphysical properties. Dust distributions used in the assessments of dust effects on climate usually rely on results of large-scale numerical models that include dust as a tracer. Otherwise, over the last few years, numerical prediction of dust concentration has become prominent in various research and operational weather centers due to growing interest from diverse stakeholders, such as solar energy plant managers, health professionals, aviation and military authorities, and policymakers. Including dust transport interaction with the atmosphere in numerical models can improve the accuracy of weather forecasts and climate simulations and contribute to a better understanding of the environmental processes caused by mineral dust.

For estimating the impact of dust on the Earth System, knowledge of the atmospheric dust's life cycle, including dust source activation and subsequent dust emission, dust transport routes, and dust deposition, is crucial. To correctly describe and quantify the dust cycle, one needs to understand equally well local-scale processes such as saltation and entrainment of individual dust particles as well as large-scale phenomena such as mid- and long-range transport (see Figure 1.11). Dust models face some challenges owing to the complexity of the system. At the center of the problem is the vast range of scales required to fully account for all of the physical processes related to dust emission, transport and deposition (i.e. time scales ranging from seconds to weeks). Another limiting factor is the paucity of suitable dust observations available for model development, evaluation and assimilation, particularly over desert dust sources.

While global models of dust cycle are used to investigate dust at large scale and long-term changes (e.g. desertification), regional models are ideal for studying processes that influence dust distribution (e.g. haboobs). Recent years have seen a considerable increase in the number and complexity of dust models used both for research and for operational purposes. Due to the increase of computer power, these models can be run at higher spatial resolutions to allow for investigations of smaller-scale meteorological processes such as the effects of cold outflows from thunderstorms on dust emission (Heinold et al., 2013; Solomos et al., 2017). At the same time, there have been some new approaches to treating emission processes in the models at high resolution (Kok, 2011; Klose and Shao, 2016). An important new development from an operational point-of-view is the introduction of dust prediction models (global and regional) at several modeling centers around the world (as NCEP, NASA, ECWMF or BSC), which produce daily dust forecasts for air-quality and weather warning purposes.

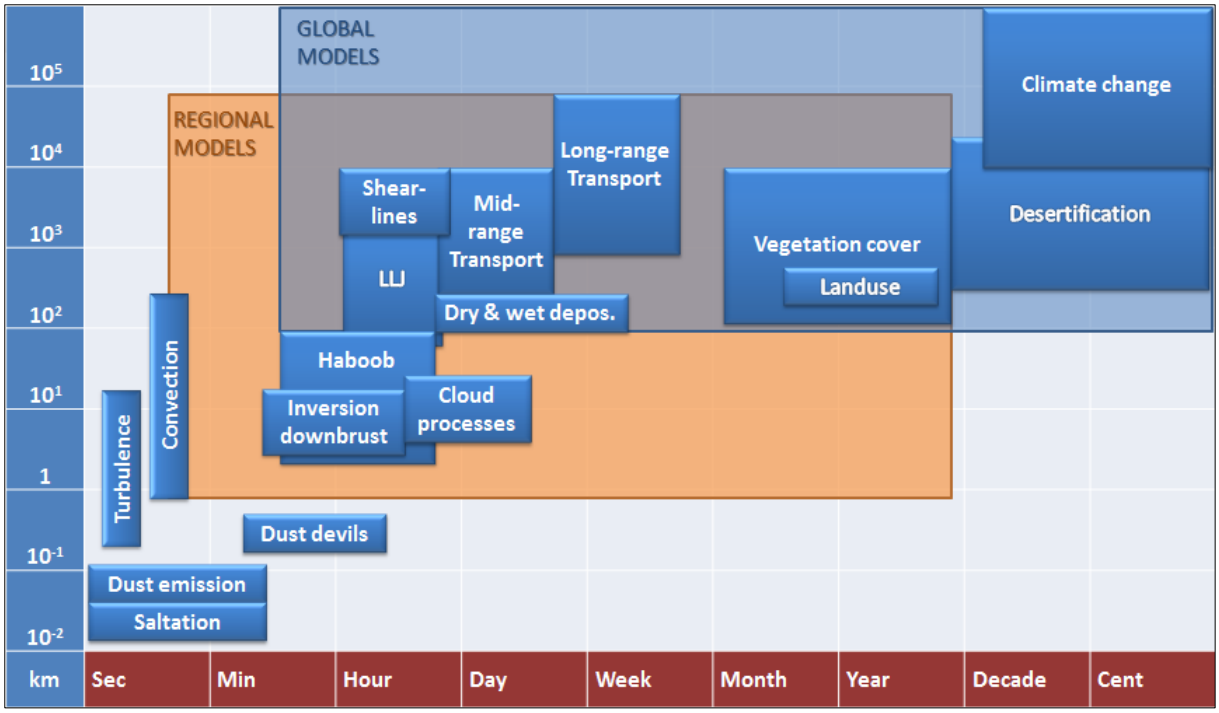

Figure 1.11: *Approximate spatial and temporal scales of the processes involved in the dust cycle. Blue and orange squares represent, respectively, the ability of the global and regional models to simulate these processes. Adapted from Shao et al. (2011). *LLJ (low-level Jet). Based on their spatial scale, they classify into synoptic-scale (~100 km), mesoscale (~1 to a few hundred km), and microscale (< 1 km).*

Modeling studies search to assess the dust global budget including the contribution of the different dust storm types. At global scales, models can reproduce the main dust transport pathways (Cakmur et al., 2006; Huneeus et al., 2011) driven by large-scale flows (mainly associated with monsoon winds and frontal passages) showing that these storms are the main contributor to the dust global budget. Otherwise, the contribution of smaller scale dust storms (associated with convection) is still uncertain (Knippertz and Todd, 2012). Fiedler et al. (2013) suggest that the breakdown of the NLLJ annually can cause 15% of the dust emission in Northern Africa (up to 60% in the Bodélé Depression). Miller et al. (2008) estimated that the haboob activity in the Middle East in summertime could be responsible for 30% of its dust emissions. A recent study from Pope et al. (2016) suggests that haboobs may be responsible for up to 30% of dust emissions in Northern Africa in summer. Redl et al. (2015) quantify the frequent occurrence of haboobs in Western Africa, from south of the Atlas Mountains in Morocco to Algeria, on the order of six per month from May to September. In Western Africa, both haboobs and the breakdown of the NLLJs appear to account for 40 to 50% of the dust emissions in summer (Allen et al., 2013; Fiedler et al., 2013; Heinold et al., 2013; Marsham et al., 2013). Microscale dust devils are not resolved in operational dust models and are still linked to a large uncertainty (Knippertz and Todd, 2012; Jemmett-Smith et al., 2015; Klose and Shao, 2016). Their global estimates could contribute by ~26% ± 18% to the total dust emissions (Koch & Renno 2005). Recent studies (i.e. Jemmett-Smith et al. 2015) estimates their global contribution to ~3.4% (uncertainty range 0.9–31%).

1.4 Dust modeling and forecasting at the Barcelona Supercomputing Center

The Earth Sciences Department at BSC (ES-BSC) has become a reference institution in Europe in the field of climate prediction, air quality, and atmospheric composition modeling. The Atmospheric Composition group at ES-BSC aims at better understanding and predicting the spatiotemporal variations of atmospheric pollutants along with their effects on air quality, weather and climate and contributes to a variety of forecasting activities. A core activity of the group is the SDS modeling and forecasting from regional to global scales.

Atmospheric modeling activities at ES-BSC include the development of the state-of-the-art Multiscale Online Non-hydrostatic AtmospheRe CHemistry model (NMMB-MONARCHv1.0) in collaboration with the National Centers for Environmental Prediction (NCEP) and the NASA Goddard Institute for Space Studies. At present, NMMB-MONARCHv1.0 includes eight aerosol types (i.e. dust, sea salt, black carbon, organic matter, sulfate, nitrate, ammonium and volcanic ash), a detailed gas-phase chemistry mechanism, and allows radiative feedbacks between aerosols and the atmosphere (Pérez et al. 2011; Haustein et al. 2012; Jorba et al. 2012; Spada et al. 2013; Spada et al. 2015; Badia et al. 2017) as well as an assimilation scheme based on the local ensemble-based transform Kalman filter (Di Tomaso et al. 2017).

The department also maintains daily operational dust forecasts up to 72 h for regional domains and up to 120 h for global domains (http://www.bsc.es/ESS/bsc-dust-daily-forecast), which are used as the reference forecast in the Barcelona Dust Forecast Center (BDFC, https://dust.aemet.es/; see Section 1.2.2.4) and contribute to the multi-model ensemble forecasts, both at the WMO SDS-WAS Regional Center (https://sds-was.aemet.es/, see Section. 1.2.2.4) for Northern Africa, the Middle East, and Europe (NAMEE), and the International Cooperative for Aerosol Prediction (ICAP). Furthermore, BSC is managing (jointly to the Spanish Meteorological Agency, AEMET) the WMO SDS-WAS Regional Center for NAMEE and the operational BDFC (see Section 1.2.2.4). Apart from that, the department is hosting the AXA Chair on Sand and Dust Storms (SDS), which is a long-term research program that aims to integrate fundamental SDS research (supporting the current activities at ES-BSC) with assessment and the implementation of SDS risk assessment and mitigation strategies.

1.5 Aim of the Ph.D. thesis

As introduced in previous sections, dust models face a wide number of challenges owing to the complexity of the Earth system. At the center of the problem is the wide range of spatiotemporal scales required to fully account for all of the physical processes related to dust emission, transport, and deposition, and its interaction with topography. Models at coarse spatial resolution can resolve the synoptic scale events well; however, model limitations emerge in reproducing smaller-scale meteorological processes related to the dust emission. The small-scale emission processes have

become one of the biggest challenges in the framework of dust cycle studies (Shao et al., 2011; Knippertz and Todd, 2012; Knippertz and Stuut, 2014). To reduce the environmental impacts of sand and dust storms, most of the dust models focus on resolving from synoptic to mesoscale, the scales which have larger contributions to the total dust budget.

Within this framework, and following the lines of research of the Earth Sciences Department at BSC, the present Ph.D. thesis **aims to test the ability of a non-hydrostatic multiscale mineral dust model to reproduce the physical processes associated with the dust cycle at meteorological scales ranging from synoptic to mesoscale** (from 100 up to 1 km spatial resolution) over the geographical regions of Northern Africa, the Middle East and Europe (NAMEE). The mineral dust module of the NMMB-MONARCHv1.0 model, the NMMB/BSC-Dust model, is the main tool used in the present research.

To reach the general objective of this Ph.D. thesis, three specific modeling experiments have been designed to assess the skills of a state-of-the-art model to resolve those processes associated with the mineral dust life cycle under a range of spatial and meteorological scales. The first experiment focuses on analyzing the spatiotemporal scales associated with the dust cycle and demonstrating the model's consistency through a range of spatial scales through an annual cycle. The second experiment addresses how the model reproduces topographic effects on dust transport under two synoptic dust storms at regional scales. The third experiment investigates the model's ability to resolve convective dust storms.

The Ph.D. thesis is organized as follows. **Chapter 2** describes the main tool used in this work, the NMMB/BSC-Dust model, including the main features of its meteorological core (NMMB) and its dust module, such as the emission scheme, soil databases, and dry and wet deposition schemes. In **Chapter 3**, a multiscale analysis is performed from global to regional scales in Northern Africa, the Middle East, and Europe for an annual cycle to demonstrate the consistency of the model through a range of spatial scales and discuss the spatiotemporal variability of dust and its associated meteorological processes. **Chapter 4** presents an analysis of how the model reproduces the topographic effects and their impacts on dust transport over complex terrains under the occurrence of synoptic dust storms in the Middle East. The third study presented in **Chapter 5** focuses on the model's ability to reproduce convective dust storms and their involved meteorological processes. For that purpose, model runs are performed using explicit and parameterized convection. Finally, **Chapter 6** summarizes the most important findings of this Ph.D. thesis and gives recommendations for future works.

Chapter 2

2 The NMMB/BSC-Dust model

The NMMB/BSC-Dust is the mineral dust module of the Multiscale Online Non-hydrostatic AtmospheRe CHemistry model (NMMB-MONARCHv1.0; Pérez et al. 2011; Haustein et al. 2012; Jorba et al. 2012; Spada et al. 2013; Spada et al. 2015; Badia & Jorba 2015; Badia et al. 2016; Badia et al. 2017; Di Tomaso et al. 2017), which is under development at the ES-BSC department in collaboration with the National Centers for Environmental Prediction (NCEP) and the NASA Goddard Institute for Space Studies (NASA-GISS). The dust model is composed of the non-hydrostatic multiscale atmospheric NMMB model and the BSC-Dust dust module, both of them which are coupled online providing a unique framework to simulate and predict air quality and weather at a wide range of spatiotemporal scales. The following sections summarize the main features of the meteorological core and the dust module of the NMMB-MONARCHv1.0 model.

2.1 The NCEP Non-hydrostatic Multiscale Model on the B grid

The Non-hydrostatic Multiscale Model on the B grid (NMMB) is the meteorological core of the modeling system NMMB/BSC-Dust. The NMMB model is designed to run simulations of scales ranging from global to mesoscale in global and regional domains. It is designed to be highly efficient from the computational point of view and allows running multiple static and moving nests with one- and two-way interactions. Since October 2011, the regional NMMB has been operationally used at NCEP as the regional North American Mesoscale (NAM) model for providing weather forecasts over the whole North American domain (12 km horizontal resolution), within which also runs four static one-way nested domains (3-6 km horizontal resolution) in order to explicitly resolve convection.

For global runs, the model is formulated on the regular latitude-longitude grid by applying conservative polar boundary conditions and polar filtering, slowing down the tendencies of basic dynamic variables (Janjic, 2009; Janjic and Gall, 2012). Otherwise, for regional runs, the model uses rotated latitude-longitude grids to obtain more uniform grid distances. In both cases, the horizontal discretization is performed on the Arakawa B-grid (Arakawa and Lamb, 1977). In the vertical, the general hybrid sigma-pressure coordinate (Simmons and Burridge, 1981) is used with the Lorenz staggering. The “isotropic” horizontal finite volume differencing technique assures the conservation of a number of dynamical and quadratic quantities (among these are energy and enstrophy). More details about the numerical schemes of the NMMB are found in Janjic and Gall (2012).

A variety of physical schemes are implemented in the model, i.e. surface layer, grid-scale cloud microphysics, convective adjustment and precipitation, and radiation transfer schemes. Boundary layer and free atmosphere turbulence are parameterized using the Mellor-Yamada-Janjic (MYJ) turbulence closure scheme (Mellor and Yamada, 1982; Janjic, 2001). On the surface layer, the Monin–Obukhov

similarity theory (Monin and Obukhov, 1954) is applied (Janjic, 1996) in combination with a viscous sub-layer parameterization over oceans (Janjic, 1994). The wind speed at 10 m (U_{10}), which is the key parameter of dust production schemes, is computed consistently with the surface layer parameterization. The friction velocity (u*) is computed as the square root of the surface layer vertical momentum transport. Grid-scale clouds are parameterized with the scheme of Ferrier et al. (2002), including five prognostic cloud variables. The relevant quantities for the coupling with aerosol processes are the mixing ratios of both liquid and ice cloud water and their conversion rates to precipitation. For the treatment of moisture and heat surface fluxes, two land surface models are available in the model: the Noah (Ek et al., 2003) and the LISS (Vukovic et al., 2010) land surface model. The Betts-Miller-Janjic (BMJ) convective adjustment scheme (Betts 1986; Betts & Miller 1986; Janjic 1994; Janjic 2000) is used for the treatment of deep and shallow convection of the sub-grid scale clouds. Using conservational constraints, the convective clouds are represented by reference humidity and temperature profiles. Both water vapor mixing ratio and temperature are relaxed toward reference values within a convection time step. In the case of deep convection, the reference profiles and the relaxation time are governed by the cloud efficiency which depends on the convective regime. This is non-dimensional parameter obtained as a combination of entropy change, precipitation, and mean cloud temperature (Janjic, 1994, 2000). The triggering mechanism calculates the cloud base just below the lifting condensation level and the cloud top where the buoyancy approaches zero. For convective clouds, the precipitation produced is proportional to the full changes in humidity during the time step. The shallow convection (non-precipitating) parameterization closure uses the constraint that the entropy change must be non-negative (Janjic, 1994, 2000). The NMMB uses the operational Geophysical Fluid Dynamics Laboratory (GFDL) radiation package, which includes shortwave (Lacis and Hansen, 1974) and longwave (Fels and Schwarzkopf, 1975) schemes. Since the coupling with aerosols is not allowed by the operational GFDL scheme, the model also includes the Rapid Radiative Transfer Model (RRTM) scheme (Mlawer et al., 1997). By using RRTM, it is possible to couple both shortwave and longwave radiation and aerosols by providing aerosol optical depth, asymmetry factor, and single-scattering albedo (Pérez et al. 2011).

2.2 Mineral dust module

As indicated before, the NMMB/BSC-Dust (Pérez et al., 2011; Haustein et al., 2012) is the dust module of the NMMB-MONARCHv1.0 which is briefly described in this section according to its main features: emission, transport, and deposition. More details about the formulation of the mineral dust module are found in Pérez et al. (2011).

The dust emission scheme implemented in the model follows the empirical relationships of Marticorena & Bergametti (1995) and Marticorena et al. (1997) according to which the vertical dust

flux is proportional to the horizontal sand flux. The horizontal to vertical flux ratio (or sandblasting efficiency factor) reflects the availability of dust in four soil populations (i.e. clay, silt, fine-medium sand, and coarse sand; see Figure 2.1). These four categories are based on Tegen et al. (2002), which reformulated the State Soil Geographic database of the Food and Agriculture Organization of the United Nations (STATSGO-FAO) that shows 12 soil texture types according to the United States Department of Agriculture.

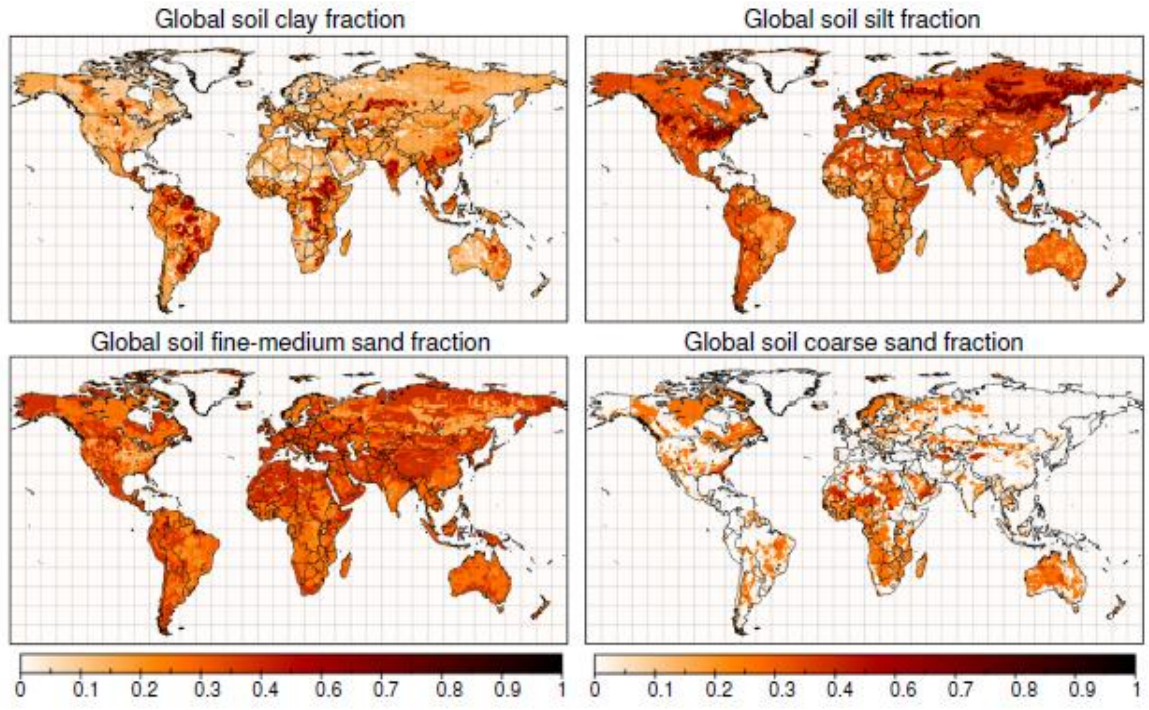

Figure 2.1: *Global soil texture fraction types for clay (0-2 μm), silt (2-5 μm), fine-medium sand (50-500 μm) and coarse sand (0.5-2 mm) according to 1 km STATSGO-FAO data. Extracted from Haustein (2011).*

The horizontal sand flux (H) is modeled as the flux of the saltating particles ($kg \cdot m^{-2} \cdot s^{-1}$), which is based on the formulation of White (1979) and considers dust saltation as proportional to the third power of the wind friction velocity u*. The soil particles begin to move in horizontal saltation flux above a given friction velocity, the threshold friction velocity u^*_{th} (Iversen & White 1982). This u^*_{th} depends on soil moisture based on the formulation of Fécan et al. (1999) as an increasing function of the clay fraction (% clay) on the ground, and it also depends on the size particles estimated according to soil characteristics (Iversen & White 1982).

The total vertical flux mass (F) is distributed in the model among 8 dust transport bins (between 0.10 and 10 μm in radius, F_k in Eq. 2.1) at intervals taken from Tegen & Lacis (1996) and Pérez et al. (2006). Each bin is assumed to be spherical, homogeneous (chemical composition of dust is not included), non-hygroscopic, and to have a time-invariant log-normal distribution (Zender et al., 2003),

a fixed geometric standard deviation of 2.0 (Schulz et al., 1998), and a fixed mass median diameter of 2.524 μm (Shettle, 1986). The version used in the present research considers d'Almeida (1987) which assumes that size particles distribute according to the 3 log-normal source modes i and then it distributes over the 8 dust transport bins k. As a result, the vertical flux of dust for each transport bin k (F_k) at each grid cell is given by:

$$F_k = C \cdot \delta \cdot \alpha \cdot H \cdot \sum_{i=1}^{3} m_i \cdot M_{i,k} \quad ; \quad k = 1, \ldots, 8 \tag{2.1}$$

where C is a calibration factor, which is introduced for minimizing the difference between model results and observations. The source function δ (varies from 0 to 1; see Figure 2.2d) is calculated considering grid's fraction of bare soil (see Figure 2.2a) based on the 1 km United States Geological Survey (USGS) land use data (Anderson et al., 1976; Loveland and Belward, 1997), the vegetation cover fraction (Figure 2.2b), which is given by a 5-year (1985–1990) monthly NDVI climatology extracted from National Environmental Satellite, Data, and Information Service (NESDIS) database (Ignatov and Gutman, 1998), and the topographic preferential source approach from Ginoux et al. (2001) (see Figure 2.2c).

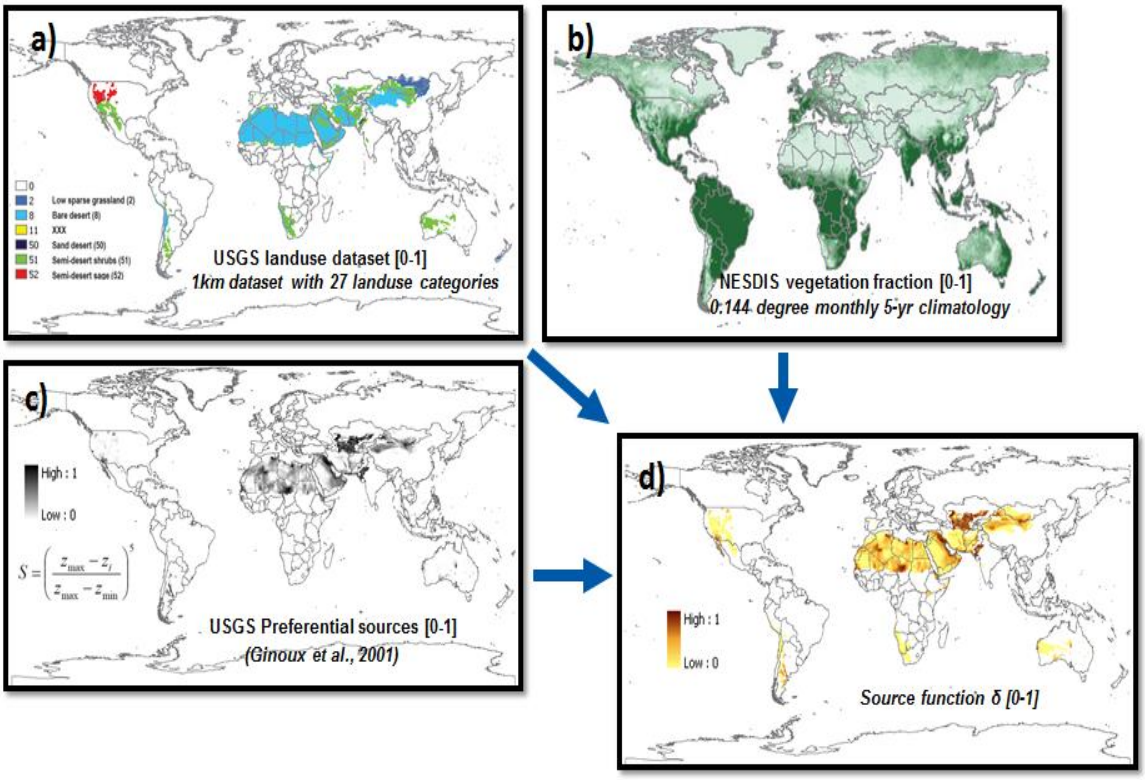

Figure 2.2: *(a) The USGS land use with 27 categories at 1 km horizontal resolution, (b) USGS Preferential source at 0.25º horizontal resolution, and (c) NESDIS vegetation climatology (1985-1990) at 0.144º horizontal resolution, are included in (d) the source function (δ) at 0.25º horizontal resolution.*

Following the terms of Eq. 2.1, α is the horizontal to vertical flux ratio (or sandblasting efficiency factor) calculated for four soil population classes (i.e. clay, silt, fine-medium sand, and coarse sand), H is the horizontal sand flux, m_i is weighted by a specific background source mode coefficient, and finally, $M_{i,k}$ is the mass fraction of source mode i carried in a transport bin k calculated following Zender et al. (2003).

Once the dust is emitted, transport of dust by advection and turbulent diffusion is analogous to those of the moisture transport in the NMMB meteorological model. Furthermore, the model includes the treatment of the dry and wet removal processes of atmospheric dust. The dry deposition of the first layer of the model is based on the scheme of Zhang et al. (2001), which includes simplified empirical parameterizations for the deposition processes of Brownian diffusion, impaction, interception, and gravitational settling (Slinn, 1982). Otherwise, the model includes both in- and sub-cloud removal scavenging processes using the scheme of Ferrier et al. (2002), which involves different microphysics parameterizations for grid-scale clouds and the BMJ convective adjustment scheme for the subgrid-scale clouds. Theses in-cloud and sub-cloud scavenging processes consider several cloud variables, including liquid precipitation rate, and the efficient capture of raindrops, which depend on the diameter of the raindrops and dust particle size, as well as Brownian diffusion, impaction and interception processes (Slinn, 1984).

Chapter 3

3 Dust life cycle consistency of a mineral dust model from global to meso scales

3.1 Background

Monitoring the parameters involved in the dust cycle is essential to better understand its spatial and temporal processes and to gain more knowledge about the impact of dust. Nevertheless, observations are limited by the low number of ground stations, particularly near dust sources, and by the decreased accuracy of satellite retrievals in thick dust layers, over bright surfaces or below clouds (Kocha et al., 2013). In this scenario, dust models are necessary to complement observations because they can provide information on areas not covered by stations and can also help to understand the various aspects that control distributions of dust concentrations and its impacts.

Annual dust emission estimates for Northern Africa and the Middle East are, on average, 792 and 128 Tg, respectively based on the global models from AEROCOM (Huneeus et al., 2011; IPCC, 2013). However, these emission estimates are still uncertain due to the nonlinear relationship of the dust emissions with wind speed and soil conditions. Surface wind fields are used to compute emission fluxes must be available at appropriate spatiotemporal resolution (from synoptic to mesoscales and microscales) to resolve the processes responsible for dust emission (Shao et al., 2011). The clarification of the role of smaller-scale meteorological processes on the dust emission and their contribution to the global aerosol budget has become one of the biggest challenges in the framework of dust cycle studies (Shao et al., 2011; Knippertz and Todd, 2012; Knippertz and Stuut, 2014). A diversity of atmospheric-dust model systems are available for the large eddy simulation (LES) scale (e.g. Klose & Shao 2013), the regional scales (e.g. Nickovic et al. 2001; Todd et al. 2008; Morcrette et al. 2009; Pérez et al. 2011), and the global scale (e.g. Ginoux et al. 2001b; Morcrette et al. 2009; Haustein et al. 2012; Ridley et al. 2012), which altogether cover the wide range of meteorological scales at which dust processes occur. Here the problem arises that these model systems are only resolving particular scales with their specific model physics, leading to uncertainties in the total dust concentration estimates.

The work presented in this chapter focuses on the analysis of the spatiotemporal scales associated with the dust cycle over the Northern Africa and the Middle East domain using a multiscale state-of-the-art dust model, the NMMB/BSC-Dust (Pérez et al. 2011) described in Chapter 2. The NMMB/BSC-Dust model offers the possibility to overcome the inconsistency between spatiotemporal scales as it uses a unified non-hydrostatic dynamical core applicable from sub-synoptic to the mesoscales. The aim of this study is twofold: (1) to discuss the spatiotemporal distribution of dust sources as well as the specific meteorological conditions associated with dust emission that occurs at various spatiotemporal scales (from synoptic to mesoscale) and involves different meteorological phenomena, and (2) to demonstrate the consistency of the model results along the different spatiotemporal scales. To achieve

this, three simulations with the NMMB/BSC-Dust model are performed for an annual cycle (2011) over Northern Africa, the Middle East, and Europe (NAMEE) domain, covering a wide range of spatial resolutions (1º, 0.25º, and 0.10º). The model is evaluated using a set of ground-based and satellite observations (i.e. dust concentration and surface meteorological fields). This chapter is organized as follows. Section 3.2 presents the model setup, and Section 3.3 includes a description of the ground-based and satellite observations and methods used for the model evaluation. In Section 3.4, we analyze the model outputs and compare them with the available observations. Finally, section 3.5 summarizes the most important findings of the present study.

3.2 Model setup

The present study uses three configurations of the NMMB/BSC-Dust model (see Table 3.1) with horizontal resolutions of 1.4ºx1º (about 110 km at Equator; hereafter referred to as GLOB) on a global domain, and 0.25ºx0.25º (about 27 km at Equator; hereafter referred to as R25) and 0.10ºx0.10º (about 11 km at Equator; hereafter referred to as R10) both on a regional domain covering NAMEE region (0º-65ºN to 25ºW-65ºE; see Figure 3.1). These configurations use 40 σ-layers as vertical resolution with the top of the atmosphere set at 50 hPa, and the temporal resolution of the model outputs is 3-hourly. The simulated dust and meteorological fields consist of daily runs (24-hours of hindcast) from 1 January to 31 December 2011 which are initialized with meteorological NCEP/Final Analysis (FNL; 1ºx1º horizontal resolution) at 0 UTC, and boundary conditions for the regional domains are updated every 6 h. The model does not include dust data assimilation and the initial state of the dust variables is defined by the 24-h of the previous-day model run, except in the 'cold start' of the model simulation (on 27 December 2010 at 0 UTC) when dust concentration is zero. The meteorological parameterizations used are the RRTM radiative scheme, LISS land model, Ferrier microphysics scheme, BMJ convective scheme, and Mellor-Yamada-Janjic boundary layer scheme. All model configurations use a unique calibration factor in the model's emission scheme of 0.255.

Table 3.1*: Model configurations of the NMMB/BSC-Dust model used in the present chapter: horizontal resolution, horizontal grid points, domain (latitude and longitude ranges), and fundamental time steps.*

Configuration	GLOB	R25	R10
Horizontal resolution	1.4º x 1.0º	0.25º x 0.25º	0.10 ºx 0.10º
Horizontal grid points	257x181	409x281	1021X701
Domain (Lat & Lon ranges)	Global	NAMEE	NAMEE
	-	0º-70ºN & 31ºW-71ºE	0º-70ºN & 31ºW-71ºE
Fundamental time step (s)	180	40	25

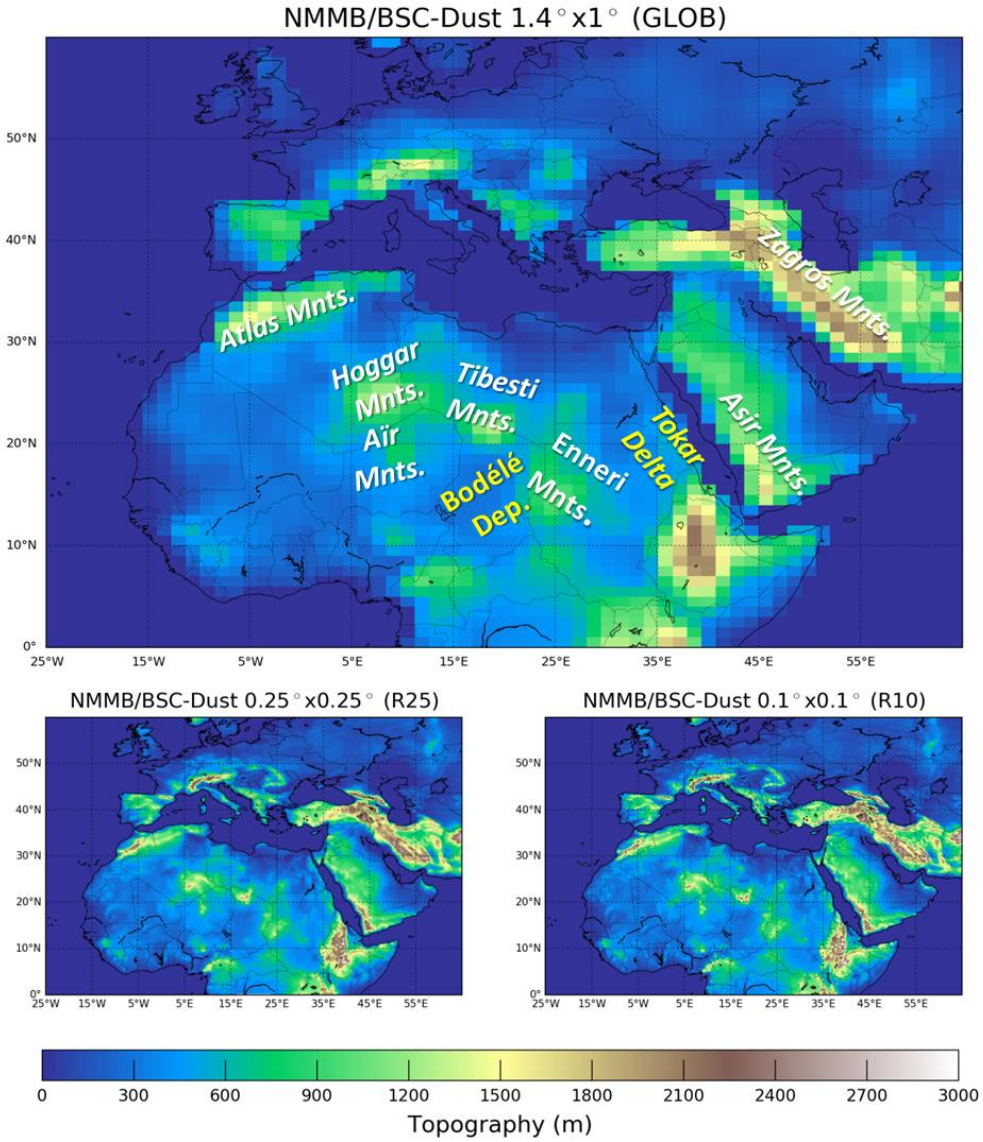

Figure 3.1*: Topography of the study domain at GLOB (top panel), R25 (bottom-left panel) and R10 (bottom-right panel). The top panel includes locations used in the present chapter.*

3.3 Observational data

3.3.1 Surface weather observations

The Integrated Surface Hourly (ISH) database (https://www.ncdc.noaa.gov/isd) archived at the National Climatic Data Center (NCDC) includes hourly meteorological data, mainly composed of the surface synoptic observations (SYNOP) and the meteorological aerodrome report (METAR). These stations are sparse in deserts and generally found in airfields or urban areas. The default time resolution tends to be 3-hourly in SYNOP stations and hourly in METAR stations, although it can vary depending on location such as in the Sahara and the Sahel, where observations are only available at certain hours of the day. Simulated wind speed and direction at 10 m are evaluated against more than

1000 stations in our area of study (NAMEE; see Figure 3.2). For the present study, only those stations reporting at least four hours per day coinciding with the 3-hourly model outputs are considered and with high data availability during all seasons (> 75%).

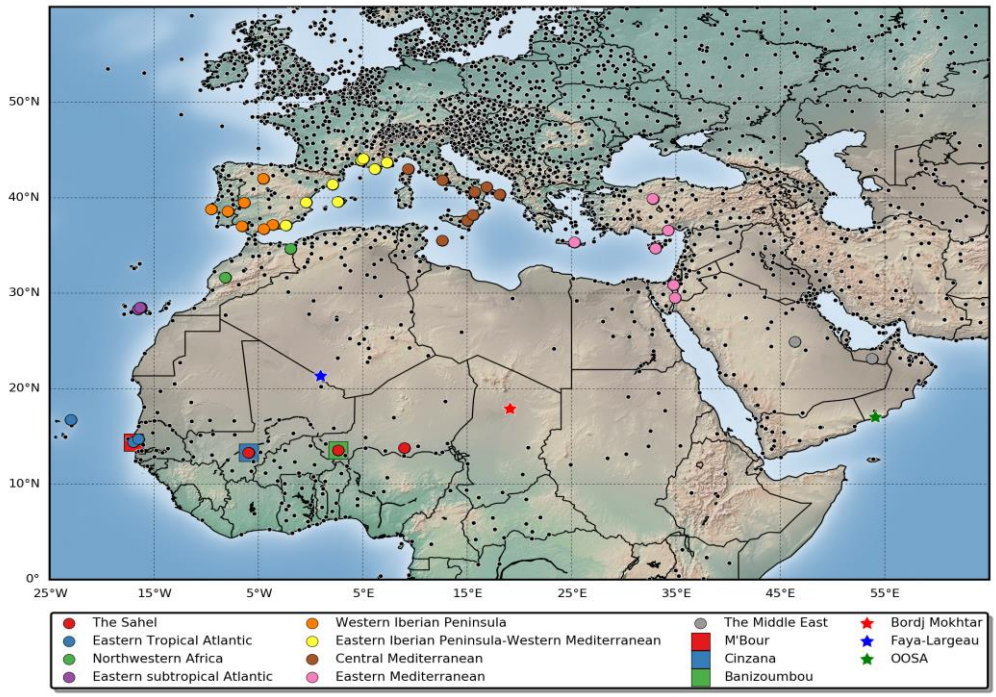

Figure 3.2*: The location of the sites is shown as follows: ISH sites (black dots), except three ISH sites (star shape dots), the three AMMA PM10 sites in the Sahel (square shape dots), and the 42 AERONET stations (circle shape dots with a color per region), which are grouped by regions: the Sahel, Eastern Tropical Atlantic-North Atlantic, Eastern subtropical-North Atlantic, Northwestern Africa, Western Iberian Peninsula, Eastern Iberian Peninsula-Western Mediterranean, Central Mediterranean, Eastern Mediterranean, and the Middle East.*

3.3.2 Aerosol optical depth

Aerosol optical properties routinely observed with AERONET sun-photometers (Holben et al., 1998; Smirnov et al., 2000) are used in the model comparison of the dust optical depth (DOD). These instruments rely on extinction measurements of the direct and scatter solar radiation at several nominal wavelengths (between 340 to 1020 nm). The uncertainty of aerosol optical depth (AOD) retrievals, under cloud-free conditions, is less than 0.02 (Holben et al., 1998; Dubovik et al., 2002).

Dust-filtered AERONET quality-assured Version 2 observations from 42 stations (see Figure 3.2) are used for the quantitative model evaluation. To allow the comparison with model results at a standard reference wavelength of 550 nm, AOD observations are extrapolated for a wavelength of 550 nm through, which is calculated using channels 440 and 870 nm and following the Ångström's law. All of the AERONET measurements available within ± 90 min around the 3-hourly model outputs have been averaged, although only those that are associated with desert dust aerosols (i.e. high extinction and coarse-particle dominated fraction) are considered. Following the aerosol characterization over

NAMEE from Basart et al. (2009), aerosol data with the Ångström's exponent between 440 and 870 nm (AE) < 0.75 is considered as dust optical depth (DOD). All data with AE > 1.2 is associated with fine anthropogenic (and non-dust) aerosols, and it is consequently described as observed DOD of 0. Measurements outside these AE ranges are associated with mixed aerosols and are not considered in quantitative model evaluation (see Section 3.3.4). In this work, the selected AERONET stations are grouped into nine regions for analysis purposes (see Figure 3.2): the Sahel, Eastern Tropical Atlantic-North Atlantic, Eastern subtropical-North Atlantic, Northwestern Africa, Western Iberian Peninsula, Eastern Iberian Peninsula-Western Mediterranean, Central Mediterranean, Eastern Mediterranean and the Middle East.

In addition to the quantitative AERONET comparison, we also use satellite aerosol products to complement the sparse ground-based observations and provide relevant information about dust distribution over a wide spatial range. Multi-angle Imaging Spectro-Radiometer (MISR) can retrieve aerosol properties like AOD over a variety of terrain, including highly reflective surface like deserts (MISR Team, 2015). MISR orbits repeat time is three or four visits per month over the Sahara. The Moderate Resolution Imaging Spectro-Radiometer (MODIS) AOD algorithm is comprised of two independent algorithms: Dark Target for ocean and land, except in bright surfaces such as deserts, and Deep Blue for bright land surfaces such as deserts (Levy et al., 2013). In the present analysis, we use the MISR Version 3.1 AOD (at 555 nm) global gridded monthly averages (at 0.5º x 0.5º horizontal resolution) as well as the MODIS Collection 6 AOD (at 550 nm) global gridded monthly averages (at 1º x 1º horizontal resolution) on board of Terra and Aqua satellites, which provide twice-daily global coverage.

As shown by the satellite data in Figure 3.3, differences are observed between MODIS and MISR- This fact is linked to the lower MISR observation frequency compared to MODIS overpasses. While its temporal resolution is high enough to capture the major seasonal dust activity, its temporal resolution is too low to reproduce some regional features. For example, over West Africa in spring and summer when dust activity is higher, MISR shows some hot spots that MODIS does not show, which is probably because MISR passes were coincident with the occurrence of strong dust storms. Meanwhile MODIS, which represents a larger number of observations, also included a higher number of calm days, therefore reducing its seasonal mean AOD. Also, MODIS shows a high hot spot in the Bodélé Depression, which is because the MODIS Deep Blue product usually overestimates AOD values over a bright surface.

3.3.3 Surface PM10 concentrations

In the framework of the African Monsoon Multidisciplinary Analysis (AMMA) program, there are three ground-based stations (Figure 3.2) in the Sahelian Dust Transect, located in M'Bour (Senegal),

Cinzana (Mali) and Banizoumbou (Niger), which are deployed to obtain surface PM10 and its variability over the Sahel. The stations are aligned around the 14ºN parallel under the main Northern African dust transport pathways towards the Caribbean. In order to avoid non-dust aerosols such as sea-salt and biomass burning in the PM10 data and select the sector affected by mineral dust, a filter is applied by wind direction (WD), which is also available on each site and station, as follows: M'Bour ($30^o < WD < 150^o$), Cinzana ($90^o < WD < 270^o$), and Banizoumbou ($90^o < WD < 270^o$). Detailed descriptions of the AMMA stations, the dataset, and the filtering process of data are provided by Marticorena et al. (2010). Despite this filter, non-dust aerosols can still affect the monitored PM10 mass, for example, aerosols from biomass burning and mixed aerosols in winter in the three stations, as well as sea-salt and anthropogenic aerosols (also mixed aerosols) in M'Bour site due to its proximity to the ocean and urban areas (e.g. Dakar or M'Bour cities) (Marticorena et al., 2010; Cuevas et al., 2015; Mortier et al., 2016). Hourly dust-filtered PM10 values that are coincident with the 3-hourly model outputs are selected for the model evaluation.

3.3.4 Statistics for quantitative evaluation

To quantitatively evaluate the performance of the three model configurations (GLOB, R25 and R10; see Section 3.2), a set of statistics such as correlation coefficient (r), mean bias (MB), mean absolute error (MAE), and root mean square error (RMSE) are used for evaluating the skill of the model on annual, seasonal and monthly basis. Ground-based observations from DOD (from AERONET), dust-filtered PM10 (from AMMA), and wind speed at 10 m (from ISH) are used for a quantitative model evaluation against the respective simulated variables, which have been extracted from coincident model outputs (on 3-hourly basis) using bilinear interpolation methods in the station locations.

3.4 Results and discussion

Satellite AOD observations show a marked seasonal variability over the study region (Figure 3.3). This dust variability is mainly driven by the latitudinal shift of the Inter-tropical Convergence Zone (ITCZ) between the northerly Harmattan and the southerly monsoon winds. The model (in each configuration) reproduces the seasonal variability of the satellite observations and the typical seasonal transport patterns such as the westward African transport towards the North Atlantic and its latitudinal shift throughout the year, the northerly African transport towards the Mediterranean basin in spring and summer, and the dust distribution through the Red and Arabian Seas from spring to summer (Figure 3.3). Satellites observe high AODs (> 1; Figure 3.3) that the model is not able to capture. Some of these high AOD values are linked to the presence of non-dust particles that the dust model is not considering, such as particles from the forest and savannah fires over the Gulf of Guinea and the Sahel in winter (Basart et al., 2009; Schepanski et al., 2012), from domestic and commercial charcoal,

industrial activities in some Northern African cities (e.g. Rodríguez et al. 2011), and the petroleum industry over the Persian Gulf (Basart et al., 2009). Overall, the simulated DOD at source regions and over the main transport pathways (e.g. the North Atlantic, the Arabian Sea) is generally weaker (particularly in summer) than those observed by the satellites, except in the Central Sahara-Sahel sources during spring (see Figure 3.3). This column-load distribution follows the surface concentrations (Figure 3.4). Differences between DOD (Figure 3.3) and dust surface concentration (Figure 3.4) fields are linked to the seasonal variation in the height of dust transport layer. In the next sections, a detailed analysis is presented per regions.

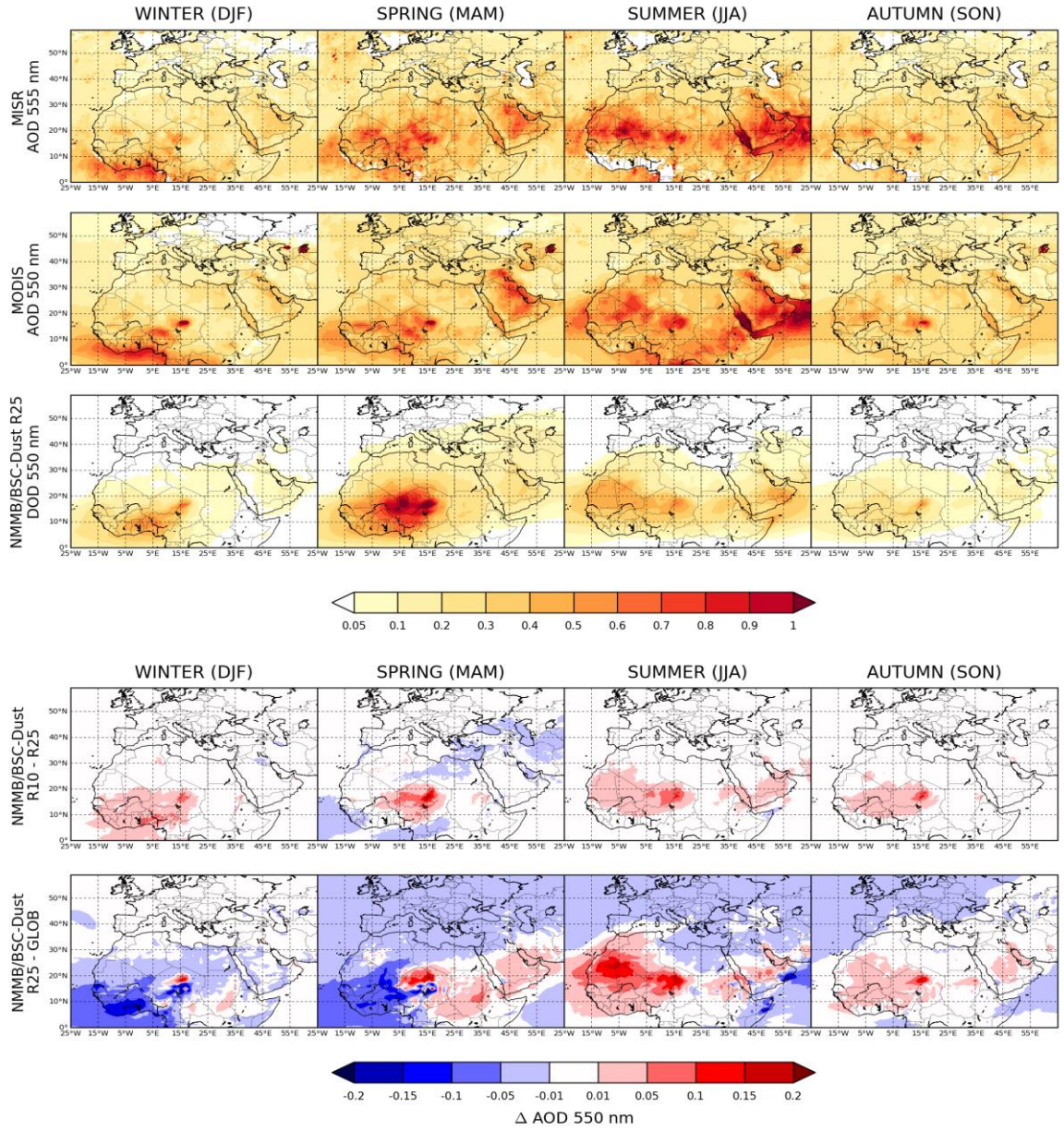

***Figure 3.3**: Seasonal average of Aqua and Terra/MODIS AOD 550 nm (1st row) at 1ºx1º horizontal resolution, Terra/MISR AOD 555 nm (2nd row) at 0.5ºx0.5º horizontal resolution, and simulated dust optical depth (DOD) at 550 nm at 0.25ºx0.25º horizontal resolution (R25; 3rd row), and the differences between configurations: 0.10ºx0.10º - 0.25ºx0.25º (R10-R25; 4th row) and 0.25ºx0.25º - 1.4ºx1º (R25-GLOB; 5th row).*

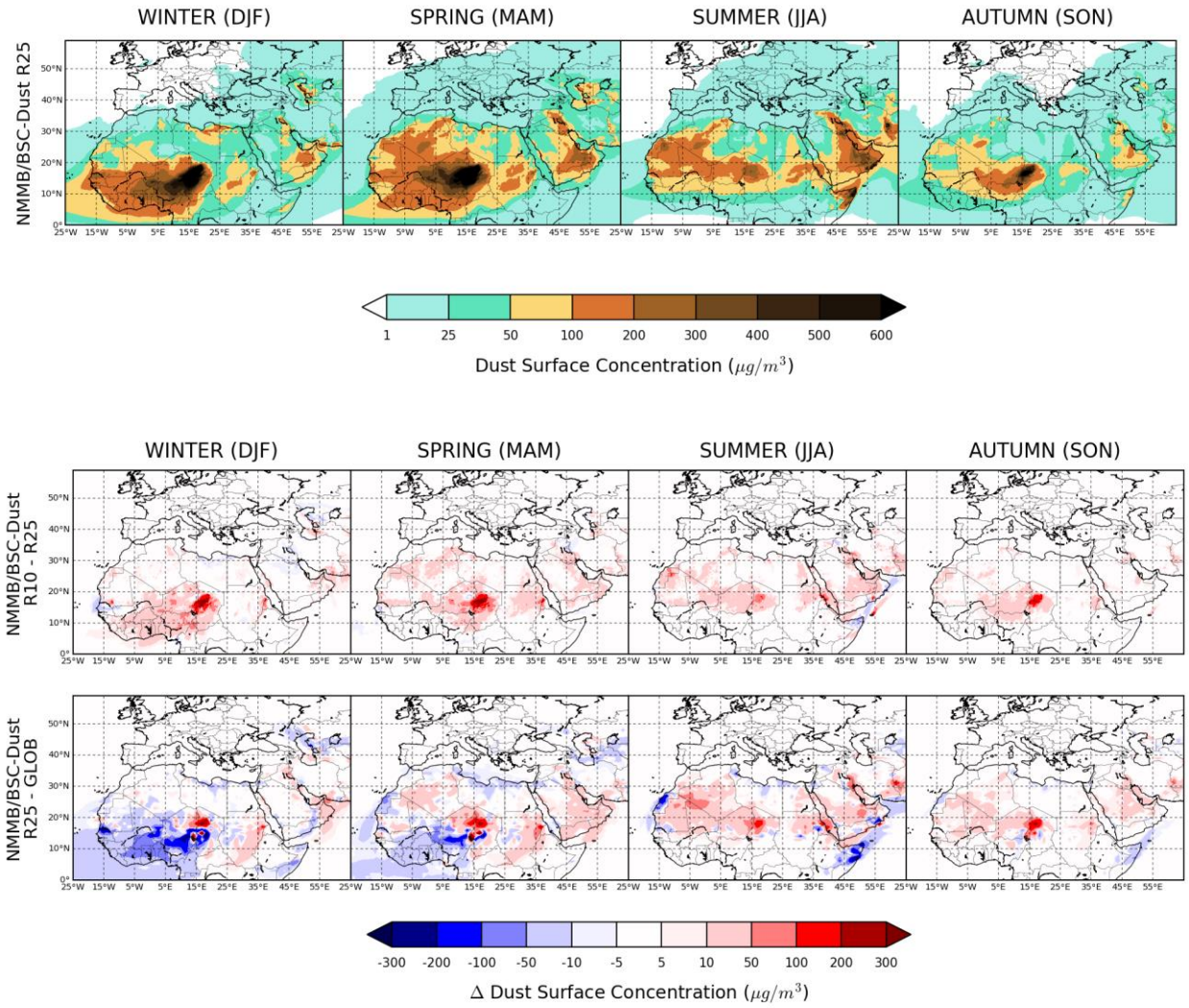

***Figure 3.4**: Seasonal surface dust concentration at 0.25ºx0.25º horizontal resolution (R25; 1st row), and the differences between configurations: 0.10ºx0.10º - 0.25ºx0.25º (R10-R25; 2nd row) and 0.25ºx0.25º - 1.4ºx1º (R25-GLOB; 3rd row).*

3.4.1 Desert dust source regions

3.4.1.1 Sahara-Sahel

In Northern Africa, maximum DOD concentrations (Figure 3.3) are found in the winter and spring months when the Harmattan winds are predominant over the Central Sahara-Sahel sources, such as in the Bodélé Depression (Chad). During summer, dust activity progressively grows under the presence of southern winds at higher latitudes, such as the Algeria-Niger-Mali and the Mali-Mauritania borders, and eastern Sudan. The model (in each configuration) reproduces the seasonal variability of the DOD observed by the satellites and the typical seasonal transport patterns such as the westward African transport towards the North Atlantic and its latitudinal shift throughout the year, although modeled DOD fields appear underestimated during summer in comparison with satellites. A noticeable

consistency is seen between model configurations. The 3-hourly values of modeled and observed dust mainly vary in terms of DOD between 0.5 and 2.0 (see Figure 3.5a), and in terms of PM10 from 10 to 1500 $\mu g/m^3$ (see Figure 3.7a and b), although under specific strong dust events DOD values can overpass these ranges achieving values of up to 3 for individual sites. Higher dust emissions in winter and early spring in the South of the Central Saharan mountains (such as the Hoggar, Tibesti and Enneri mountains) are found at coarser horizontal resolutions than R10 (Figure 3.6a and b), which represent more smoothed and lower topographies (Figure 3.1) that do not block or break the Harmattan winds. On the contrary, higher dust emission in the vicinities of the Central Saharan mountains is found at higher horizontal resolutions than GLOB by topographic wind acceleration over dust sources. From late spring and summer, Northern African emission between configurations increases at a higher resolution by a stronger representation of the breakdown of the nocturnal low-level Jet (NLLJ) and its associated wind peak. Almost half of the annual Northern African emissions occur at 9-12 UTC (Figure 3.6c), when the Bodélé Depression shows its peak of emission and wind, as can be seen from the surface weather station in Faya-Largean (Chad) (Figure 3.8). This large morning contribution to emission ratio and timing is in agreement with Fiedler et al. (2013).

Seasonal variability in the Sahel is marked by two main periods (see DOD in Figure 3.3 and surface dust concentration in Figure 3.4): (1) dry season (from late February to May) when the northeasterly Harmattan winds are maximum and they cause the low-level dust transport from the Central Sahara to the Sahel and westwards, and (2) wet season (from June to August), when more predominant southwesterly monsoon winds from the South favors the precipitation in the region, causing a gradual decrease of dust concentrations, although with occasional short-lived peaks (see Figure 3.7a and b in June). Different behaviors between the simulated DOD (Figure 3.3) and surface dust concentration (Figure 3.4) are found by the seasonal variation in the dust transport layer over the Sahel with a maximum height up to 5 km in summer and 3 km in winter (not shown here).

Over the grouped AERONET stations in the Sahara-Sahel (see Figure 3.2), the model reproduces reasonably well the annual DOD variability (Figure 3.5a) with annual correlations of 0.58 for GLOB, 0.62 for R25 and 0.6 for R10. On an annual basis, no significant differences are found between configurations in terms of MB (-0.01 for GLOB, -0.03 for R25 and 0 for R10) and RMSE (0.37 for GLOB, 0.33 for R25 and 0.36 for R10). During spring, the model overestimates the AERONET observations (Figure 3.5a) with MB as follows: 0.19 for GLOB, 0.14 for R25 and 0.15 for R10. For the whole year, spring presents the maximum monthly DOD overestimations in May for GLOB with MB of 0.45, in May and March for both R25 and R10 with similar peaks of MB of 0.17-0.19 and of 0.18-0.2, respectively. In summer, the model underestimates the AERONET observations (Figure 3.5a) with MB as follows: -0.17 for GLOB, -0.15 for R25 and -0.09 for R10.

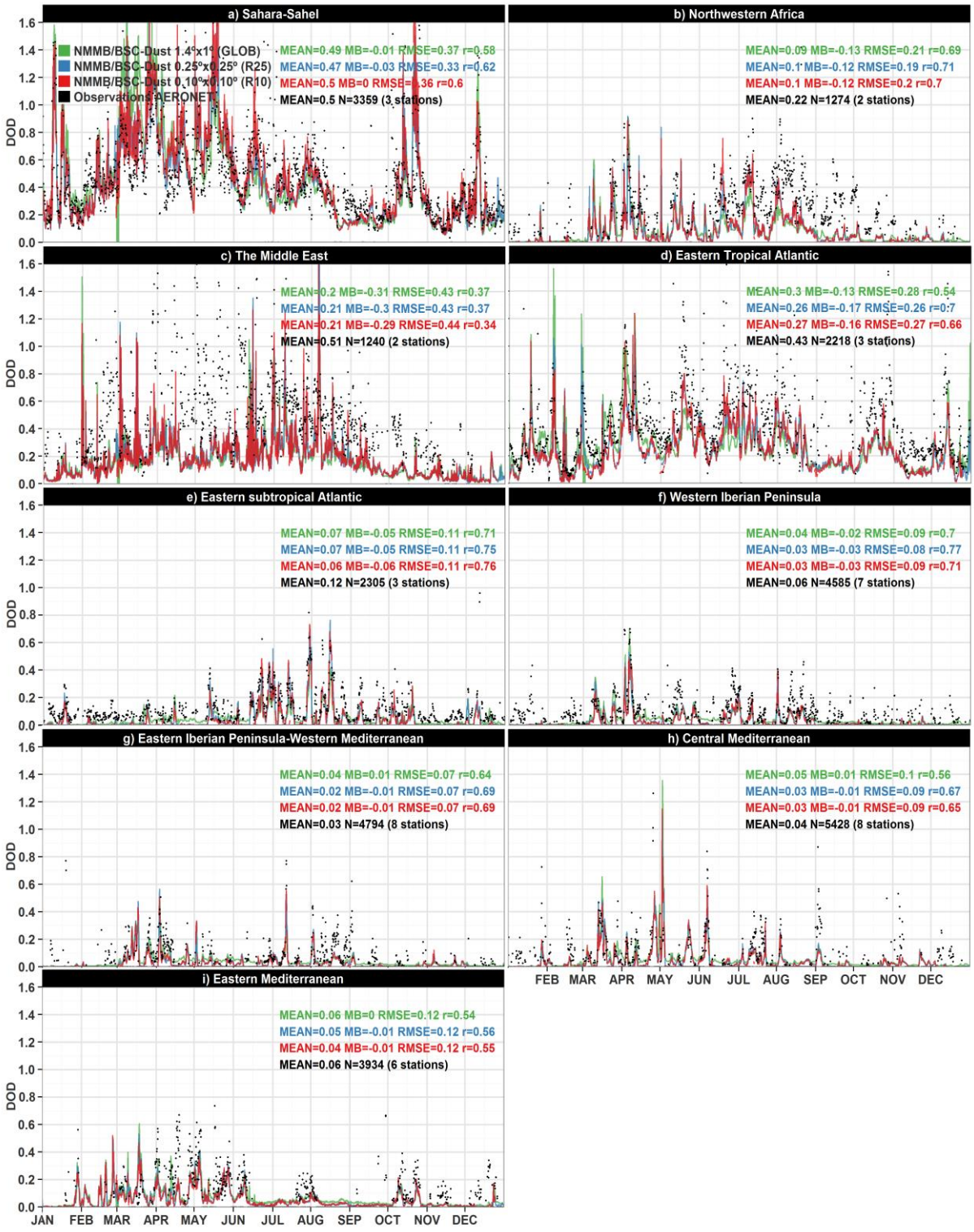

Figure 3.5: *Time series (on 3-hourly basis) of the simulated DOD for GLOB (NMMB/BSC-Dust 1.4ºx1º; green lines), R25 (NMMB/BSC-Dust 0.25ºx0.25º; blue lines) and R10 (NMMB/BSC-Dust 0.10ºx0.10º; red lines) and AERONET dust-filtered AOD observations (black dots). Observations are grouped per region depicted in Figure 3.2. Each plot includes the used number of values (N), the annual simulated and observed mean per configuration and a set of statistics computed between observed and simulated DOD as follows: mean bias (MB), root mean square error (RMSE) and the correlation coefficient (r).*

The modeled PM10 surface concentration shows a good agreement with PM10 AMMA observations in the Sahel (Banizombou and Cinzana in Figure 3.7a and b) and it reproduces most of the dust activity with higher PM10 values in winter and lower values in summer, except for short and fast peaks of PM10 (associated with haboobs) that commonly appear in late spring and summer (see June-July in Figure 3.7a and b). The correlation coefficients are annually controlled by the wet season due to its much higher number of filtered observations than the dry season (in summertime data filtering leaves less than 25% of the total available data), although both seasons are marked by different model performances. Banizoumbou (with a mean observed PM10 of 174 $\mu g/m^3$) is the site with higher correlations (0.78, 0.74 and 0.71 for GLOB, R25 and R10, respectively), especially at GLOB due to higher contribution of the transported dust than R25 and R10, although the model highly overestimates the surface concentrations during winter and spring for the three configurations, especially in January (when MB > 250 $\mu g/m^3$ and RMSE > 600 $\mu g/m^3$). This is associated with a significant overestimation of dust emission from the Central Saharan sources (e.g. the Bodélé Depression) that are transported near the ground to the Sahel (up to 3 km in height). Among configurations similar results are obtained in the Banizoumbou site, although GLOB (MB = 152 $\mu g/m^3$ and RMSE = 342 $\mu g/m^3$) shows a slightly higher overestimation due to the higher dust transport to the Sahel, especially in March, in comparison with R25 (MB = 109 $\mu g/m^3$ and RMSE = 308 $\mu g/m^3$) and R10 (MB = 129 $\mu g/m^3$ and RMSE = 365 $\mu g/m^3$) on an annual basis. Cinzana (with a mean observed PM10 of 105 $\mu g/m^3$), further west of Banizoumbou and less affected by the high Central Saharan emissions, is the station where the model presents the lowest annual errors and slight differences between configurations such as MB (26, 9 and 2 $\mu g/m^3$ for GLOB, R25, and R10, respectively) and RMSE (139, 109, and 105 $\mu g/m^3$ for GLOB, R25, and R10, respectively) as well correlations of 0.58, 0.61, and 0.64 for GLOB, R25, and R10, respectively.

In springtime, DOD overestimations observed in the Sahel (see Sahara-Sahel in Figure 3.5a) in the AERONET comparison are partly linked to wind overestimation of the Harmattan winds, which is reported by some surface weather stations, such as Bilma (Niger; not shown here) and Faya-Largeau (Chad; see Figure 3.8), with hourly mean wind overestimations up to 2 m/s, especially at some diurnal hours and in May. The highest monthly DOD overestimation in the Sahara-Sahel is observed in GLOB on March, which can be partly caused by a slightly mean wind speed overestimation (around 0.5 m/s) at 12 UTC over the Bodélé Depression, as shown in the Faya-Largeau site (see Figure 3.8). Based on Fiedler et al. (2013), the Bodélé Depression is a hot spot for the occurrence of the breakdown of the NLLJ between November and March. Over the region, this mechanism produces a maximum wind value at about 9 UTC, which is consistent with the model configurations and generally intensifies at finer spatial scales (from GLOB to R10), as shown by wind stations and the mid-morning emission peak (Figure 3.8).

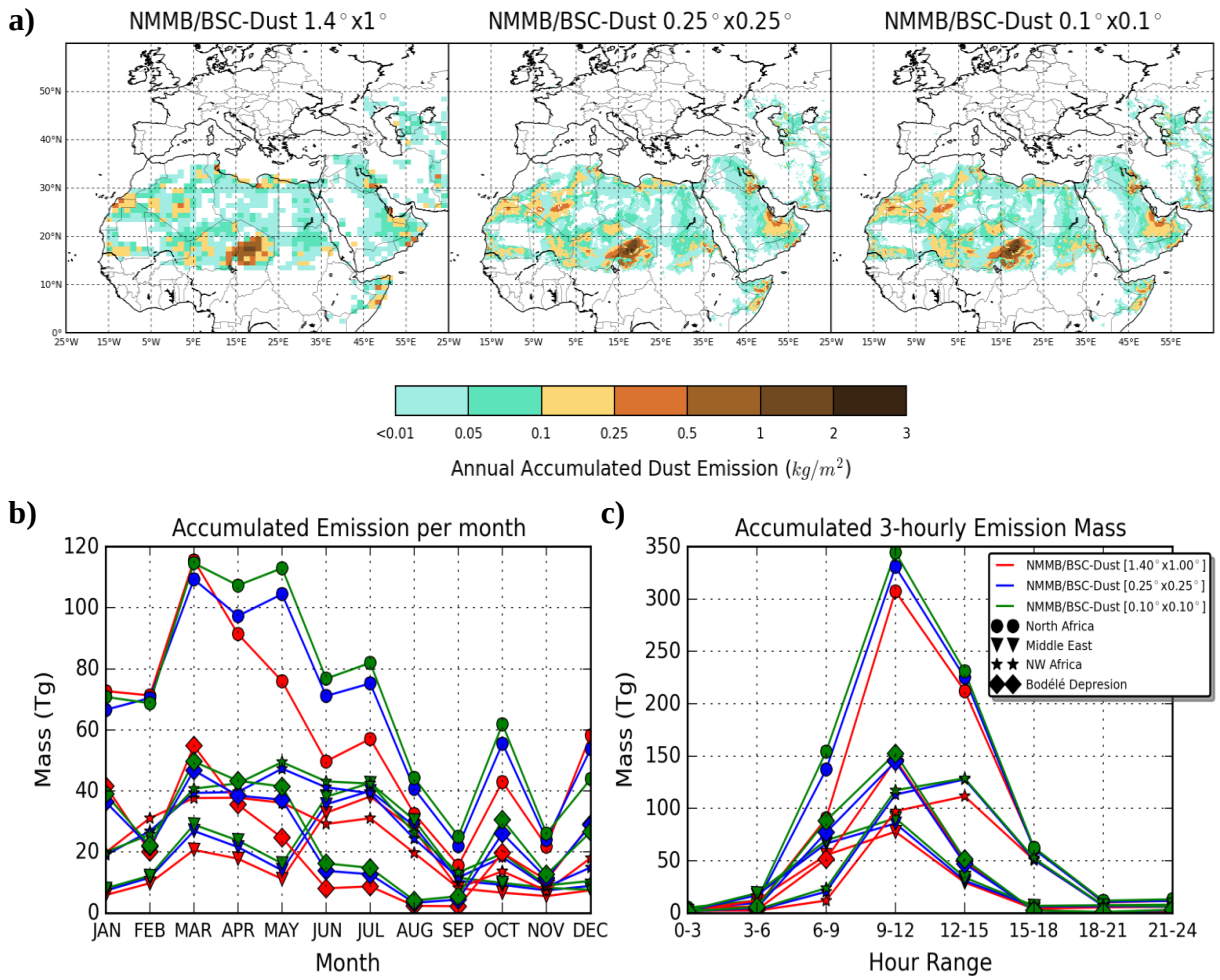

***Figure 3.6**: (a) Annual accumulated dust emission for the NMMB/BSC-Dust with horizontal resolutions of 1.4ºx1º (GLOB; left), 0.25ºx0.25º (R25; middle) and 0.10ºx0.10º (R10; right), and (b) monthly accumulated emission and (c) 3-hourly accumulated emission both for Northern Africa (0º-40ºN to 25Wº-35Eº; circles), the Middle East (10ºN-40ºN to 35ºE-65ºE; triangles), NW Africa (15ºN-40ºN to 25ºW-12ºE; stars), and the Bodélé Depression (10ºN-20ºN to 12ºE-20ºE; diamonds), which are differentiated by dot shape, and for horizontal resolutions of 1.4ºx1º (GLOB; red lines), 0.25ºx0.25º (R25; green lines) and 0.10ºx0.10º (R10; green lines).*

Otherwise, DOD underestimations in all configurations are observed in summer in the AERONET and satellite comparison. These underestimations may be partly caused by the meteorological and soil initial conditions (i.e. the NCEP/FNLs) used in the model run. These underestimations have associated the highest uncertainties over the Sahara because of the lack of observations to be assimilated and the high sensitivity of the model's emission scheme to the soil moisture (Haustein et al., 2015). Furthermore, the latitude movement of the ITCZ up to 20º N (not shown here) contributes to increase soil moisture by rainfall, which is especially stronger and at higher latitudes in July and August, and then it can also inhibit or reduce dust emissions.

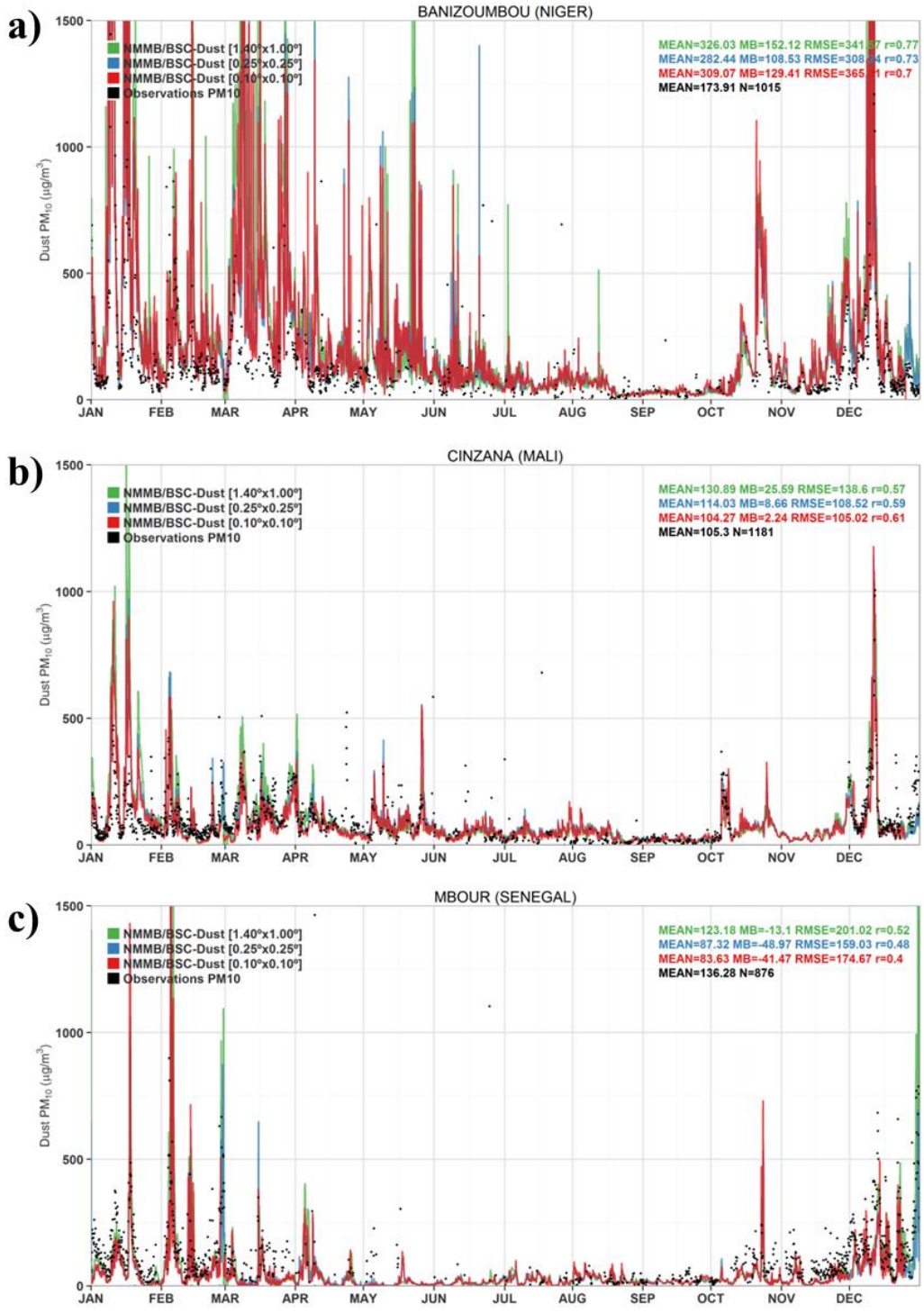

Figure 3.7*: Time series (on 3-hourly basis) of the simulated dust PM10 for GLOB (NMMB/BSC-Dust 1.4ºx1º; green lines), R25 (NMMB/BSC-Dust 0.25ºx0.25º; blue lines) and R10 (NMMB/BSC-Dust 0.10ºx0.10º; red lines) and AMMA filtered PM10 observations (black dots) per station as follows: (a) Banizoumbou, (b) Cinzana, and (c) M'Bour (see their location in Figure 3.2). Each plot includes annual simulated mean per configuration and a set of statistics computed between observed and simulated DOD as follows: mean bias (MB), root mean square error (RMSE) and the correlation coefficient (r). Also, the number of observed values (N) and the annual observed mean is included in black.*

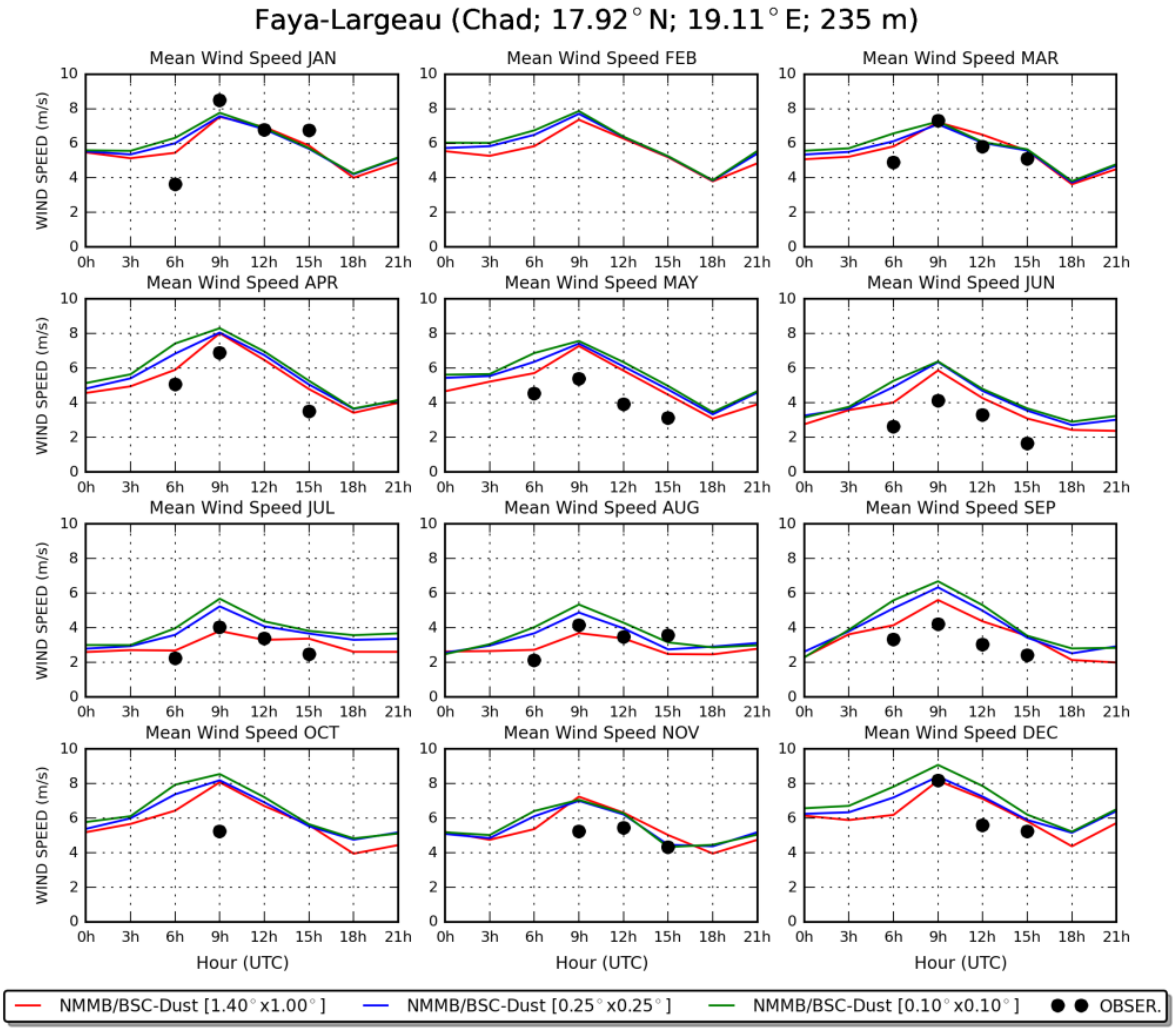

Figure 3.8*: 3-hourly mean wind speed per month provided by GLOB (NMMB/BSC-Dust 1.4ºx1º; red lines), R25 (NMMB/BSC-Dust 0.25ºx0.25º; blue lines) and R10 (NMMB/BSC-Dust 0.10ºx0.10º; green lines) and by surface weather observations (black dots) in Faya-Largeau (Chad; see its location in Figure 3.2). To consider an hourly mean of wind speed observation, hourly observations must provide a high representatively of the specific hour and month of 75%.*

3.4.1.2 Northwestern Africa

Over the grouped AERONET stations in the Northwestern Africa (see Figure 3.2), the model is able to capture most of the DOD variability observed (see Figure 3.5b) throughout the year with a high annual correlation in all the configurations (0.69, 0.71, and 0.70 for GLOB, R25, and R10, respectively). However, under its highest dust activity in August, high DOD underestimations are found. The regional configurations (i.e. R10 and R25) slightly correct this underestimation by intensifying summertime dust emissions on the downwind side of the Atlas Mountains.

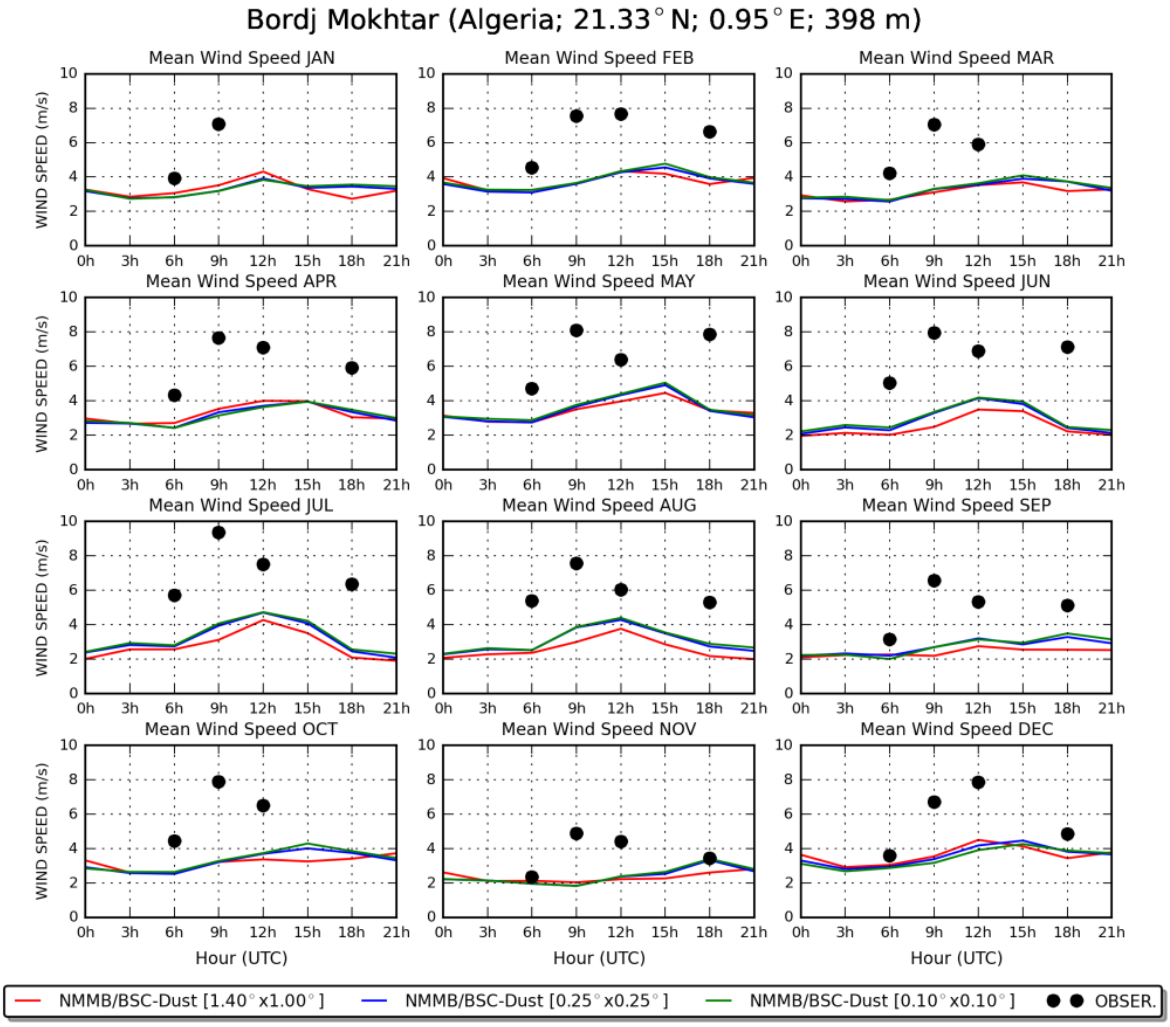

Figure 3.9*: Same as Figure 3.8, but in Bordj Mokhtar (Algeria; see its location in Figure 3.2).*

Even though the emissions over Northwestern Africa increase from GLOB to R10, annual wind speed underestimations are still present in some dust sources from Western Sahara to Southwestern Algeria with values of MB less than -1.5 m/s (blue dots; Figure 3.10) and MAE higher than 2.5 m/s (not shown here). The dust emission growth is mainly as a result of a wind speed increase caused by the enhancement of the morning breakdown of the NLLJ, low-pressure systems between the Atlas and the Hoggar Mountains, such as the summer Saharan Heat Low (SHL), and lee depressions in the South Atlas. In Northwestern Africa, the daily dust emission peak is not as marked as in the Bodélé Depression, and the model simulates it between 9 and 15 UTC (Figure 3.6c) which is not well-captured in comparison with the weather stations over the region, such as in the Bordj Mokhtar site in Algeria. In the Bordj Mokhtar site (Figure 3.9), the daily wind peak is generally observed at 9 UTC and at 18 UTC. This afternoon peak is stronger during the wet season (during summer) and is linked to the presence of cold pool outflows associated with Mesoscale Convective Systems (MCSs), the haboob's meteorological driver. The model configurations do not capture the intensity of these cold pool outflows because they are not parameterized in the model nor explicitly resolved by the proposed

configurations. During summer, dust emissions are partly driven by the breakdown of NLLJ embedded in both the Harmattan and the monsoon flows and by cold pool outflows of MCSs in the downwind side of the Atlas Mountains (Ashpole and Washington, 2013; Marsham et al., 2013). Both mechanisms are not well reproduced by the model and, consequently, this leads to high underestimations in terms of wind speed (Figure 3.10) and DOD (Figure 3.3). The global meteorology and soil initial and boundary conditions (i.e. NCEP/FNLs) used in the model runs (particularly soil moisture, surface pressure, and temperature) may introduce uncertainties in the associated dust processes. Higher soil moisture content can inhibit the modeled dust emission. Otherwise, high surface pressure or low near-surface temperature values can limit the development of the breakdown of the NLLJ.

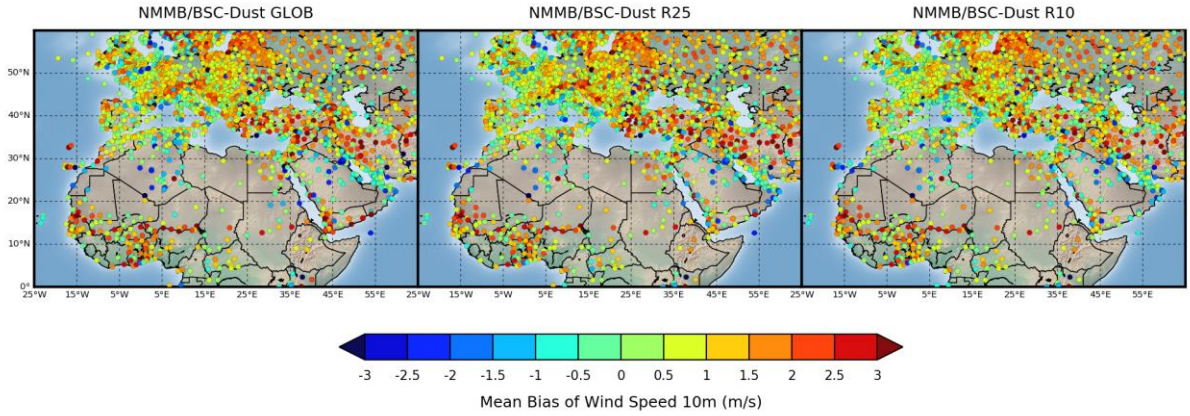

Figure 3.10*: Annual wind speed mean bias of the NMMB/BSC-Dust wind speed at 10 m for 1.4ºx1º (GLOB; left), 0.25ºx0.25º (R25; middle), and 0.10ºx0.10º (R10; right) horizontal resolutions against ISH wind observations*

3.4.1.3 The Middle East

In the Middle East, the highest DOD and dust surface concentrations are found in Syria, Iraq, the Arabian Sea, the Red Sea, around the Iran-Afghanistan-India border and Oman (see Figure 3.3 and Figure 3.4). The Monsoon circulation widely causes emission and transport of dust (Prospero, 2002) from Somalia to the Arabian Sea, Yemen, and Oman by southwest synoptic winds, as well as emission and transport of dust in three north-south wind corridors: (1) from the Red Sea coasts by channeled northwest winds (Kalenderski and Stenchikov, 2016), (2) from Iraq through the Persian Gulf and up to the southern part of the Arabian Peninsula by the northwesterly Shamal winds (Alizadeh-Choobari et al., 2014), (3) and across the Turkmenistan, Iran, and Afghanistan border by northerly winds, commonly known as the “wind of the 120 days” (Alizadeh-Choobari et al., 2014).

The observed DOD annual mean from AERONET sites in the Middle East (i.e. Solar Village in Saudi Arabia and Mezaira in the United Arab Emirates; see Figure 3.2) reaches 0.5 and the highest monthly activity is observed from April to June with DOD of 0.65-0.7, when the strongest months of the

southwest monsoon occur. Due to the proximity of the AERONET stations with the dust sources, strong dust events are monitored which generally vary from 0.5 to 1.5 (see Figure 3.5c). The model reproduces, consistently among configurations, the DOD seasonality observed from satellite data. The DOD tends to present low activity in winter and autumn, but this increases from spring to summer under the Southwest monsoon dynamics. Despite this, the model results show a systematic DOD underestimation throughout the year (Figure 3.3). The computed statistics between model results and the two AERONET stations (see Figure 3.5c) on average are the worst ones of the study domain with annual correlations of 0.37 (GLOB), 0.37 (R25), and 0.34 (R10), and large errors, which on an annual basis computes to MB ~ - 0.30 and RMSE ~0.44 for all configurations.

In the Middle East, the wind and emission peak occurs between 9 and 12 UTC when the emission ratio highly increases from GLOB to R10 (Figure 3.6c). Furthermore, higher wind speeds and emissions are found at GLOB than R25 and R10. This can be explained by the smoother topography in GLOB simulation due to the coarse resolution of the model that allows a stronger penetration of the marine air over land such as in Oman during summer. This fact is shown by a near-coastal source in South Oman (Figure 3.11), which shows really strong Southwestern winds at GLOB and a slightly lower one at R25. R10 reproduces the topography of the region better (Figure 3.1) and wind predictions, especially over complex terrain and near-coastal areas, significantly improve (Figure 3.10 and Figure 3.11). Furthermore, we found high DOD values in the Southern part of the Red Sea (Figure 3.3). Based on Kalenderski & Stenchikov (2016), this region is highly affected by local haboobs and LLJs, developed from the Tokar Delta (Sudan) in summer and transported towards the West coast of the Arabian Peninsula. The R10 increases DOD and surface dust concentration over the Red Sea in comparison with both R25 and GLOB. This is attributed to: (1) an enhancement of the daily wind peak caused by the breakdown of the NLLJ, which produces more emissions from East of Sudan that advects dust eastward, and (2) to the highest topography represented by R10 that in the southern part of the Red Sea (Figure 3.1) creates a blocking effect on dust air masses.

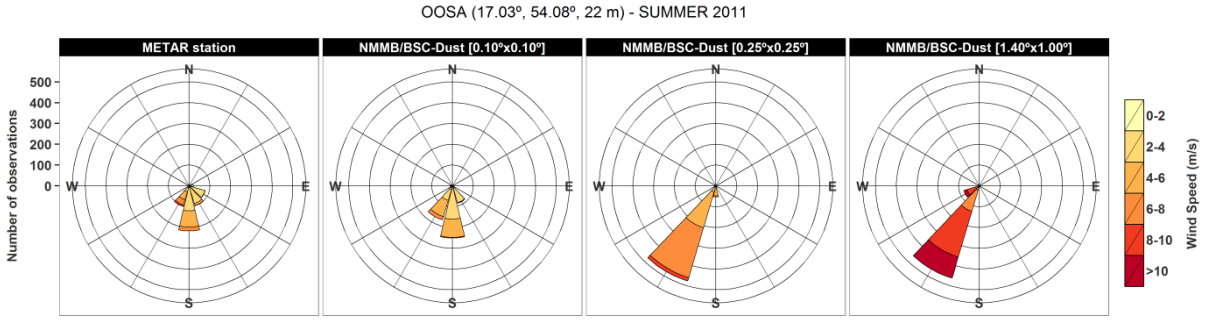

Figure 3.11: *Observed wind rose in OOSA (see its location in Figure 3.2), and the simulated wind rose by the NMMB/BSC-Dust with horizontal resolutions of 0.10ºx0.10º (R10), 0.25ºx0.25º (R25) and 1.4ºx1º (GLOB). Data comparison is performed during summer, covering June, July, and August when the southwestern monsoon develops over the region.*

The observed DOD underestimations in comparison with AERONET in the Middle East can be partly attributed to a poor representation of small-scale emission processes such as the wind peak associated with the breakdown of the NLLJ, the meteorological effects in the vicinities over complex topography, sea breezes (Rezazadeh et al., 2013) and cold pools (Miller et al., 2008). The simulated topographical features (Figure 3.1), which contain steep and high mountains up to 3000 m, and the wind predictions (Figure 3.10) over the region are better reproduced at R10 than R25 and GLOB, respectively. Furthermore, recent changes in source areas (which are not considered in the current desert dust source mask implemented in the model) as a result of the war in Iraq and Syria (Solomos et al. 2017) or other human activities such as agriculture or desiccation in Iran, the border between Iraq and Saudi Arabia, and the plains between the Caspian and Aral Seas (Ginoux et al., 2012; Xi and Sokolik, 2016) could enhance dust erodibility over those regions.

3.4.2 Long-range dust transport regions

3.4.2.1 Eastern Tropical North Atlantic

The eastern subtropical-North Atlantic region is characterized by generally weaker dust intrusions that more frequently and strongly appear during the wet season, which is also well-identified by satellites (see Figure 3.3) and the AERONET measurements (Bambey-ISRA and Dakar in Senegal, and Cape Verde considered in Figure 3.2). The region is characterized by a high annual DOD (see Figure 3.5d) that intensifies during the wet season when West African sources are more active. Higher DOD at R10 than GLOB is found over West Africa, where it significantly increases during summer (the wet season), which highly contributes to more dust transport towards the North Atlantic (see Figure 3.3). Over the Cape Verde island, a much lower DOD is shown in Figure 3.4, due to its larger distance from the Northern African coast (around 600 km), although it remains high in summer when the Saharan dust layer reaches its highest annual altitude (up to 5 km in height) and favors the dust transport to the North Atlantic Ocean towards Cape Verde (Gama et al., 2015) and the Americas (Prospero, 2002).

Based on the grouped AERONET stations (see Figure 3.2), the model generally reproduces the main dust activity, with correlations of 0.66, 0.70, and 0.54 for R10, R25, and GLOB, respectively, although limitations are found on the simulated DOD values that do not reach the magnitude of the observed peaks most of the time,, which lead to compute annual MB of -0.13, -0.17, and -0.16, and annual RMSE of 0.28, 0.26, and 0.27 for GLOB, R25, and R10. In GLOB, a higher amount of dust is presented in the Western and Central Saharan sources from winter to early spring than at regional configurations (R25 and R10). Otherwise, during the wet season, higher DOD values are shown over the region at R10 and R25 than GLOB. This fact is associated with the omission of convective dust storm haboobs (which are frequent in the wet season) of the model. In autumn, especially September and October, the model shows highest annual DOD underestimation in comparison with the

AERONET sites (Figure 3.5). M'Bour (close to Dakar AERONET site and with a mean observed PM10 of 136 µg/m^3, see Figure 3.7c) is the station where the higher PM10 underestimation occurs at the three experiments (with MB of -13, -49, and -41 µg/m3 for GLOB, R25, and R10, respectively) and lower correlations (0.55, 0.5, and 0.44 for GLOB, R25, and R10, respectively).

During autumn is when dust transport towards Senegal and Cape Verde is dominated by the Mali-Mauritania sources (Gama et al. 2015). Dust sources in the Mali/Mauritania border are omitted by including the topographical approach, as it was already identified in Pérez et al. (2011). This leads to the underestimation of the dust fields observed by satellite data (Figure 3.3) and to a lack of emissions in Figure 3.6a. The better scores at GLOB than at both regional configurations are probably linked to its higher contribution to westerly dust transport from the Central Sahara during winter and spring over the region (Figure 3.3 and Figure 3.4), which compensates the lack of short dust transport from Mauritania and Mali. Additionally, observed underestimations in PM10 at M'Bour site could also be linked to the presence of non-dust mass monitored by the station, which is affected by non-dust particles (see Section 3.3.3) that the dust model does not consider.

3.4.2.2 Eastern sub-Tropical North Atlantic

In the eastern subtropical-North Atlantic (i.e. Tenerife Island in the Canary Islands, see Figure 3.3e), two maximum DOD activity periods are observed: winter (with low-level dust intrusions) and summer (with high-level dust intrusions). The model is in very good agreement with the daily variability of the AERONET with annual correlations of 0.76, 0.75, and 0.71 for R10, R25, and GLOB, respectively, and the computed annual MB of -0.05 and RMSE of 0.11 for all configurations.

Lower annual correlations in GLOB in comparison with regional configuration (R10 and R25) are linked to the fact that the three AERONET sites are in the same model pixel, omitting the different altitude of each of them. Also, GLOB provides a persistent background DOD (0.05-0.1) that is mainly produced by a lower representation of the topography of the North Atlantic African coast. This fact significantly reduces orographic obstacles and favors the dust propagation from West Africa to the Canary Islands.

The performance of the model presents different behaviors, depending on the AERONET site. Although the three AERONET sites are situated very close to each other (Santa Cruz de Tenerife is located at 52 m a.s.l within the oceanic boundary layer, La Laguna is located at 568 m a.s.l., and Izaña is located at 2.391 m a.s.l., normally under free troposphere conditions), they present very different behaviors that are linked to the seasonal vertical transport over Tenerife Island. The model is particularly good at capturing the high-level summer events as it is indicated by the good performance of the model at Izaña (with correlations of 0.82, 0.84, and 0.80 for R10, R25, and GLOB, respectively, MB of 0.01 and RMSE of 0.06 for all configurations), which is considered the AERONET site with

the highest correlation of NAMEE. On the other hand, the model performances in the rest of the stations are also good: La Laguna with correlations of 0.81, 0.82, and 0.78 for R10, R25, and GLOB, respectively, MB of -0.1 for all configurations, and RMSE of 0.13 for GLOB and 0.12 for both R25 and R10; and Santa Cruz de Tenerife with correlations of 0.75, 0.79, and 0.79 for R10, R25, and GLOB, respectively, MB of -0.1 for all configurations, and RMSE of 0.15 for GLOB and 0.16 for both R25 and R10.

3.4.2.3 Mediterranean

The Mediterranean basin is affected by episodic dust intrusions in the Western and Central basin from Morocco, Algeria, Tunisia and Libya; meanwhile, in the Eastern Mediterranean, sources from the Northeastern Sahara, such as Egypt and the Western part of the Middle East, mostly contribute to its dust budget. As shown in the AERONET comparison (Figure 3.5), dust activity in the Western Mediterranean is frequent during spring (maximum in April) and summer (maximum in August). In the Central Mediterranean, it is higher during spring (maximum in April) although Lampedusa island (closer to the Tunisian and Libyan coast) is more affected by strong events in April and to the second degree in July. In the Eastern Mediterranean, the monthly dust activity is high from January to June and lower and shorter in some periods such as late July, October, and December.

The model can capture dust intrusions over the whole Mediterranean basin although, in comparison with satellite images and AERONET sites, the DOD magnitude of most dust events is underestimated (Figure 3.3). From the AERONET comparison, correlations increase from the Eastern, Central to the Western Mediterranean basin, although this model performance also varies depending on the configuration (R10, R25 and GLOB): the Eastern Mediterranean (0.55, 0.56 and 0.56), the Central Mediterranean (0.65, 0.67 and 0.56), and the Western Mediterranean (0.69, 0.69 and 0.64). In terms of annual RMSE, the model performance also increases from the Eastern, Central to the Western Mediterranean basin: the Eastern Mediterranean (0.12 for all configurations), the Central Mediterranean (0.1 for GLOB and 0.09 for both R25 and R10), and the Western Mediterranean (0.07 for all configurations). On the other hand, annual MB shows an overestimation of 0.01 for GLOB, and an underestimation of -0.01 for both R25 and R10, for the three regions.

Different behaviors, depending on the sub-region and configuration, can be associated with a wide range of causes. The lower model performance in the Eastern Mediterranean for all configurations is mainly due to high influence of sources from the Western part of the Middle East that the model systematically underestimates, as it has previously shown in Section 3.4.1.3. Mainly during spring and summer, a background DOD (0.05-0.1) constantly appears at GLOB in comparison with R10 and R25, which is well identified by seasonal DOD means (Figure 3.3) and in the DOD time series (Figure 3.5), which consequently reduces the GLOB performance in the whole region. This is properly corrected

with the R25 and R10 regional configurations. Mountains (such as the Atlas) play a key role in blocking dust blowing from Northwestern Africa towards the North Atlantic and the Mediterranean, whereas the Sierra Nevada ranges in Southern Spain reduce Northern African dust intrusions into the inner Iberian Peninsula. The simulated mountain height is lower than real at GLOB (Figure 3.1). Thus, airborne particles find a few orographic obstacles in their path than real, which favors the dust transport at low altitudes. Otherwise, wet deposition processes over the Mediterranean significantly increase at higher resolutions (not shown), which removes atmospheric dust mainly when maximum rainfall and cloud cover occur in the Western and the highly Central Mediterranean basin during spring and decrease in the Eastern Mediterranean from winter to spring. On an annual basis, the accumulated dust deposition at least doubles over many regions from GLOB to R10, leading to the removal at regional configurations (i.e. R25 and R10) of the DOD background (0.05-0.1) that is persistent at GLOB.

3.5 Summary and conclusions

The present work analyzes the spatiotemporal scales (from synoptic to mesoscale) associated with the dust cycle focusing on dust sources over Northern Africa and the Middle East using a multiscale model, the NMMB/BSC-Dust model. Three simulations of the NMMB/BSC-Dust model are performed for an annual cycle (2011) over NAMEE region covering global to regional scales: 1.4ºx1º (GLOB), 0.25ºx0.25º (R25), and to 0.10ºx0.10º (R10) horizontal resolutions. Observations from AERONET sites, surface weather stations, and in-situ AMMA PM10 network, as well as satellite aerosol products (MODIS and MISR), are compared with the model results.

Modeled dust emissions over desert dust sources increase at higher spatial resolutions mainly due to an increase of the wind speed peak that is associated with the enhancement of the morning breakdown of the NLLJ, low-pressure systems, and the wind channeling effect over some sources (such as the Bodélé Depression in Chad). Dust emission increase between configurations is higher from GLOB to R25 (R25 can reproduce smaller-scales that are not resolved by GLOB) than from R25 to R10 because both regional configurations are resolving processes at similar scales. Despite this, higher emissions are found at GLOB than at R25 and R10 in some coastal sources, such as in Western Sahara, Libya, Somalia and Oman, because GLOB represents lower topographies and large-scale synoptic sea winds can strongly penetrate inland. Otherwise, haboobs, which are characterized by short-life and intense peaks of DOD and PM10 mainly presented during the wet season over the Sahara-Sahel and the Middle East, are not resolved by the model at the proposed configurations because the dust emissions associated with cold pools are not parameterized nor explicitly simulated.

The model reproduces the seasonality of the dust activity observed by the satellites, which is controlled by the latitudinal change of the ITCZ and monsoon systems and remains consistent from global (GLOB) to regional (R25 and R10) configurations. In the DOD quantitative comparison with

AERONET observations, the model shows higher annual correlations in dust transport regions ($r > 0.7$) than near-dust source regions as in the Sahara-Sahel ($r \sim 0.6$) and in the Middle East ($r < 0.4$). In the Sahara-Sahel, the model overestimates DOD in spring and PM10 from October to March. One of the reasons for this is linked to a wind speed overestimation of the Harmattan winds in the Bodélé Depression, which may be partly explained by the initial meteorological conditions. In Northwestern Africa, the model underestimates DOD and PM10. These underestimations are partly associated with underestimation of dust emissions over Mali-Mauritania border, annual wind speed underestimations between Western Sahara and South Algeria (MB ~ -2 m/s) as well as a combination of high soil moisture content and lower temperatures that limit the modeled dust emission mechanisms. In the Middle East, the model underestimates DOD partly linked to topographical features and meteorological small-scale processes that are not well resolved in the proposed configurations. Despite this, meteorological impacts are better reproduced at R10 than R25 and GLOB, respectively. At long-range dust transport regions, GLOB shows a background DOD (0.05-0.1) over some regions such as in the Mediterranean basin and Europe during spring and summer when dust intrusions are more frequent. This is mainly caused by a lower representation of the topography and weaker wet convection processes at GLOB than at R25 and R10, respectively, which favors dust transport from Northern Africa.

This work contributes to a better understanding of the benefits and uncertainties of using a multi-scale model from sub-synoptic to mesoscale resolutions. These results show a consistency of the model for a range of spatiotemporal scales to reproduce the dust cycle over Northern Africa, the Middle East and Europe.

Chapter 4

4 Topographic effects on synoptic dust storms over complex terrains

4.1 Background

The Middle East has been identified in Chapter 3 as a region where the model tends to present larger limitations reproducing dust concentration fields (e.g. DOD). There are several causes of this: (1) the representation of its dust sources in the model, (2) the presence of smaller scale dust storms (such as haboobs), and (3) the topographic effects on dust fields caused by a really complex topography over the region, which alters the meteorology of the dust cycle processes such as dust propagation in many ways. The present chapter focuses on the analysis of the topographic effects and their impacts on dust transport in the vicinity of complex terrains. For this purpose, two simulations were performed: one with a very high horizontal resolution (at 0.03ºx0.03º) and another one with a lower horizontal resolution (at 0.33ºx0.33º). Both configurations covered two intense dust storms that occurred on 17-20 March 2012 as a consequence of strong winds that spanned over thousands of kilometers in the Middle East. The chapter is organized as follows: Section 4.2 presents the study region. Section 4.3 presents the model setup used in the experiments. Sections 4.4 and 4.5 include a description of the ground-based, satellite observations and meteorological reanalysis data and methods used for the model evaluation. In Section 4.6, the model outputs are compared with observational datasets and reanalysis, and the results are discussed. Finally, Section 4.7 summarizes the findings of the present study.

4.2 Description of the Middle East domain

The Middle East is a singular region characterized by a complex topography and with several peaks higher than 3000 m; a low average annual precipitation; low soil moisture content; small and large dust sources with erodible sediments of fine particles from areas with dry lakebeds, dry riverbeds and sand seas; and a wide variety of meteorological phenomena (e.g. Shamal winds, thermal sea breezes, convective thunderstorms or low-level jets) that are able to produce severe dust storms (Miller et al. 2008; Rezazadeh et al. 2013). Its three primary desert regions are the Rub Al-Khali (“Empty Quarter”) in the southeast, An Nafud in the northwest, and the Ad Dahna sand corridor in the east, connecting the two previous deserts. Remote desert regions that can potentially serve as dust source regions to Saudi Arabia include the vast Sahara Desert to the West and the Syrian and Iraqi Deserts to the north (Prospero et al. 2002; Goudie & Middleton 2006; Ginoux et al. 2012). The seasonal variation of the dust activity in the Middle East is complex and differs depending on the region. In most parts of the Middle East, dust activity is frequent throughout the year, with minimum activity in the winter months. Dust activity increases in March and April, with maximum activity in June and July, and weakens in September (Shao, 2008).

The Middle East contains large areas of mountainous terrain (Figure 4.1). The Zagros Mountains are located in Iran and in areas along its border with Iraq. The Central Plateau of Iran is divided into two drainage basins: the northern basin is Dasht-e-Kavir (Great Salt Desert), and the Southern basin is Dasht-e-Lut. In Yemen, elevations exceed 3000 m in many peaks, and highland areas extend north along the Red Sea coast and north into Lebanon. A fault-zone also exists along the Red Sea, with a continental rifting creating a trough-like topography with areas located well-below sea level. The Al-Hajar mountain range is located in the East of the United Arab Emirates (UAE) and along the north coast of Oman; it reaches up to 3000 m elevation with its highest mountains in its central section, Jebel-al-Akhdar.

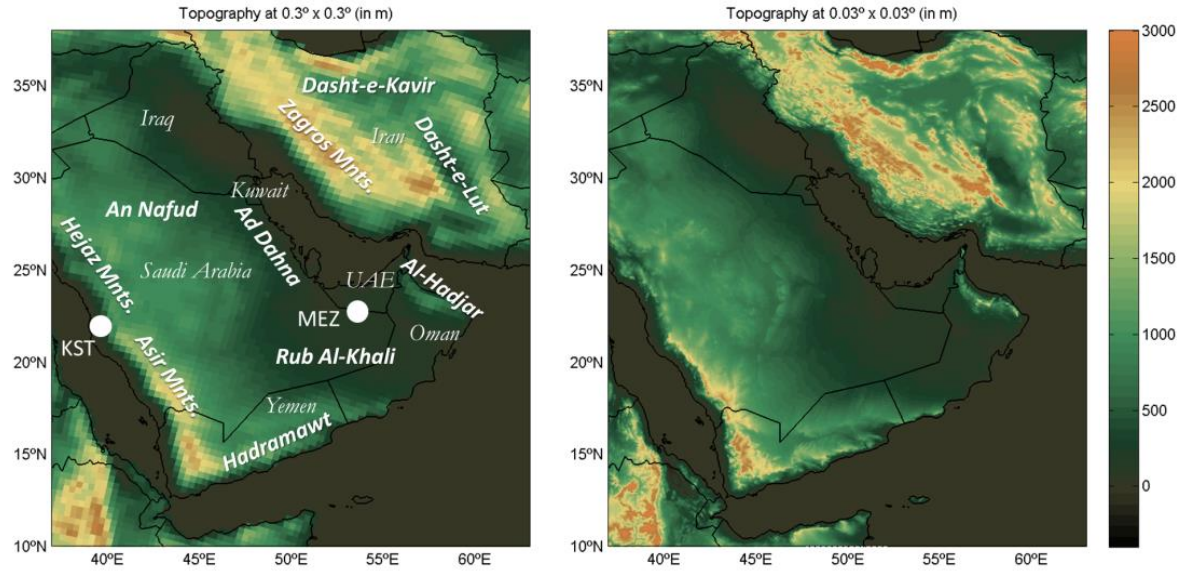

Figure 4.1: *Topography at horizontal resolutions of 0.33º (LR) and 0.03º (HR) over the study region in the color scale. The main countries referred to in the text (i.e. Oman, Yemen, Saudi Arabia, Kuwait, Iran, Iraq and the UAE), primary desert dust regions (i.e. Rub Al-Khali, Ad Dahna and An Nafud in the Arabian Peninsula; and Dasht-e-Kavir and Dasht-e-Lut in Iran), main mountains referred to in the text (Hadramawt, Asir, Hejaz, Al-Hajar and the Zagros Mountains), and the Kaust Campus (KST) and Mezaira (MEZ) AERONET sites used in the study are indicated in the map.*

4.3 Model setup

Two regional NMMB/BSC-Dust simulations are performed covering the whole Arabian Peninsula: a regional simulation for Northern Africa, the Middle East and Europe (box window: 0º – 70ºN and 31ºW – 71ºE) with a horizontal resolution of 0.33ºx0.33º (~36 km in the Equator; hereafter referred to as LR) and a high-resolution simulation covering the Arabian Peninsula (box window: 10ºN – 40ºN and 35ºE – 65ºE) with a horizontal resolution of 0.03ºx0.03º (~3 km in the Equator; hereafter referred to as HR). The vertical resolution for both simulations is 40 σ-hybrid layers with the top of the

atmosphere at 50 hPa. The atmospheric model's fundamental time steps for both LR and HR experiments are set to 40 and 25s, respectively.

The simulation period is from 10 to 21 March 2012, and consists of 24-hourly forecasts (initialized at 0 UTC) with model outputs saved every 3 hours. The study domain of this experiment covers from 35ºE to 65ºE in longitude and from 10ºN to 40ºN in latitude. The initial meteorological state is supplied by the NCEP/Final Analyses (FNL; at 1º×1º horizontal resolution) at 0 UTC, and boundary conditions are updated every 6 hours. The model does not include dust data assimilation systems, and therefore dust concentration at 0 UTC is defined by the value at hour 24 of the previous day's dust forecast, except on 10 March at 0 UTC when dust concentration is set to zero (cold start). The study period covers from 17 to 21 March 2012; the previous six days are discarded in this study and are only used as a warm-up of the simulation. Simulations are run with the operational RRTM radiation scheme, which allows for dynamic dust-radiation feedback. Both configurations use a tuning factor of 0.255 in the model's emission scheme. The main model features are summarized in Table 4.1.

Table 4.1: *Summary of the main features of the model configurations used in the present chapter: horizontal resolution, horizontal grid points, domain (latitude and longitude ranges), and fundamental time step.*

Configuration	Low-resolution (LR)	High-resolution (HR)
Horizontal resolution	0.33ºx0.33º	0.03ºx0.03º
Horizontal grid points	307x211	1001x1001
Domain (Lat & Lon ranges)	NAMEE* (0º-70ºN and 31ºW-71ºE)	The Middle East (10ºN-40ºN and 35ºE-65ºE)
Fundamental time step (s)	40	5

*NAMEE is Northern Africa, the Middle East and Europe

4.4 Observational datasets

There are few available in-situ observations such as AERONET stations and a low amount of international research campaigns that have been conducted in the Middle East in comparison with other desert dust source regions such as the Sahara (Cuevas, 2013). To complement the model results, satellites and ground-based meteorological observations are included in the present analysis.

4.4.1 Satellite aerosol products

4.4.1.1 MSG/SEVIRI RGB dust product

The Meteosat Second Generation (MSG) satellite is a joint project between the European Space Agency (ESA) and the European Organisation for the Exploitation of Meteorological Satellites

(EUMETSAT). The MSG satellite's radiometer, the Spinning Enhanced Visible and Infrared Imager (SEVIRI) with 12 spectral bands, provides unique capabilities for monitoring rapidly evolving events such as thunderstorms and dust storms due to its frequent sampling (every 15-min). The MSG satellite is in geostationary orbit over the Equator and its full disc view covers Europe, Africa and the Middle East with a horizontal resolution of 1-3 km in the High-Resolution Visible (HRV) channel.

In the present analysis, the MSG/SEVIRI RGB dust product is used with a 3 km horizontal resolution, which is similar to the horizontal resolution of the HR simulation (0.03ºx0.03º horizontal resolution). The MSG/SEVIRI RGB dust product is a qualitative and dimensionless column-load product based on an RGB composite based upon infrared channels of SEVIRI (8.7, 10.8, and 12 μm), in which red is the difference between 12 and 10.8 μm, green is the difference between 10.8 and 8.7 μm, and blue is 10.8 μm. The RGB combination is designed for detecting and monitoring dust storms during both day and night time (Schmetz et al., 2002), and it exploits the difference in emissivity of dust and desert surfaces, although it does, however, allow for the further (24-hour) tracking of dust clouds as they spread over the sea. Also, during the daytime, it exploits the temperature difference between the hot desert surface and the cooler dust cloud. In this RGB combination, the dust appears pink or magenta. Dryland looks from pale blue (daytime) to pale green (night time). Thick, high-level clouds have red-brown tones, and thin high-level clouds appear very dark (nearly black). Emissions and subsequent transport of individual dust events can be very well observed and followed in the RGB composite pictures.

4.4.1.2 Aqua/MODIS AOD

The Moderate Resolution Imaging Spectroradiometer (MODIS) is onboard the Aqua and Terra satellites and provides high radiometric sensitivity in 36 spectral bands ranging in wavelength from 0.4 to 14.4 μm. Two bands are imaged at a nominal resolution of 0.25 km at nadir, with five bands at 0.5 km, and the remaining 29 bands at 1 km. A ±55º scanning pattern of the satellite orbit at 705 km altitude achieves a 2330 km swath and provides global coverage every one to two days. The MODIS aerosol algorithm consists of two independent algorithms, one for deriving aerosols over land and the second for aerosols over the ocean (Remer et al. 2002; Levy et al. 2010). However, the algorithm over land was developed only for low ground reflectance (i.e. over dark vegetation). For this reason, we also include the MODIS Deep Blue (DB) product which provides information over arid and semi-arid areas. The MODIS DB product employs radiances from blue channels for which the surface reflectance is low enough for the presence of dust to brighten the total reflectance and enhance the spectral contrast (Hsu et al., 2004). The Level 2 (at 10 km from the Collection 6) AOD data (cloud-free) and the AOD DB products from Aqua/MODIS sensor (Levy et al., 2015) are used in the following analysis.

4.4.2 Ground-based observations

4.4.2.1 Surface weather observations

Ground-based observations are sparse close to dust source regions and available time series are relatively short and present many gaps. In the present study, surface weather observations from the Integrated Surface Hourly (ISH) database (see Section 3.3.1) are used to quantitatively evaluated against modeled wind speed at 10 m and observed horizontal visibility is used as proxy information of the evolution of the dust event at surface level.

4.4.2.2 AERONET sun-photometers

Column-integrated aerosol optical properties routinely observed within AERONET sun-photometers (Holben et al. 1998; Smirnov et al. 2000; see Section 3.3.2) are used in the model comparison. In the Middle East, a few number of AERONET stations are available, and most of them are found in the Arabian Peninsula (i.e. Bahrain, Kaust Campus, Kuwait University, Mezaira or Solar Village). In the present analysis, direct-sun Level 2.0 data (cloud screened and quality-assured) such as AOD and AE are used. The selected AERONET stations are Mezaira (MEZ) in the UAE and Kaust Campus (KST) in Saudi Arabia (Figure 4.1) because they were the only available ones during the study period. The AE is added as proxy information of the presence of coarse mineral dust in the observation point (AE < 0.75). Because AERONET data is acquired at 15-min intervals on average, the AERONET measurements within ±90 min around the 3-hourly model outputs are averaged and are used for the model comparison.

4.5 Meteorological reanalysis data

Data from the ERA-Interim reanalysis (Dee et al., 2011) downloaded from the ECMWF website (http://apps.ecmwf.int/datasets/data/interim_full_daily/) is used to compare meteorological fields and spatial patterns. It is the latest global atmospheric reanalysis produced by the European Centre for Medium-Range Weather Forecast (ECMWF) as a transition between ERA-40 and a future reanalysis project. It provides information on a large variety of surface parameters (3-hourly), describing the weather as well as ocean-wave and land-surface conditions and 6 hourly upper-air parameters (37 pressure levels up to 1 hPa), on a 0.25ºx0.25º grid. ERA-Interim uses an improved atmospheric model and a more sophisticated data assimilation method (4-D-Var) for atmospheric analysis compared with ERA-40. In the present analysis, 10 m wind fields and the geopotential height at 700 hPa are used.

4.6 Results and discussion

4.6.1 Case study of two synoptic dust storm outbreaks

Two large-scale dust storms that occurred in the Middle East between 17 and 21 March 2012 extended through thousands of kilometers of land and sea, affecting all of the countries in the region and from the Arabian Sea to the Red Sea. Both dust storms were driven by the passage of a large mid-tropospheric trough of low pressure moving eastward from the Eastern Mediterranean basin on 17 March to Eastern Iran on 20 March. Jish Prakash et al. (2015) identified this whole event as one of the most powerful dust storms found in the literature.

On 17 March 2012, a dust storm originated in the Tigris and Euphrates river basin, mainly in Eastern Syria and Iraq, as a result of strong northwesterly Shamal winds that extended from Iraq towards the Arabian Gulf and from the ground up to 700 hPa. These dust-generating winds were associated with the advancing of a cold front (Al-Yahyai and Charabi, 2014). The rapid dust uplifting between 8 and 12 UTC generated a thick dust cloud that covered Iraq and Kuwait, dropping visibility below 300 m in many surface weather stations, as shown in Figure 4.2. The dust storm moved from Iraq and Kuwait to the southern and western Arabian Peninsula, firstly extending over the Persian Gulf and progressively affecting countries such as Saudi Arabia, Iran, Bahrain, Qatar, the UAE, and Oman. Satellite images (Figure 4.2) show how the dust plume posteriorly extended towards the inner Rub'al Khali desert and reached the Asir Mountains in the western Arabian Peninsula, and the mountains in Yemen and western Oman where it was blocked at 12-15 UTC 18 March. Between 18 and 19 March 2012, under the passage of the dust front, satellite aerosol images achieved AOD values of up to 5 and surface weather stations monitored horizontal visibility lower than 800 m (Figure 4.2). Also, during the following hours, satellite images observed dust channeling through valleys between the near-coast mountain ranges: (1) in Western Saudi Arabia towards the Red Sea, (2) in Southern Yemen towards the Red Sea and the Gulf of Aden, and (3) in Southwestern Oman also towards the Arabian Sea.

On 18 March 2012, while the first dust storm was still crossing the Arabian Peninsula, a second dust storm formed over the Eastern Iranian deserts and the Sistan and Baluchistan basin, which covers the borders where Afghanistan, Pakistan, and Iran meet (Al-Yahyai and Charabi, 2014). This massive dust storm was also driven by a mid-tropospheric trough of low pressure (that previously crossed over Iraq) that intensified the northerly winds over the region. The northerly winds become accelerated by the channeling effect of the surrounding orography resulting in substantial dust emission and long-range dust transport. The new-formed dust storm moved south over the complex terrain towards the Arabian Sea, the Oman Gulf and reached the Oman sea coasts on 19 March at 12 UTC (Figure 4.2). The role of the topography on the dust propagation was also important in this event because the blowing dust was channeling through valleys between mountain ranges in Iran and Pakistan in the direction of the sea,

as shown in Figure 4.2. Furthermore, the dust cloud was blocked at low altitudes by the Al-Hajar mountain range in Oman and was forced to extend to the west of the Strait of Hormuz and circle the mountains eastward and towards the Arabian Sea. Based on some stations, visibility was reduced to less than 500 m in Northern Oman and Southern Iran (Figure 4.2). Aqua/MODIS shows on 19 March how the AOD values were high (between 2 and 3) on the Omani coast due to the initial dust blocking. On 20 March, AOD retrievals reached up to 4 on both the left and right sides of the Al-Hajar Mountains and reached a relative maximum AOD (between 2 and 3) on the Omani coast because the blocked dust was still present. Finally, the intense dust storm spanned thousands of kilometers over the Arabian Sea, reaching the Yemeni and Somalian coasts over the following days.

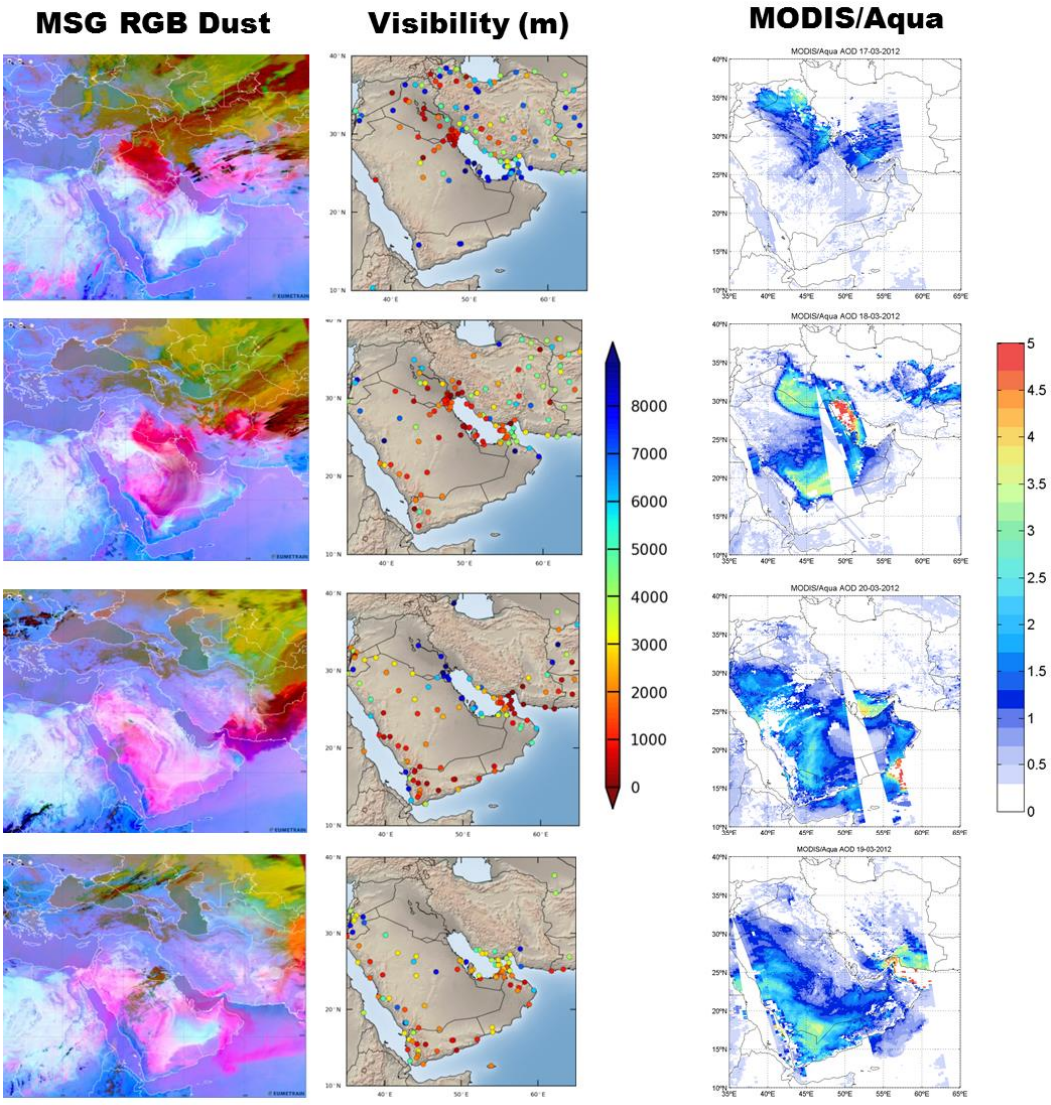

Figure 4.2: *Observed dust concentrations from 17 to 20 March 2012 at 12 UTC (in rows). First column: MSG/SEVIRI RGB dust product; second column: horizontal visibility (in meter) from surface weather stations; third column: aerosol optical depth (AOD) at 550 nm from Aqua/MODIS. These images correspond to the combined Level 2 (at 10 km x 10 km) aerosol product from Aqua/MODIS between 9 and 12 UTC.*

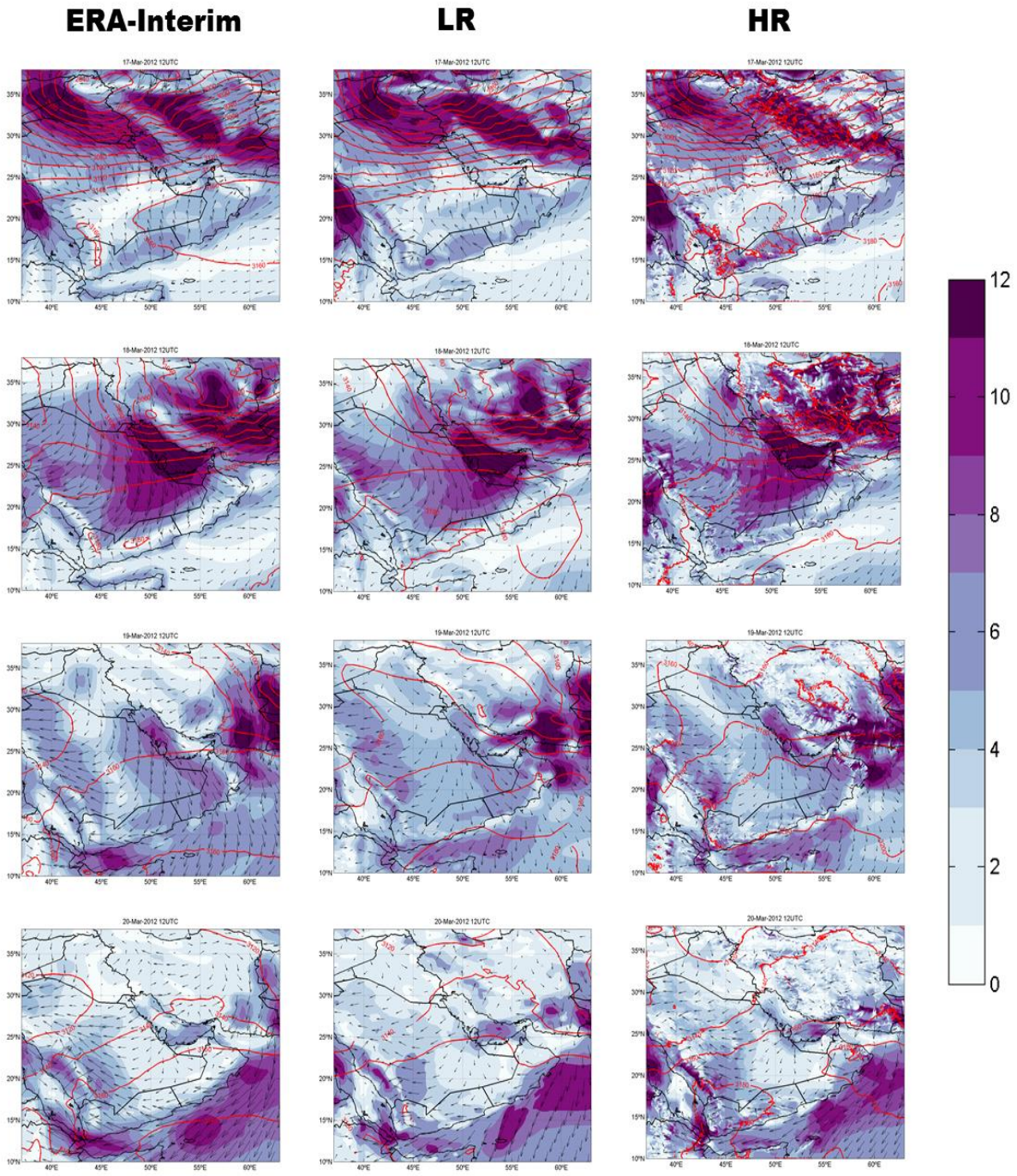

Figure 4.3. *Modeled geopotential height (red color solid line) at 700 hPa and winds at 10 m (wind speed is shown by shaded areas up to 12 m/s in one color bar and wind direction by black arrows) from 17 to 20 March 2012 at 12 UTC (in rows) for ERA-Interim reanalysis at 0.25º x 0.25º (right panels), and for the NMMB/BSC-Dust model with horizontal resolutions of 0.33º (LR; central panels) and 0.03º (HR; left panels).*

4.6.2 Model evaluation

In the present section, modeled dust and wind fields are compared against observational data previously introduced. The modeled topography domains for both configurations (LR and HR)

represent topography differently. Simulated topography at 0.03º x0.03º horizontal resolution represents mountain ranges, valleys, coastlines and small islands better than at lower horizontal resolution (0.3º x 0.3º) with height differences of up to 1 km, although these height differences are even higher in steep and narrow mountain ranges in Oman, Iran, Yemen, and Saudi Arabia (Figure 4.1).

Simulated meteorological (Figure 4.3) and airborne dust distributions (Figure 4.4) can reproduce the main features observed at ground level (i.e. visibility and winds) and column-load dust aerosol satellite retrievals (Figure 4.2). Both simulations (LR and HR) reproduce the northwesterly winds which are extended up to 700 hPa level due to a high-pressure system over the Arabian Peninsula, as it is also observed in the ERA-Interim fields (Figure 4.3). The intensified northwesterly wind caused an increase of the surface winds from the Iraq Desert to the Persian Gulf where wind speed reached up to 12 m/s on 19 March (Figure 4.3). Also, they follow the reduction of the visibility observed by the ground-based observations and the increasing of observed column-load aerosol fields by the satellites (Figure 4.2). However, inconsistency between concentration-modeled fields and observations could be detected in some areas. High satellite AOD (up to 5) and low surface visibility are observed over the Persian Gulf on 18 March (Figure 4.2). These high aerosol concentrations do not have correspondence with modeled dust fields (see dust optical depth < 1 in Figure 4.4). Even though visibility observations are dust-dominated phenomena, aerosol concentrations in this region are also influenced by local high humidity contents in near-coastal areas and aerosols from anthropogenic activities in the region (Basart et al., 2009), inducing the observed model underestimation.

On 17 March, both model simulations show how dust rises from the Iraq Desert and moves in a southeasterly direction affecting the entire Arabian Peninsula and reaching Oman and Yemen on the following days (Figure 4.4). However, the model underestimates the dust concentrations during 18 March over Iraq and Kuwait and overestimates the dust concentrations (AOD > 5) during its transport in the middle of the Arabian Peninsula in the following days, as shown in the satellite comparison in Figure 3.3. This is also confirmed by the Mezaira AERONET comparison (see 18 March in Figure 4.5). On 17 March, both simulations present wind overestimations over the main dust sources in Iraq and wind underestimations in Kuwait in comparison with surface weather stations at 12 UTC (MB up to -8 m/s; Figure 4.6), when the emission of the first event is produced. During the following hours, dust transports south (see Figure 4.4) and during its southeasterly trajectory is affected by a high wind speed underestimation in both simulations (up to 8 m/s; see Figure 4.6). As a consequence of that, both simulations show low AOD values (Figure 4.4) over Iraq and Kuwait on 18th March in comparison with Aqua/MODIS AOD, and furthermore, both present a delay in the arrival of the dust front to the Southern Arabian Peninsula of about 8 hours (see Figure 4.4 on March 18th at 12 UTC). This delay is linked to the NCEP/FNL meteorological fields that are used as initial and boundary conditions in the simulations, which is also observed with the surface winds against ERA-Interim (Figure 4.3).

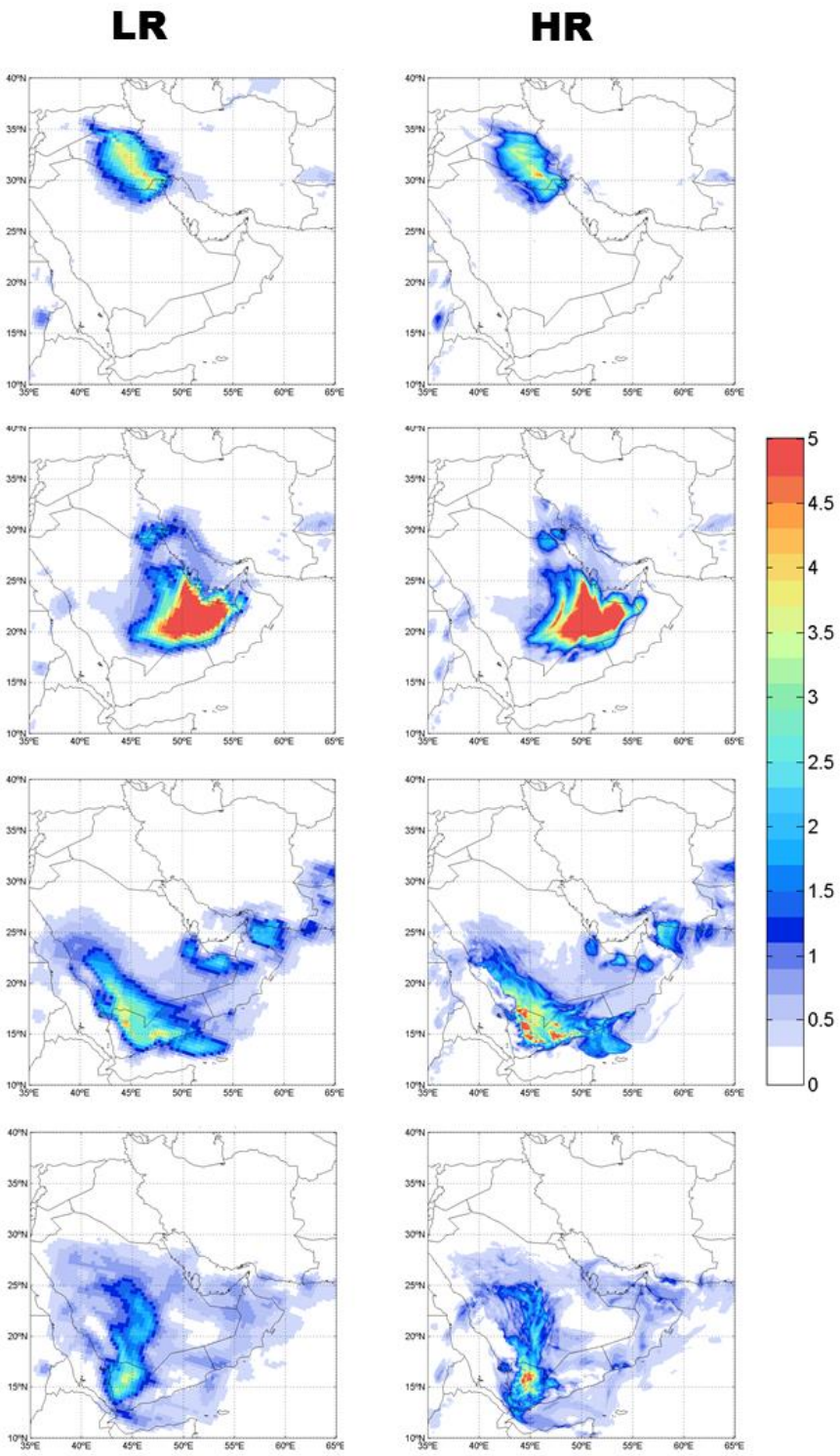

Figure 4.4: *Modeled dust optical depth (DOD) at 550 nm from 17 to 20 March at 12 UTC (in rows) for the NMMB/BSC-Dust model with horizontal resolutions of 0.33º (LR; left panels) and 0.03º (HR; right panels).*

When the dust plume arrives at Qatar and the UAE on 18 March, a large area between the coast and the Rub Al-Khali desert quickly activates, reaching simulated AOD larger than 5 (Figure 4.4), which overestimates the satellite aerosol retrievals Figure 4.2. The Mezaira AERONET station (in the Southern UAE; see 18 March in Figure 4.5) also reported this AOD overestimation, which is mainly

driven by the high dust emission from the UAE coast. At that time, ERA-Interim (Figure 4.3) reproduces strong northerly winds (>12 m/s) across the Persian Gulf that hit the UAE coast, which were overestimated as reported some surface weather stations (above 4 m/s, see Figure 4.6), although with higher values in the LR simulation, which is also associated with a high AOD peak than HR simulation in the Mezaira AERONET site (Figure 4.5a).

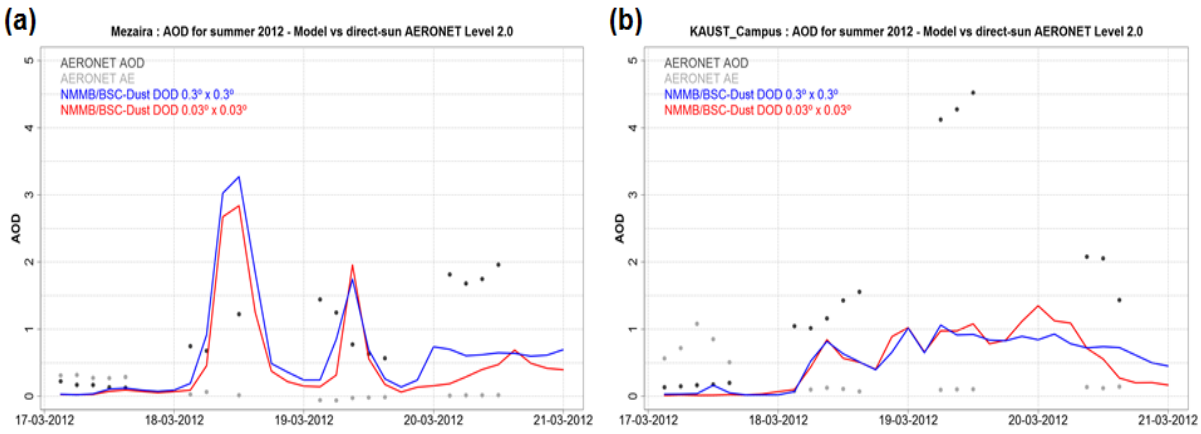

Figure 4.5: *Modeled and observed aerosol optical depth 550 nm (AOD) at a 3-hourly temporal resolution for (a) Mezaira (MEZ) and (b) Kaust Campus (KST) AERONET sites. The Ångström's exponent between 440 and 870 nm (AE) is added as proxy information of the presence of coarse mineral dust in the observation point (AE < 0.75). The location of both sites is shown in Figure 4.1.*

On 19 March, we can observe a sharp increase in the modeled AOD that is not observed by the Mezaira AERONET sun-photometer (see the second AOD peak in Figure 4.5a). This high dust emission from Rub Al Khali is associated with a wind increase over the region probably associated with high and slightly overestimated northerly winds, which is reported by the coastal station in the UAE between 6 and 9 UTC 19 March (not shown here), favoring dust emission in this area. These local emissions are associated with coarse fractions that rapidly deposited back on the ground. On 20 March, when the dust front with origin in Iran arrives at the Omani coast (Figure 4.2), LR presents the dust arrival to the Mezaira AERONET station 12 hours earlier than HR (Figure 4.5a). This is associated with a lower topography and fewer obstacles for the wind flows in the LR simulation that provoked a wind speed overestimation along its trajectory towards the UAE. On the contrary, the blowing of dust by winds in the HR simulation had to overcome and circle higher topographic obstacles, delaying its advance, as it is observed in Aqua/MODIS and MSG/SEVIRI RGB dust products on 19 and 20 March (Figure 4.2).

On the other hand, the AERONET comparison in Kaust Campus AERONET site shows how the maximum dust concentration is found on 19 March. Both model simulations (LR and HR) underestimate the observed AOD (Figure 4.5). The Kaust Campus AERONET sun-photometer is

located in a rural region just at the seashore in Thuwal (Saudi Arabia, see the KST label in Figure 4.1). Both model simulations (LR and HR) reproduce the observed dust presence; however, they underestimate the observed values that achieve values up to 4.5 as shown in the Kaust Campus AERONET site (Figure 4.5b). Both simulations (LR and HR) show that dust emission originated in a littoral area of the Red Sea (Figure 4.7) where the surface winds achieve values > 12 m/s on 18 March at 12 UTC (Figure 4.3). Additionally, as a result of the dust blocking over Asir Mountains, dust is forced to move to this site (see Figure 4.4) in better agreement with HR (see Figure 4.5).

On 18 March, both simulations show high aerosol concentrations over Southeastern Iran, Southwestern Pakistan, and along the border of Iran, Pakistan, and Afghanistan (see Figure 4.4), where the second dust event originates. Both model simulations strongly underestimate the intensity of this dust outbreak in comparison with Aqua/MODIS AOD (Figure 4.2), which can be associated with several factors such as a poor representation of the alluvial sources, which are highly presented over the region. During this event, the dust outbreak moved south, affecting the Oman seacoasts and the Arabian Sea.

Jish Prakash et al. (2015) simulated the period between 17 and 20 March using the WRF-Chem model (at 10 km horizontal resolution and 40 vertical levels) to quantify the effects of severe dust events on radiation fluxes and regional climate characteristics in the Arabian Peninsula and the Red Sea. In this study, even though the magnitude of the simulated AOD at the Kaust Campus site was lower compared to that of AERONET during 19 March, the simulations were able to reproduce the peak AOD and the temporal dependence quite well as is the case with both LR and HR simulations used in the present study.

Discrepancies between different model configurations are not easily attributed to specific model aspects. The NMMB/BSC-Dust model's emission scheme is a function dependent on the cubic wind speed and several soil features above a given threshold (White, 1979). Misrepresentations of soil features (not studied here) and of wind speed can lead to emission bias. Furthermore, including a topographic preferential source mask in the model's emission scheme can inhibit the dust emissions in the western coast of the Arabian Peninsula. In order to improve the model's ability to estimate dust emission, several elements can be used in the model's emission schemes such as aeolian roughness derived from satellites as an indicator for the location of preferential sources and/or in the drag partition scheme (i.e. Menut et al. 2013) or the effect of the soil salt on threshold friction velocity for wind erosion (i.e. Hamidi et al. 2014).

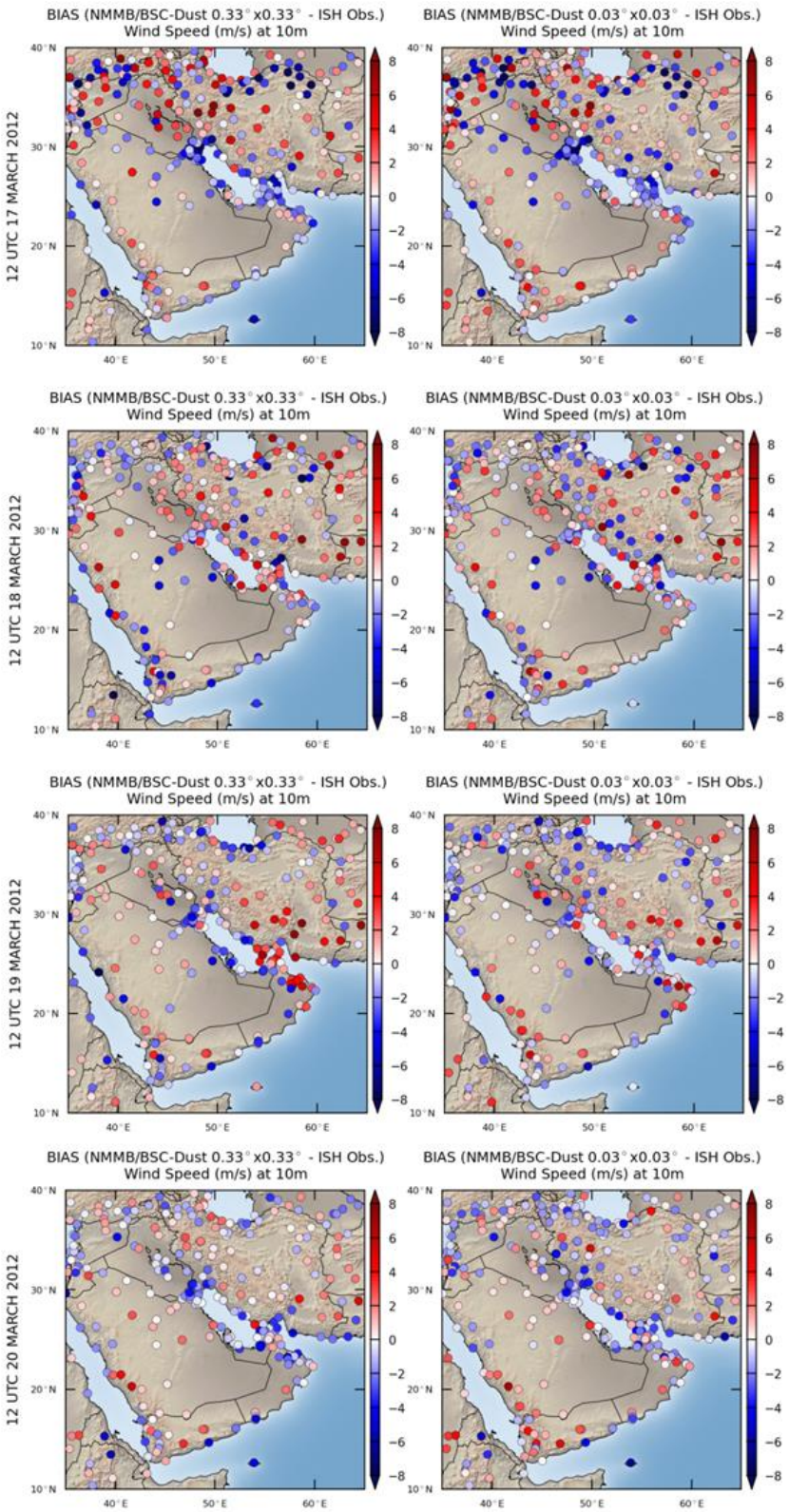

Figure 4.6: *Mean Bias between modeled and observed wind speed at 10 m at 12 UTC for the NMMB/BSC-Dust model with a horizontal resolution of 0.33º (LR; left column) and 0.03º (HR; right column).*

Both model configurations yield consistent and comparable results for the study of dust transport, despite differences in the magnitude of the simulated dust concentrations (see Figure 4.7). This is

linked to the fact that: (1) the mobilization of the dust outbreaks during the study period is from synoptic origin (see Section 4.1); therefore, similar general synoptic meteorological patterns are observed in both model configurations, and (2) no changes have been included in the emission scheme of the model for both model simulations. The highest surface winds in the high-resolution simulation (HR) cause an increase of emission linked to the emission of coarser particles that are rapidly removed by deposition given a total emission for the similar period (see Figure 4.7). In this sense, we want to highlight that the present study only analyzes the impact of the model resolution on the description of the terrain relief and its consequence in the aerosol propagation, not on the dust emission scheme, which is beyond the scope of this thesis.

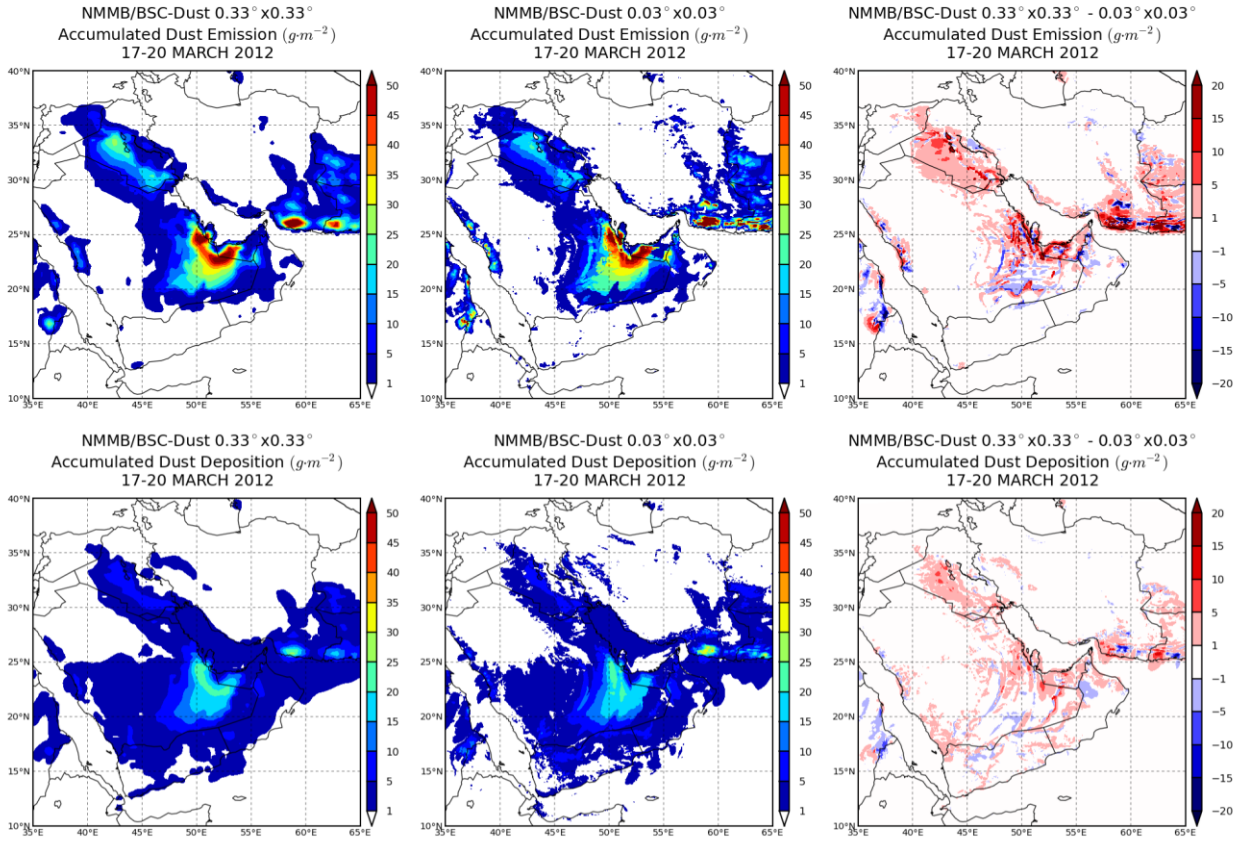

Figure 4.7: *Modeled accumulated emission (top row) and deposition (bottom row) fields from 17 to 20 March for the NMMB/BSC-Dust model with horizontal resolutions of 0.33º (LR; left column) and 0.03º (HR; middle column), and their respective differences (right column). The highest differences in the emissions close to mountains can be affected by the bilinear interpolation applied in the emission and deposition differences.*

4.6.3 Topographic effects on dust transport

In both presented dust events observed, the topography plays key roles in wind patterns that affect the blocking and changes the blowing dust trajectories. The Middle East is particularly sensitive to these topographic effects, and the model spatial resolution can be crucial in allowing for a better

representation of the dust propagation. In the present section, we focus on specific cases for both presented dust events where the topographic effect on wind patterns and dust propagation were relevant. The presented cases are based on 19 March: (1) dust blocking on Hadramawt in Yemen and Asir Mountains in Western Saudi Arabia and dust channeling between these mountains that extended over the Arabian Sea and the Red Sea; and (2) dust channeling in Southeastern Iran and Southwestern Pakistan and dust blocking in the Al-Hajar Mountains in Oman and the UAE.

The Hadramawt mountain ranges in Yemen are less represented in the LR simulation than the HR simulation (Figure 4.1). In both simulations, they are high enough to block the dust flow from Saudi Arabia on 18-20 March, causing a large accumulation of dust over inner Yemen and on the windward side of its mountains (Figure 4.4), as shown in the satellite aerosol products in Figure 4.2. However, the LR simulation omits the narrow valleys between the Hadramawt Mountains and river valleys to where the wind channels the dust and which are well-reproduced in the HR simulation (Figure 4.8e-l). Through some of these valleys, wind channeling transports dust towards the coastal areas – in the Gulf of Aden in the south and the Red Sea in the west. In comparison with the available surface weather stations, simulated wind fields are highly overestimated in the vicinity of these mountain ranges with local wind speed differences of up to 8 m/s (Figure 4.6) and large changes in the wind directions. Over the Arabian Sea, the HR simulation shows how intensified dusty winds (up to 18 m/s; Figure 4.3) through the valleys were able to describe these dust channeling structures in a qualitative comparison with satellite images (Figure 4.8a and Figure 4.8b).

As expected, the definition of the topography modifies the temperature's vertical structure profiles and consequently the dust peak. The higher mountain elevation of the HR simulation is also associated with stronger subsidence in the leeward of the Asir Mountains (see the cross sections along 15ºN and 45ºE in Figure 4.8). The rapid vertical dust extension over the high elevations observed in both model simulations with the peak of dust vertical mixing at about 15 UTC (see the cross section along 15ºN in Figure 4.8f and Figure 4.8g) are associated with the rapid growth of the planetary boundary layer (PBL) over the high elevations in the Western Arabian Peninsula, as indicated by Jish Prakash et al. (2015). The PBL in the Arabian Peninsula can be influenced by different mechanisms associated with coastal breezes, terrain, and surface properties. During the day, the surfaces of the mountains heat the air higher up in the atmosphere.

On 19 March at 12 UTC, both model simulations (LR and HR) predicted the arrival of a dust front into Oman, where it is blocked at low altitude by the Al-Hajar mountain range (Figure 4.4). The Mezaira AERONET site detected this dust flow on 20 March (Figure 4.5a) with observed AOD values between 1.5 and 2. Both simulations showed AOD peaks around 0.5, highly underestimating the magnitude of real dust intrusion.

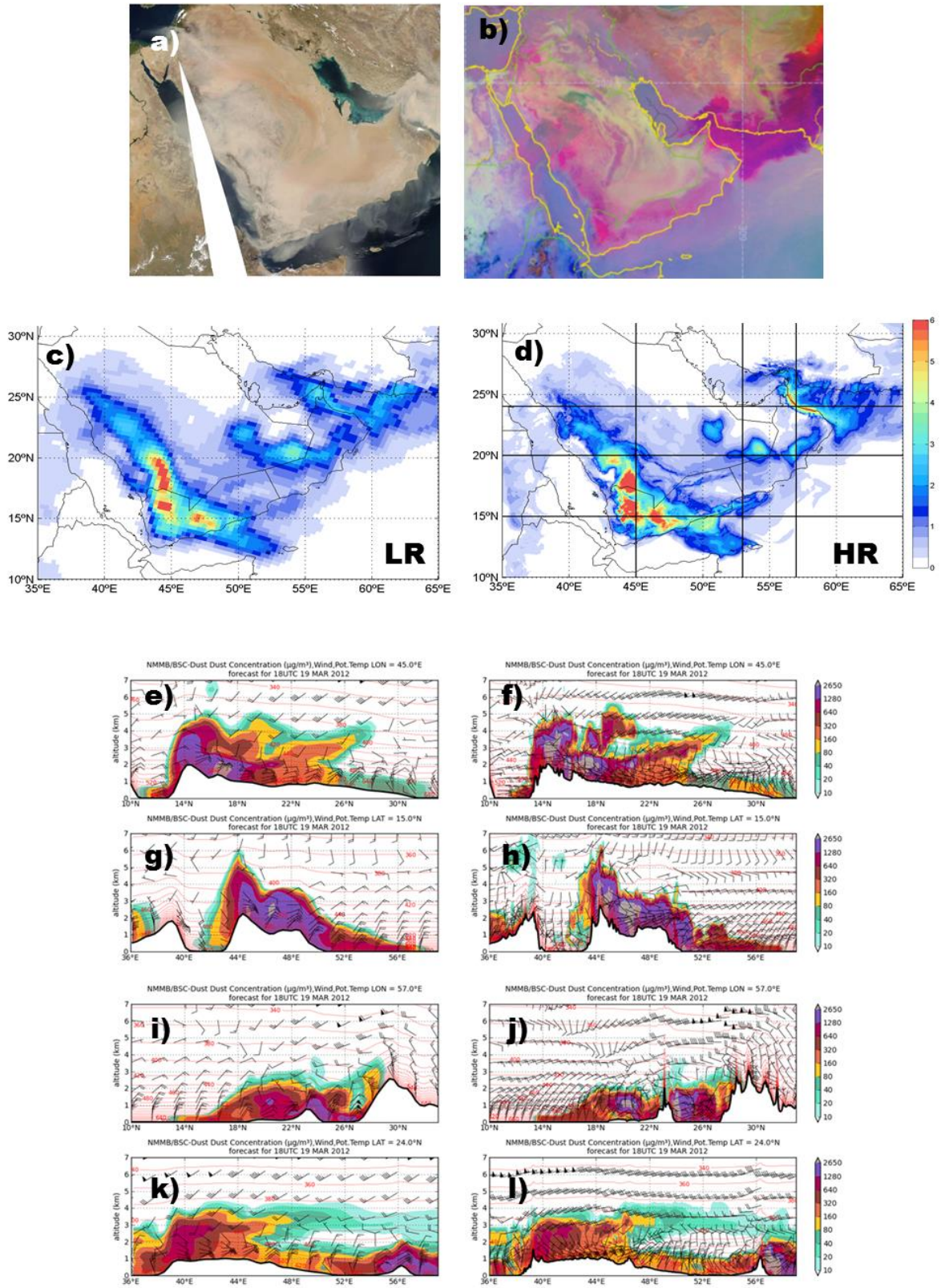

Figure 4.8: *(a) Aqua/MODIS at 09:50 UTC and 10:05 UTC on 19 March, (b) MSG/SEVIRI RGB image for 19 March at 15:15 UTC. Modeled dust load (in g/m^2) from 19 March at 15 UTC at for the NMMB/BSC-Dust model with horizontal resolutions of (c) 0.33º (LR) and (d) 0.03º (HR). (e-l) Modeled vertical dust concentration cross sections (in µg/m^3) at fixed latitudes (15ºN and 24ºN) and longitudes (45ºE and 57ºE) and on 19 March at 12 UTC for both LR and HR configurations.*

The LR simulation presented dust arrival to this station 12 hours earlier than the HR simulation (Figure 4.5), which is associated with a lower topography and fewer obstacles for wind flows, which were mostly overestimated along its trajectory towards the UAE. On the contrary, the blowing dust by winds in the HR simulation had to overcome and circle higher topographic obstacles, delaying its advance. Figure 4.8 shows how the higher topography simulated by the HR simulation left more dust particles on the Omani coast, especially in its central section where the highest mountains (with an altitude of around 3000 m; Figure 4.1) are found. The dust front is initially blocked by the mountains in Oman on 19 March and, consequently, low AOD values are shown on its leeward side on 20 March, as it is observed in the satellite images (Figure 4.2). Topographic effects on wind patterns (e.g. channeling or blocking) are better represented in the HR simulation with higher wind speed bias reductions and more realistic wind directions than in the LR simulation (Figure 4.3 and Figure 4.6). On 19 March at 15 UTC in Oman, both model simulations predict the dust arrival to the mountain system achieving altitudes above 3 km a.s.l (see the cross sections along 24ºN in Figure 4.8). In this event, the HR simulation is able to better reproduce the blocked dust mass upwind of the mountains observed in the MSG/SEVIRI RGB dust image, as it is shown in the cross sections along 24ºN at 15 UTC in Figure 4.8k. In the LR simulation, high concentrations are shown on its leeward side on 19 March at 15 UTC (AOD up to 5 in Figure 4.8c and concentrations above to 2650 $\mu g/m^3$ in Figure 4.8k) in comparison with concentrations predicted by the LR simulation (AOD up to 2 in Figure 4.8b and concentrations up to 2500 $\mu g/m^3$ in Figure 4.8j).

4.7 Conclusions

In the present chapter, two intense dust storms that occurred in the Middle East on 17-20 March 2012 that spanned thousands of kilometers from the Red Sea to Afghanistan and affected the whole Arabian Peninsula are studied. In both dust events, the topography plays key roles in wind patterns that affect the main trajectories of the blowing dust. This study analyzes the impact of model resolution on the description of the terrain relief and its consequence in the dust propagation. For that reason, two NMMB/BSC-Dust model simulations with horizontal resolutions of 0.03ºx0.03º (HR) and 0.33ºx0.33º (LR) horizontal resolutions are used to simulate the whole event.

Synoptic analysis done for the Middle East using the ERA-Interim and the NMMB/BSC-Dust models shows that on 17 March 2012, a dust storm developed as a result of a winter northwesterly Shamal wind crossing Iraq towards the Arabian Gulf. Satellite aerosol products (i.e. Aqua/MODIS AOD and MSG/SEVIRI RGB) and ground-based observations (surface weather and AERONET stations) show that the event achieves AOD values up to 5 and reduces visibility to less than 300 m. The NMMB/BSC-Dust model simulations indicate that the main dust sources during this event are in the river valleys of the lower Tigris and Euphrates in Iraq, Kuwait, Iran, the UAE and the Arabian Desert that includes the Rub Al Khali, An Nafud and Ad Dahna regions. Dust sources are also detected along

the Red Sea coast in the Western Arabian Peninsula. This dust storm affected all Arabian Gulf countries. This event was followed by another dust storm that formed over the Iran Desert on 18 March 2012, and moved south reaching Oman and the Arabian Sea during the following days.

The dust evaluation results demonstrate that despite differences in the magnitude of the simulated dust concentrations, both model configurations are able to reproduce these two dust outbreaks. Differences in the dust spread between both simulations appear in regional dust transport areas in Southwestern Saudi Arabia, Yemen and Oman where a complex topography with several peaks higher than 3000 m is present. Both model simulations present a delay of about 8 hours in the arrival of the dust front to the South Arabian Peninsula. This is linked to the meteorological data required to initialize the atmospheric part of the model and because updating its boundary conditions can introduce uncertainties. On 19 March, the model overestimates dust emissions in Rub Al Khali Desert (Saudi Arabia) and underestimates the event with origin in Southern Iran. The overestimation in Rub Al Khali Desert is associated with coarse fractions that are rapidly removed from the atmosphere. Otherwise, underestimations in Iran are linked to a combination of the poor representations of the desert dust sources in the model.

It is not straightforward to attribute the discrepancies to specific aspects of the model since the emission scheme depends on multiple surface, soil, and meteorological features and includes threshold processes and non-linear relationships. In this sense, the topographic preferential source map used in the model does not describe the sources located on the western coast of the Arabian Peninsula well, leading to an underestimation of the dust emission. These results highlight the need to revise the land-surface datasets used by the model to generate the source mask over the Middle East.

The analysis of both model configurations (LR and HR) on 19 March shows that the complex orography in Southwestern Saudi Arabia, Yemen, and Oman modifies the simulated dust concentration fields over mountain regions. On 19 March, the first dust front is blocked by the mountains in Southwestern Saudi Arabia, Yemen, and Oman and spread through the valley that channelizes the dust flow towards the Arabian Sea. On the other hand, the second dust front associated with the dust outbreak with its origin in Iran is blocked by the Al-Hajar Mountains in Northeastern Oman, forcing dust to move towards the Arabian Sea. Differences between both model configurations are mainly associated with the description of the topography and its effects on meteorology such as changes in wind speed and direction (e.g. channeling or blocking winds) that modify transport of dust.

The present analysis demonstrates the benefits of using high-spatial-resolution simulations to refine the description of mountain systems and consequently improve the prediction of regional dust transport fields over the Middle East.

Chapter 5

5 Investigating the predictability of convective dust storms

5.1 Background

Haboobs have been documented in many regions worldwide, for example, in North America (Vukovic et al., 2014), the Middle East (Miller et al. 2008; Karami et al. 2017; Solomos et al. 2017), Eastern Africa (Sutton, 1925; Farquharson, 1937; Kalenderski and Stenchikov, 2016), Western Africa (Knippertz et al., 2009; Marsham et al., 2013), the Taklimakan and Gobi deserts in China (Takemi, 1999, 2005) and Australia (Strong et al., 2011). The Western Sahara shows a significant occurrence of haboobs, which can contribute to half of its total dust emissions in summer (Allen et al. 2013; Heinold et al. 2013; Marsham et al. 2013). The Saharan Heat Low (SHL; see Figure 1.7) has been identified as a major component of the West African monsoon system and is linked to the latitude shift of the ITCZ (Engelstaedter et al., 2015; Lavaysse et al., 2016). Moist air inflows from the Mediterranean, the North Atlantic coast of Western Africa, and the Gulf of Guinea to the SHL allow the development of mesoscale convective systems (MCSs), which can develop cold pools over dust sources and thereafter produce haboobs (Engelstaedter et al., 2015). Satellite analysis based on CALIOP observations (Todd and Cavazos-Guerra, 2016) show a zone extending through Southern Algeria, Northern Mali, and Northwestern Niger, on the southwestern margins of the Hoggar Mountains and the northwestern margins of the Aïr Mountains, where frequent emissions are observed in summer coinciding with the western edge of the SHL.

Moist convection and associated cold pool outflows can produce haboobs, although their contribution to the dust global budget is still uncertain (Knippertz and Todd, 2012). In Northern Africa, their contribution can be up to 30% of dust emissions during summer (Pope et al., 2016). Typically they are developed in the late afternoon and span hundreds of kilometers over arid regions (Knippertz and Todd, 2012; Solomos et al., 2012). As shown in Chapter 3, model simulations at global and regional scales (from ~ 100 to 10 km) tend to underestimate haboob events in comparison with ground-based observations. Model runs with horizontal resolutions above ~10 km tend to parameterize convective clouds, which results in a simulated convection that produces too much light rainfall and too little intense rainfall, with the peak in rainfall too early in the day (Stephens et al. 2010; Dirmeyer et al. 2012; Marsham et al. 2013).

Several model experiments highlighted the importance of small-scale processes (e.g. deep convection and planetary boundary layer processes) in the dust emission. Reinfried et al. (2009) and Solomos et al. (2012) studied some convective phenomena over the Atlas region (Northwestern Africa) between May and June 2006 using the LM-MUSCAT and RAMS/ICLAMS models, respectively. Both studies used horizontal resolutions ranging from 24 to 0.8 km and concluded that horizontal resolutions lower than 4 km more realistically resolved convective processes. Heinold et al. (2013) identified cold pools

and the breakdown of the nocturnal low-level jet (NLLJ) as key meteorological drivers of dust emission over Western Africa using the UK MetUM model with a horizontal resolution of 4 km. This study permitted the reproduction of a large number of dust drivers; however, it also revealed the need for a better representation of the moist convection and stable nighttime conditions. Marsham et al. (2013) used simulations from the Cascade project to demonstrate the impact of the representation of convection on the large-scale circulation. Their main findings showed that explicit runs were able to develop moist convection and cold pools, although their timing and strength developed better with 4 km than with 12 km. Furthermore, at the parameterized convection run with 12 km, convection was triggered too early and cold pools were essentially absent. Vukovic et al. (2014) performed an analysis of a single severe dust storm over the Southwestern United States using model simulations from a regional dust model (NMME-DREAM) with a horizontal resolution of 3.5 km. The model predicted the position of the dust front, the rapid uptake of dust and high values of the storm's dust concentration in space and time. However, the model showed a delay of about 1 hour in its arrival to Phoenix due to the lack of precision of the atmospheric model in predicting such severe dust events. Kalenderski & Stenchikov (2016) applied the WRF-Chem model at 2.5 km horizontal resolution to reproduce typical summertime dust events over Eastern Africa and the Arabian Peninsula. Severe dust outbreaks were identified including haboobs caused by cold pools from MCSs, which were successfully resolved explicitly by the model. However, the simulated maximum dust concentration was underestimated in comparison with the ground-based and satellite observations. Solomos et al. (2017) addressed the simulation of a haboob by using the regional RAMS/ICLAMS model with a horizontal resolution of 2 km. The extreme dust storm that originated in Syria and Northern Iraq and moved toward Cyprus in September 2015 was reproduced well by the model in comparison with observations (e.g. location and height) but underestimated the maximum dust concentration by almost 50%. According to these mentioned studies, non-hydrostatic models with horizontal resolutions of at least 4 km and with explicit convection runs are required to simulate a more realistic timing and strength of deep convection and cold pool outflows.

The present chapter aims to better understand the simulation of haboobs and to explore the NMMB/BSC-Dust model's ability for reproducing them. For that reason, five model experiments for both explicit and parameterized convection and different (horizontal and vertical) spatial resolutions are used under a convective situation that occurred in Western Africa on 14 July 2011. This chapter is organized as follows: Section 5.2 describes the case study. Section 5.3 presents the modeling experiments. Section 5.4 discusses the results of the modeling experiments with a special focus on two convective systems. Finally, Section 5.5 is devoted to the conclusions of the work.

5.2 Case study

The present analysis is centered on a study domain covering Southern Algeria, Northeastern Mali, and Northwestern Niger (16.5ºN-30ºN and 4ºW-10ºE) on a convective situation during 14 July 2011. This region is characterized by areas with high topography, such as the Aïr Mountains in Northwestern Niger (where steep mountains are over 1400 m in height) and the Hoggar Mountains in Southern Algeria (where heights are higher than 2000 m in height). At synoptic scale, a low-pressure system appears over Northeastern Mali on 14 July (Figure 5.1). The cyclonic circulation is associated with a moist monsoon flow coming from the south and southwest in Northeastern Mali and Northwestern Niger, and with drier winds coming from the north and northeast in Southern Algeria. This unstable situation favored the development of convective regions where thunderstorms develop along during the day (see Figure 5.2). The presence of dust (pink color in the MSG/SEVIRI RGB product in Figure 5.2, see Section 4.4.1.1 for further information about this satellite product) was also observed under the cloud masses from mature convective storm cells as a consequence of cold pool outflows.

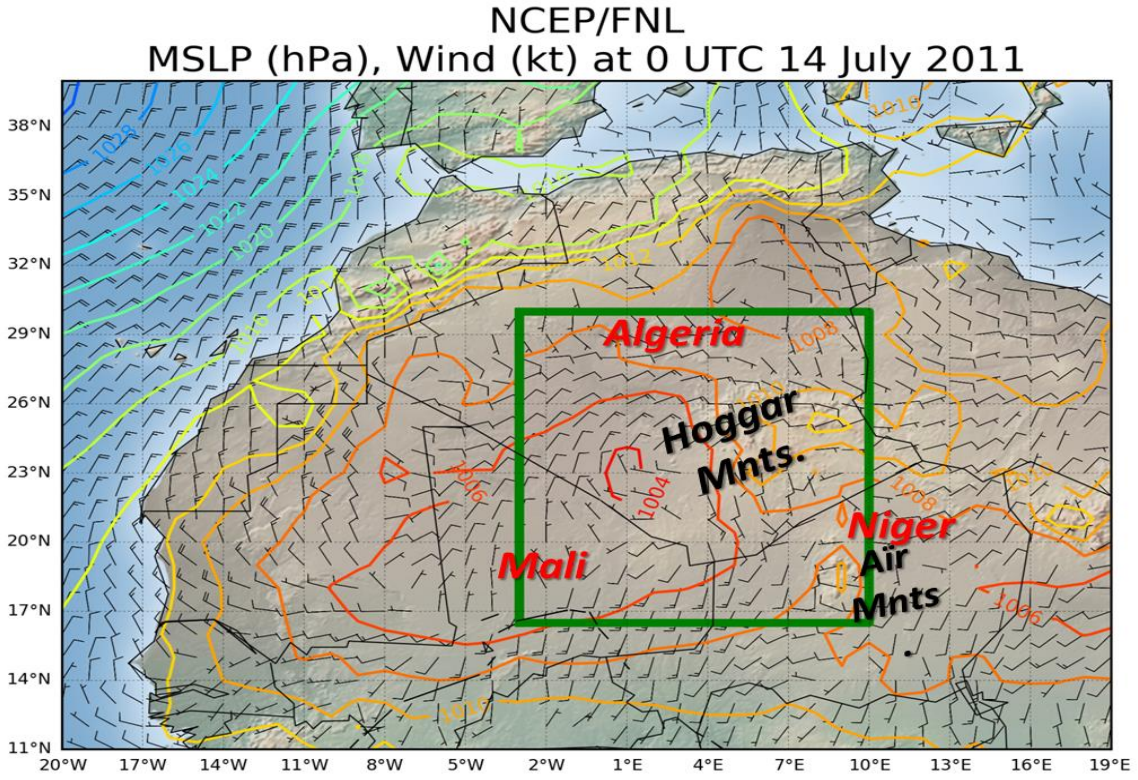

Figure 5.1: *Mean Sea Level Pressure (MSLP) in hPa and surface winds (barbs) at 0 UTC on 14 July 2011 from NCEP/FNL analysis over Northwestern Africa. The green rectangle marks the study domain (16.5ºN-30ºN and 4ºW-10ºE) used in the present chapter, which covers Southern Algeria (central and upper region), Northeastern Mali (bottom-left region), and Northwestern Niger (bottom-right region).*

5.3 Model setup

The present study uses five NMMB/BSC-Dust model configurations (see Table 5.1) that differ in terms of the horizontal and vertical resolutions, and in turning on or off the convective scheme of BMJ included in the model (see Chapter 2). The proposed model runs are: (1) 0.03ºx0.03º horizontal resolution, 100 σ-layers and explicit convection (R3NONE100), (2) 0.03ºx0.03º horizontal resolution, 60 σ-layers and explicit convection (R3NONE60), (3) 0.10ºx0.10º horizontal resolution, 40 σ-layers and explicit convection (R10NONE40), (4) 0.03ºx0.03º horizontal resolution, 60 σ-layers and parameterized convection (R3BMJ60), and (5) 0.10ºx0.10º horizontal resolution, 40 σ-layers and parameterized convection (R10BMJ40). All model simulations are run for 24 hours from 0 UTC 14 July to 0 UTC 15 July 2011, and cover Southern Algeria, Northeastern Mali, and Northwestern Niger (see Figure 5.1). In all model configurations, the top of the model domain is at 50 hPa. The simulations used the meteorological NCEP/FNL analysis as initial conditions at 0 UTC and as boundary conditions every 6 hours. This model version does not include dust data assimilation and the initial state of the dust concentration is zero. The meteorological model uses the following parameterizations: the Ferrier microphysics scheme, the Noah land surface model for the treatment of moisture and heat surface fluxes, the radiative RRTMG model for longwave and shortwave radiation and the Mellor-Yamada-Janjic turbulence scheme. All experiments include a calibration factor of 0.255.

Table 5.1: *Summary of the main features of the five model configurations: horizontal resolution, horizontal grid points, number of vertical layers, number of layers in the first 1 km, height of the 1st layer, fundamental time steps, and convection mode.*

Configuration	R3NONE100	R3NONE60	R10NONE40	R3BMJ60	R10BMJ40
Horizontal resolution	0.03ºx0.03º	0.03ºx0.03º	0.10ºx0.10º	0.03ºx0.03º	0.10ºx0.10º
Horizontal grid points	501x501	501x501	151x151	501x501	151x151
Number of vertical layers (σ)*	100	60	40	60	40
Number of vertical layers (< 1 km)	21	12	8	12	8
Height of the 1st layer (m)	18	31	44	30	44
Fundamental time steps (s)	5	5	25	5	25
Convection mode	Explicit	Explicit	Explicit	BMJ scheme	BMJ scheme

*top of the atmosphere at 50 hPa

5.4 Results and discussion

Figure 5.2 shows composite figures for the five model configurations with simulated fields of the wind at 10 m (barbs), dust optical depth at 550 nm (DOD; pink shaded color), cloud fraction (red shaded color), and 1-hourly accumulated rainfall (green-blue shaded color) to compare qualitatively with the MSG/SEVIRI RGB dust product at 11, 17 and 21 UTC. Figure 5.3 presents the spatial distribution of the daily accumulated dust emissions over the study domain for all configurations. The model simulates three main dust events during 14 July in Southern Algeria (at 27ºN), Northwestern Niger (DOM1 in Figure 5.3), and Northeastern Mali (DOM2 in Figure 5.3). In Southern Algeria at 27ºN, daily accumulated dust emissions appear below 15 g/m^2, in which all configurations simulate similar spatial distributions and magnitudes. On the other hand, daily accumulated dust emissions higher than 15 g/m^2 appear in Northwestern Niger (DOM1) for explicit runs, and in Northeastern Mali (DOM2) for all configurations, except in R10BMJ40.

At 11 UTC, all model configurations develop a thunderstorm formed by orographic convection over the Aïr Mountains in Northwestern Niger, although around two hours earlier than the MSG/SEVIRI RGB satellite observations. The model reproduces a second storm cell (with associated dust emissions) covering Northeastern Mali and Southern Algeria in agreement with the MSG/SEVIRI satellite. Otherwise, all model runs simulate a large-scale dust storm in Algeria (DOD > 0.5 around 27ºN), which is not visible in the MSG/SEVIRI RGB dust images. At 17 UTC, according to satellite images, haboobs develop under these storms and move westwards in Southern Algeria and Northeastern Mali, which can be identified by satellite images as a pink arc in the western edge of the cloud masses. All model configurations predict three storms in Northeastern Mali, Northwestern Niger and Southern Algeria that move westwards in agreement with those observed by satellite. At 21 UTC, satellite images show a thick dust mass moving toward the northwest in Southern Algeria, which all model configurations do not reproduce. Despite that, the model can reproduce the haboobs associated with the storm cells in Northeastern Mali and Northwestern Niger.

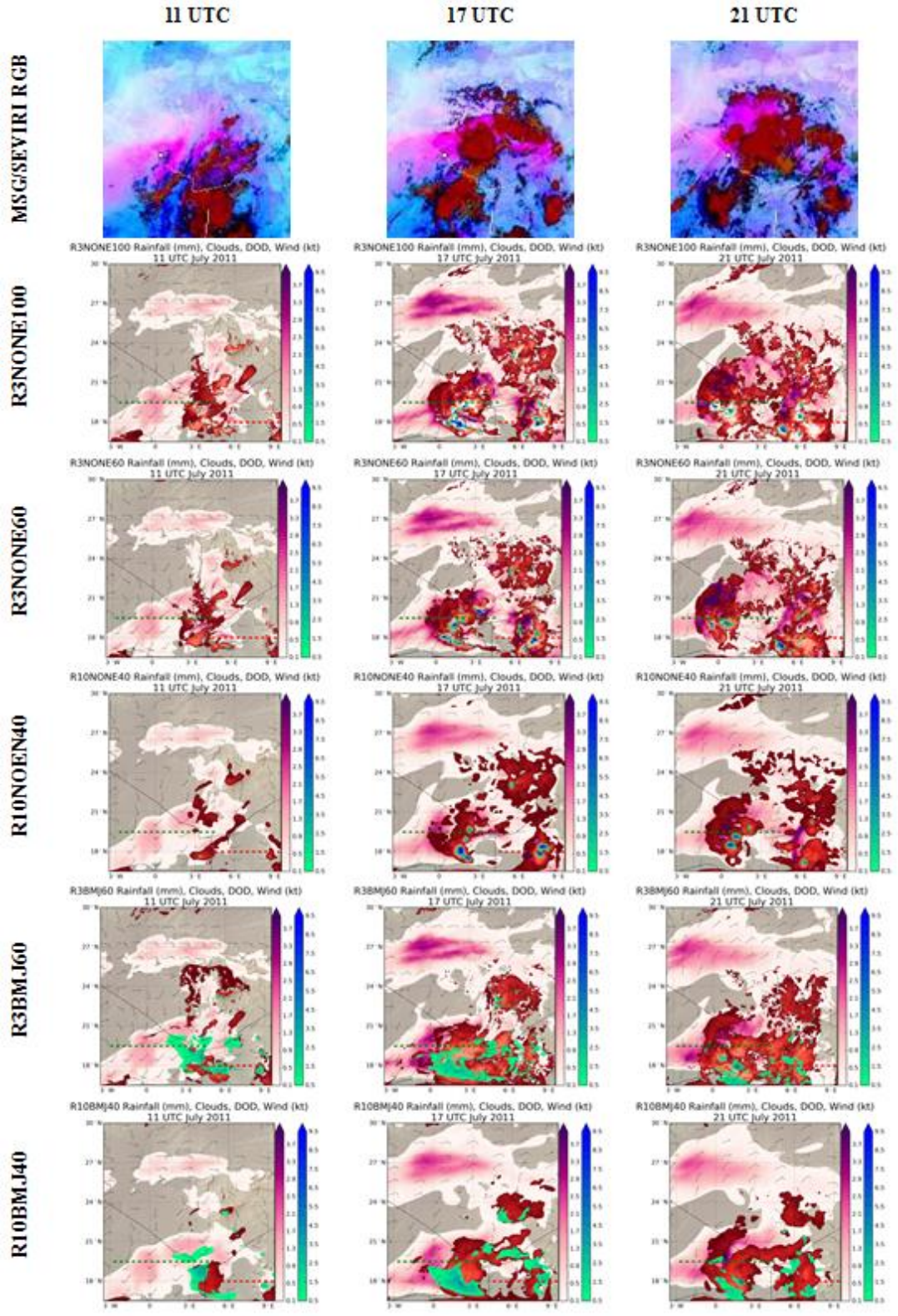

Figure 5.2*: The MSG/SEVIRI RGB dust product (1st row, see Section 4.4.1.1 for further information about this satellite product), and the model results show the wind at 10 m (barbs), 1-hourly accumulated rainfall (mm) in green-blue, cloud cover (red colors), dust optical depth at 550 nm (DOD, pink colors) in R3NONE100 (2nd row), R3NONE60 (3rd row), R10NONE40 (4th row), R3BMJ60 (5th row), and R10BMJ40 (6th row) at 11, 17, and 21 UTC (from left to right columns).*

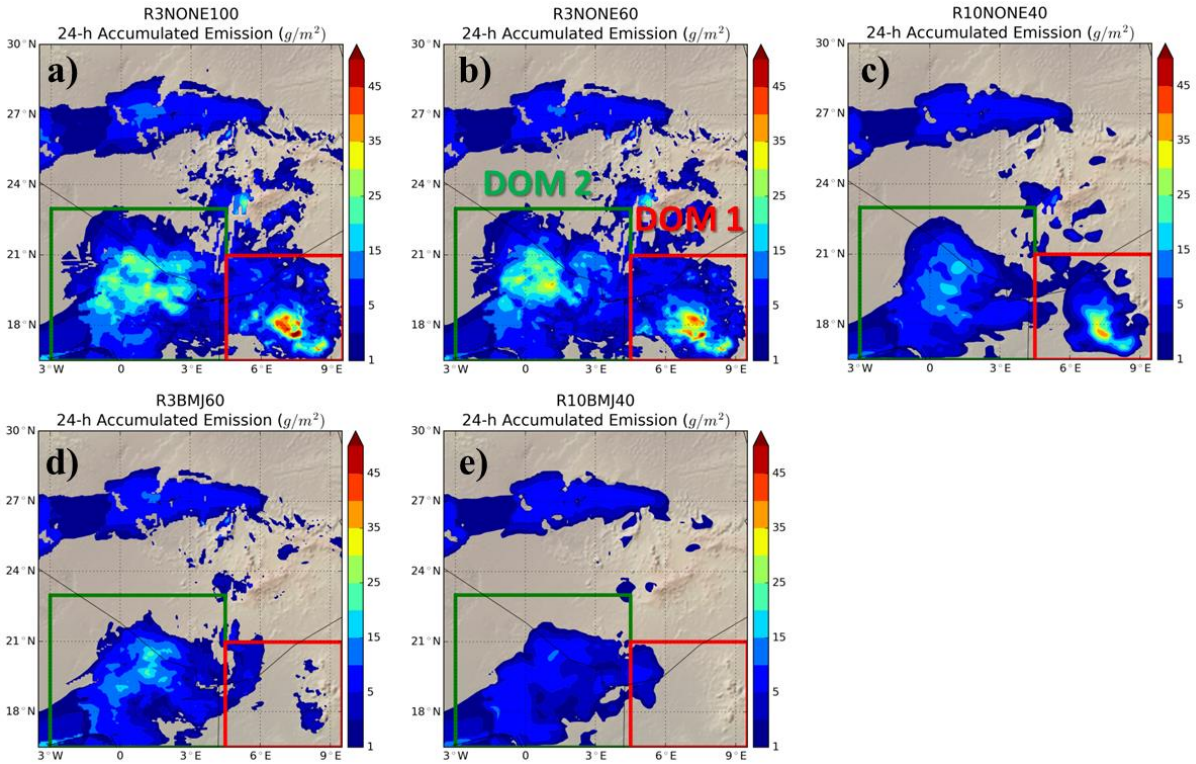

***Figure 5.3**: Daily accumulated dust emission (g/m^2) on 14 July 2011 covering the study domain (16.5ºN-30ºN and 4ºW-10ºE) in (a) R3NONE100, (b) R3NONE60, (c) R10NONE40, (d) R3BMJ60, and (e) R10BMJ40. All figures contain two rectangles: DOM1 (red rectangle; 4.5ºE-9.5ºE and 16.5ºN-21ºN) and DOM2 (green rectangle; 3ºW-4.5ºE and 16.5ºN-23ºN).*

Daily accumulated dust emitted masses for the whole domain and the two sub-domains (DOM1 and DOM2) are computed on Table 5.2. Considering the whole domain, daily accumulated dust emitted masses per model configuration are as follows: 7.54 Tg (R3NONE100), 6.90 Tg (R3NONE60), 4.31 Tg (R10NONE40), 3.68 Tg (R3BMJ60), and 2.73 Tg (R10BMJ40). These emissions show that those configurations with higher spatial resolutions and those that resolve explicit convection (i.e. R3NONE100 and R3NONE60) produce higher dust emissions than those lower spatial resolutions and parameterized convection. Explicit runs (i.e. R3NONE100, R3NONE60 and R10NONE40) provide higher values and more widely distributed spatial fields in terms of DOD patterns, and in terms of rainfall patterns they provide later, more intense (in the downdraft area) rainfall with a smaller spatial distribution compared to parameterized runs.

The main differences between configurations appear in DOM1 and DOM2 because the genesis of the convective systems developed. In Northwestern Niger, an isolated thunderstorm originated by orographic convection over the local steep topography as it is indicated by the high-CAPE availability Figure 5.4c). Otherwise, in Northeastern Mali, the storm cell developed over low topography as a result of intense surface heating, monsoon moist flow from the south and southwest, and large-scale lifting by the low-pressure system.

The next sections focus on the two convective dust events that developed in Northwestern Niger (DOM1) and Northeastern Mali (DOM2).

Table 5.2: *Daily accumulated dust emitted mass (Tg) computed for the whole domain, DOM1 and DOM2 (see Figure 5.3) in R3NONE100, R3NONE60, R10NONE40, R3BMJ60 and R10BMJ40.*

Domain	Lat-Lon range	Daily accumulated emitted dust mass (Tg)				
		R3NONE100	R3NONE60	R10NONE40	R3BMJ60	R10BMJ40
Total	(16.5ºN-30ºN; 3.5ºW-9.5ºE	7.54	6.90	4.31	3.68	2.73
DOM1	16.5ºN-21ºN; 4.5ºE-9.5ºE)	1.92	1.89	0.96	0.21	0.17
DOM2	(16.5ºN-23ºN; 3ºW-4.5ºE)	3.82	3.42	2.16	2.14	1.45

5.4.1 Convective event in Northwestern Niger

In Northwestern Niger (DOM1 in Figure 5.3), significant dust emissions caused by intense cold pool outflows from a thunderstorm appear in explicit runs (i.e. R3NONE100, R3NONE60 and R10NONE40); meanwhile, such dust emission drivers are practically absent in parameterized runs (i.e. R3BMJ60 and R10BMJ40). In explicit runs, emission areas appear near the southern and western foothills of the Aïr Mountains. Both R3NONE100 and R3NONE60 show similar daily emitted dust masses of ~1.9 Tg with similar emission areas, but more intense emission peaks appear in R3NONE100, with maximum daily dust emissions of about 45-55 g/m^2, than in R3NONE60, with emission peaks that reach 40-50 g/m^2 (Figure 5.3). Otherwise, R10NONE40 only reaches half of those daily emitted masses (0.96 Tg), and its main emission area extends closer to the mountain area with weaker daily emission peaks that do not exceed 40 g/m^2. In parameterized runs, emissions only appear in R3BMJ60 in the vicinity of the Aïr Mountains with daily emissions lower than 5 g/m^2.

Before 6 UTC, weak winds of ~3 m/s (on average) are predominant over DOM1 and sharply intensify up to ~5.5 m/s (on average) from 6 to 9 UTC by the breakdown of the NLLJ. All model configurations similarly reproduce the wind patterns with mean wind speed differences lower than 0.5 m/s (Figure 5.4a), although higher maximum wind speed values are found in explicit runs with higher spatial resolutions (i.e. R3NONE100 and R3NONE60). Dust emissions largely differ between model configurations, since dust emission fluxes are highly sensitive to higher wind values because they are proportional to the third power of the surface wind friction velocity. Since 8 UTC, an unstable atmospheric situation is marked in all configurations by the increase of the maximum convective

available potential energy (CAPE) (Figure 5.4c), which favors the development of a thunderstorm over the Aïr Mountains at 11 UTC (Figure 5.2).

Parameterized runs (i.e. R10BMJ40 and R3BMJ60) sharply remove CAPE (Figure 5.4c) at 10 UTC by the rearrangement of the moisture and temperature profiles produced by the BMJ scheme. As a result of this rearrangement, both parameterized runs provide early initialization of precipitation and high rainfall values (see Figure 5.4d), with daily accumulated values in Northwestern Niger (DOM1) of 1042 mm for R10BMJ40 and 1003 mm for R3BMJ60. R3BMJ60 develops strong downdrafts, which are easily identified by the sharp increase in maximum downdraft velocities up to ~3 m/s at 11-12 UTC (Figure 5.4f). However, these downdrafts are short-lived, and their intensity quickly drops after values of 1.5-2 m/s, when CAPE also drops. In R10BMJ40, vertical velocities remain below 1 m/s during the whole event. The BMJ scheme negatively impacts the formation of intense cold pool outflows, high surface winds, and consequently, high dust emissions (Figure 5.4).

Otherwise, explicit runs (i.e. R3NONE100, R3NONE60 and R10NONE40) start decreasing their CAPE (Figure 5.4c) after 11 UTC by the development of cold pool outflows, which is followed by an increase in the rainfall in the downdraft area (Figure 5.2), although with lower daily accumulated values (370 mm in R3NONE100, 373 mm in R3NONE60, and 205 mm in R10NONE40) than compared to parameterized runs (Figure 5.4d). As a consequence of the cold pool outflows, explicit runs develop intense vertical velocities in the first 3 km in height (see Figure 5.4f) and reduce surface temperatures (Figure 5.4e). Both R3NONE60 and R3NONE100 sharply increase their maximum downdraft velocities from 8 up to 11 UTC from ~2 to ~5 m/s in absolute values (hereafter downdraft values are referred to as absolute values), respectively. R10NONE40 develops its maximum downdraft velocities later (initiated at 11-12 UTC) and with weaker values (lower than 2 m/s) than compared to both R3NONE100 and R3NONE60. Otherwise, maximum updrafts are weaker than their respective maximum downdrafts in each configuration with values of ~3 m/s both for R3NONE100 and R3NONE60 and ~1 m/s for R10NONE40. These differences in the timing and strength of the downdrafts between runs are consistent with the study of haboobs during the SAMUM campaign presented in Marsham et al. (2013). After 12UTC, explicit runs show an increase in surface mean wind speeds and emissions by the strong development of cold pool outflows and gravity currents. Both R3NONE60 and R3NONE100 reach maximum mean wind speeds of ~6.5 m/s at 18 UTC and hourly emitted masses of ~0.29 Tg at 17 UTC. Meanwhile, the R10NONE40 run reaches a mean wind speed peak of 5.2 m/s at 19 UTC and hourly emitted dust masses of ~0.15 Tg (from 17 to 19 UTC). After 19 UTC, the gravity currents progressively weaken resulting in a decrease of surface wind speeds and emissions.

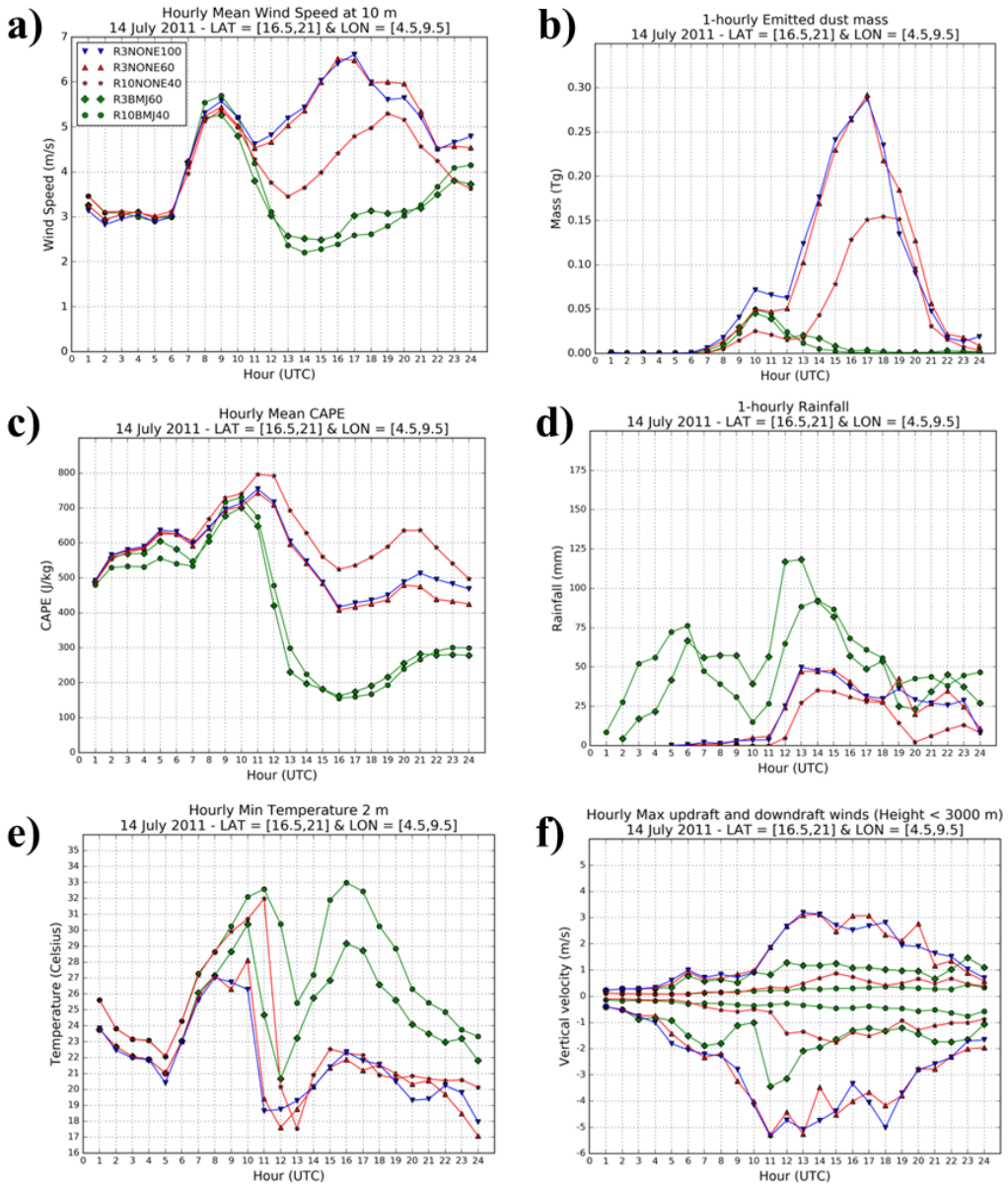

Figure 5.4*: Time series on an hourly basis of: (a) emitted dust mass (Tg), (b) mean wind speed at 10 m (m/s), (c) mean of maximum convective available potential energy (CAPE(J/kg)), defined as the accumulated buoyant energy from the level of free convection to the equilibrium level, (d) rainfall (mm), (e) maximum values of the updraft and downdraft vertical velocities (m/s) in the first 3000 m (tropospheric layer where cold pool outflows develop; see Figure 5.7), and (f) minimum temperature at 2 m (ºC) in Northwestern Niger (DOM1; see Figure 5.3) in R3NONE100, R3NONE60, R10NONE40, R3BMJ60, and R10BMJ40 (see Table 5.1).*

Cold pool outflows are identified in both R3NONE100 and R3NONE60 by small circles on the peaks of the Aïr Mountains where low temperatures (18-21ºC) meet high surface wind speeds (13-16 m/s) at 11 UTC (Figure 5.5). The newly formed cold pool outflows propagated horizontally toward the west and met ~200 km away from the Aïr Mountains, finally acting as a single gravity current with a fast dust mobilization. At 17 UTC, surface variables in Northwestern Niger show well-developed cold pools (low temperatures of 21-24ºC in explicit runs), gravity currents (surface wind speeds of 15-18

m/s in both R3NONE100 and R3NONE60 and 12-15 m/s in R10NONE40), and dust fronts (higher surface dust concentrations than 30.000 μg/m^3) in the shape of an arc for the three explicit runs, as shown in Figure 5.6. The main differences between those configurations are found in surface dust concentrations. R3NONE100, with maximum surface dust concentrations of 50.000 μg/m^3, is more effective at uplifting dust with surface dust concentrations of 5.000-10.000 μg/m^3 higher than R3NONE60. Otherwise, R10NONE40 develops the main cold pool outflows an hour later, and it is weaker than in the finer spatial resolutions of both R3NONE100 and R3NONE60 that find its dust front located around 50 km closer to the mountain range. In R10NONE40, the haboob's body contains dust concentrations slightly higher than 30.000 μg/m^3 and a horizontal extension of 60 km (Figure 5.6). The simulated haboobs by R3NONE60 and R3NONE100 lasted around 10 h, spreading over a distance of 400 km in the west direction and forming a maximum front line of over 400 km in length. In R10NONE40, dust propagation lasted 8-9 h, covering a shorter distance of over 300 km and developing a maximum front line of over 350 km in length.

Figure 5.7 presents vertical cross sections along 18ºN of model results from the three explicit runs (i.e. R3NONE60, R3NONE100 and R10NONE40) at 17 UTC. At that time and latitude, the haboob and the meteorological processes, such as intense vertical velocities, cold pool outflows, and gravity currents, are well-identified. Strong vertical velocities develop under the cloud mass (up to 3.5-4 km in height) where the descending cold air forces warm air upward on the leading edge of the haboob, located on the west edge at 6ºE. Maximum downdraft and updraft speeds develop around the mid-column height (~1.5-2 km). Both R3NONE100 and R3NONE60 develop similar maximum vertical velocities in downdrafts of 3-4 m/s and in updrafts of 2-3 m/s. Otherwise, R10NONE40 reproduces weaker vertical velocities (up to 1 m/s) and this turns out to be insufficient to develop the "wall of dust" on the haboob's front edge. Microphysical processes associated with cold pool outflows are the melting and evaporation of precipitation, which cools the air and provokes the downdraft under the cloud. In the area where the cold pool outflows are identified, the specific humidity increases with values of 10 g/kg on its boundaries (brown contour lines in the vertical velocity plot) and up to 16 g/kg on the ground (blue contour lines). Vertical cross sections of the horizontal wind speeds show the formed gravity currents (higher wind speed than 15 m/s) pushing the air masses toward the leading edge. Both R3NONE60 and R3NONE100 show maximum horizontal wind speeds at 200-500 m in height with higher values in R3NONE100 (24-28 m/s) than in R3NONE60 (20-24 m/s). Those wind speeds progressively reduce vertically up to 14-16 m/s at 1.5-1.8 km in height. R10NONE40 shows lower vertical extension (up to 1 km) of horizontal wind speed with maximum values of ~20 m/s at 200-300 m in height. As a consequence of these strong wind speeds, R3NONE60 and R3NONE100 simulate dust fronts which are characterized by a main dust body of 500 m in height and a horizontal extension of 100-150 km that contains dust concentrations higher than 20.000 μg/m^3, moving west. The highest dust concentrations are found at the bottom (up to 200 m) of the front edge reaching peaks

of about 40.000 µg/m^3 that exponentially decrease in height until 2.5 km, where concentrations are below 1000 µg/m^3. R3NONE100 is more effective at uplifting dust vertically than R3NONE60, with higher concentrations of 5.000-10.000 µg/m^3 up to 500 m. Otherwise, R10NONE40 presents a weaker vertical development, with dust concentrations lower than 30.000 µg/m^3 in the first 300 m in height.

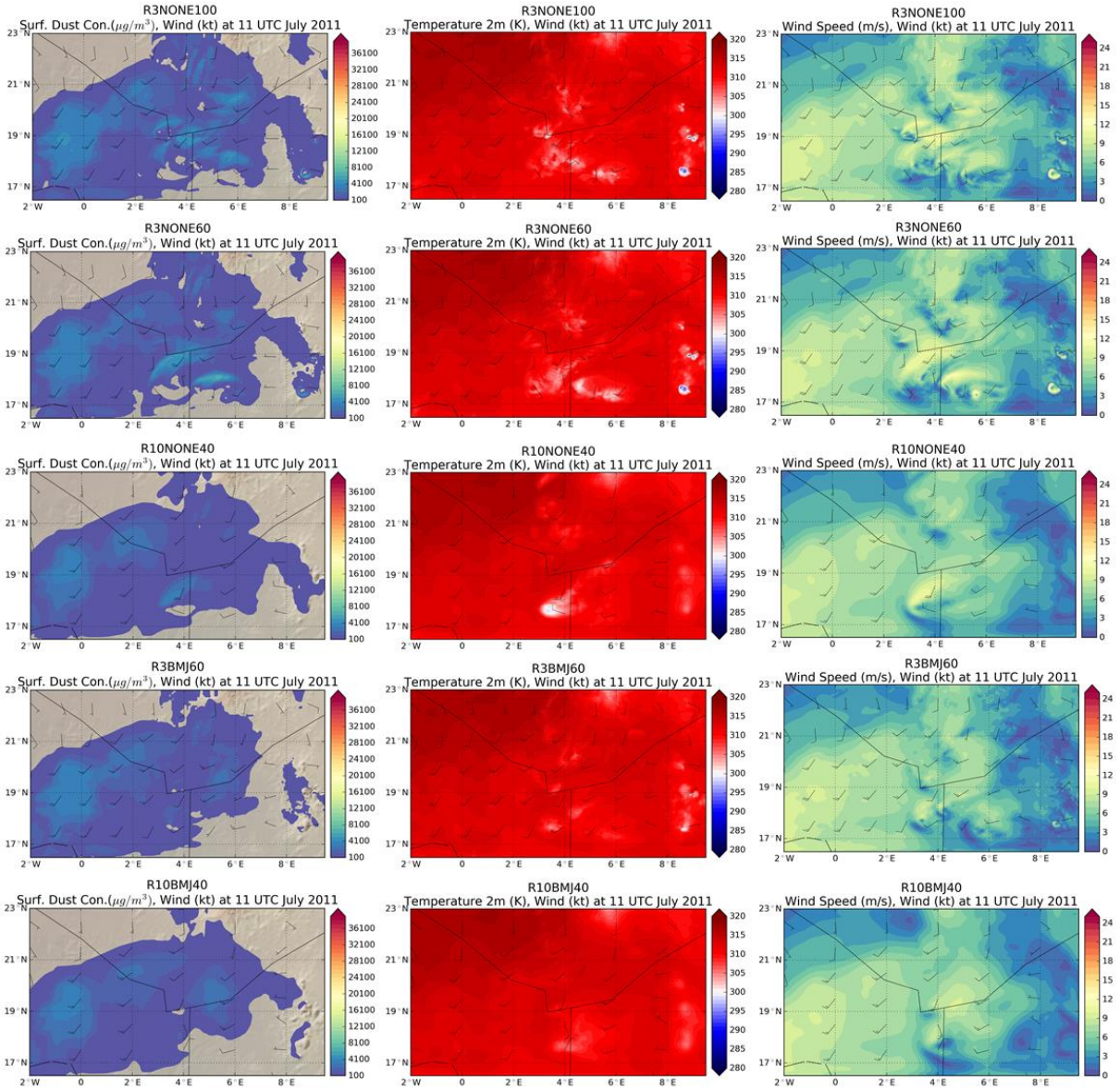

Figure 5.5: *Surface dust concentration (µg/m^3) (left panels), temperature at 2 m (K) (middle panels), and horizontal wind speed at 10 m (m/s) (right panels) covering DOM1 and DOM2 (2ºW-9.5ºE and 16.5ºN to 23ºN; see Figure 5.3) in R3NONE100, R3NONE60, R10NONE40, R3BMJ60, and R10BMJ40 (from top to bottom) at 11 UTC. Additionally, all panels contain the horizontal wind at 10 m (barbs).*

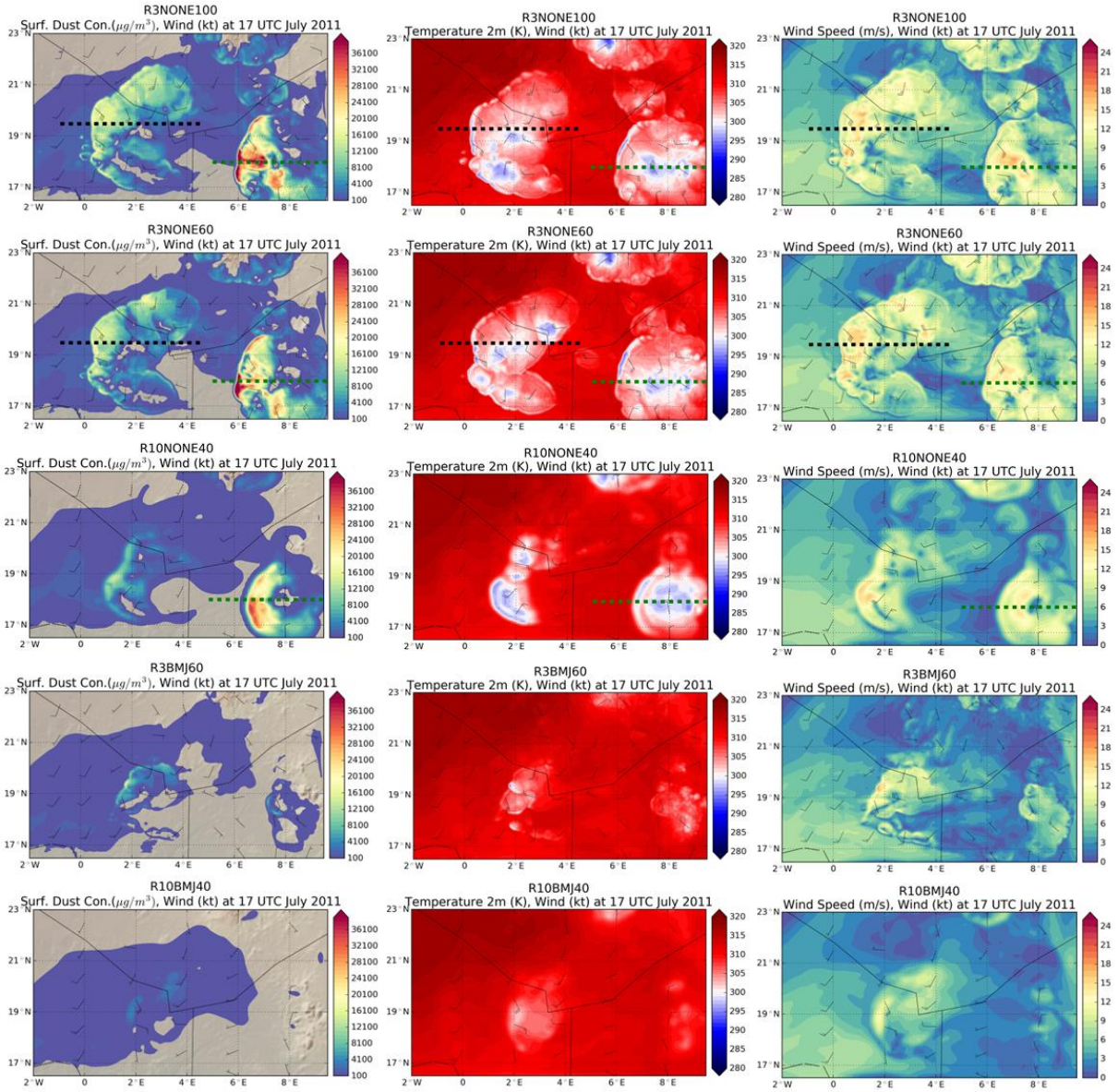

Figure 5.6: *Same as Figure 5.5 but at 17 UTC. The pointed lines at 18ºN (from 5ºE to 9.5ºE) in R3NONE100, R3NONE60 and R10NONE40 and at 19.5ºN (from 1ºW to 4.5ºE) in R3NONE100 and R3NONE60 mark where the vertical cross sections are made in Figure 5.7 and Figure 5.10, respectively.*

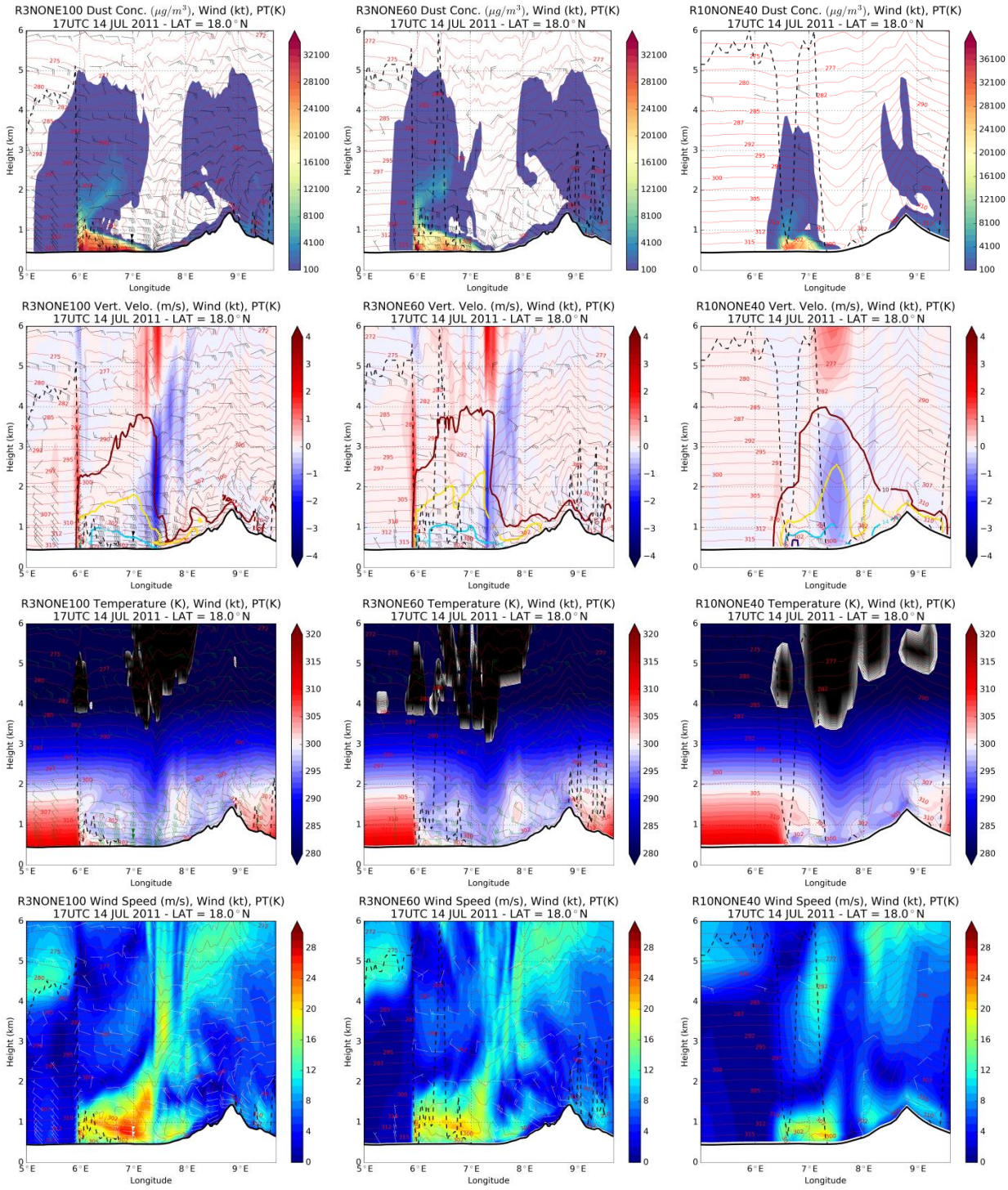

Figure 5.7: *Vertical cross sections (up to 6 km in height) of dust concentration (µg/m^3) (1st row), vertical wind speed (m/s) and specific humidity (bold contour lines) (2nd row), temperature (K) and clouds (black shaded) (3rd row), and horizontal wind speed (m/s) (4th row) at 18ºN, from 5ºE to 9.5º E in longitude (Northwestern Niger; see Figure 5.5), in R3NONE100 (left panels), R3NONE60 (middle panels) and R10NONE40 (right panels) at 17 UTC. All panels include horizontal winds (barbs), potential temperature (PT (K); red contour lines) and the planetary boundary layer (dashed black lines).*

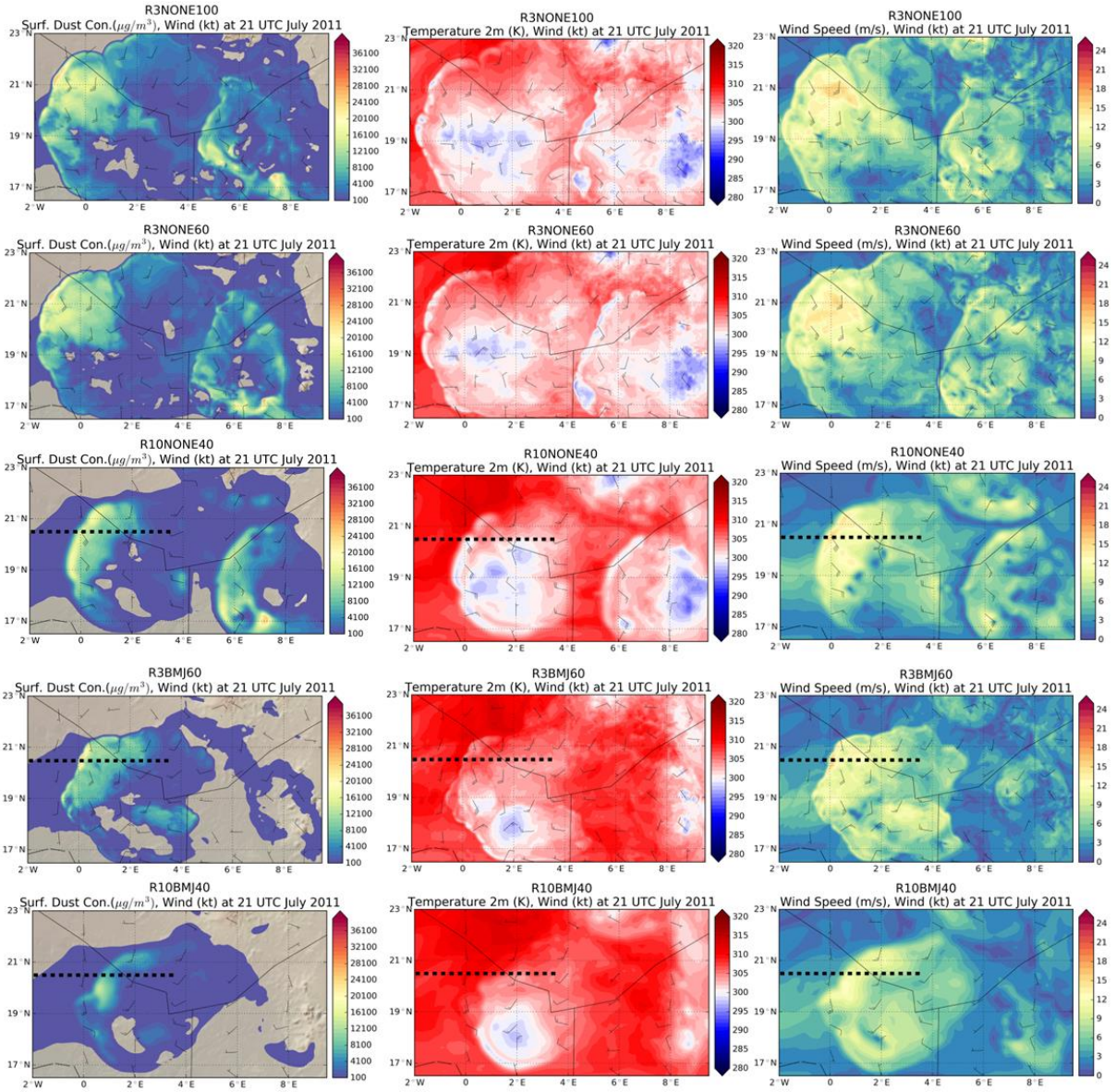

Figure 5.8*: Same as Figure 5.5 but at 21 UTC. The dashed lines in R10NONE40, R3BMJ60 and R10BMJ40 at 20.5ºN (from 2ºW to 3.5ºE) mark where the vertical cross sections are made in Figure 5.11.*

5.4.2 Convective event in Northeastern Mali

In Northeastern Mali (DOM2 in Figure 5.3), dust emissions caused by intense cold pool outflows from a thunderstorm appear in the five model configurations. Both explicit R3NONE100 and R3NONE60 provide daily emitted dust masses of 3.82 and 3.42 Tg, respectively, with similar spatial extension and maximum daily emission peaks of 20-35 g/m^2, although larger areas with these emission peaks appear in R3NONE100. Both R10NONE40 and R3BMJ60 show similar emission features covering approximately the same area with daily emitted dust masses of 2.16 and 2.14 Tg, respectively, and daily dust emission peaks of 15-25 g/m^2. R10BMJ40 is the weakest configuration to uplift dust, producing a daily emitted dust mass of 1.45 Tg and daily emission areas lower than 15 g/m^2.

Before 6 UTC, the meteorological situation in DOM 2 is dominated by weak winds of ~3-3.5 m/s (on average) that intensify from 6 to 9-10 UTC up to ~6.5 m/s (on average) by the breakdown of the NLLJ (Figure 5.9a) with similar behavior in all configurations. The morning winds lead to an hourly peak of dust emitted mass in all configurations, with values from 0.18 to 25 Tg at 10 UTC, in which higher values correspond to higher spatial configurations (see Figure 5.9b). During the morning, all configurations develop a thunderstorm, which reaches its mature stage from 7 to 13-14 UTC favored by a sharp temperature increase (see Figure 5.9e) and the increase of the atmospheric instability (CAPE) (Figure 5.9c).

In parameterized runs (i.e. R3BMJ60 and R10BMJ40), the CAPE increases up to 11 UTC when it drops by the rearrangement of temperature and moisture profiles produced by the BMJ scheme (Figure 5.9b). This results in an early initialization of precipitation (Figure 5.9d), with daily accumulated values over the domain of 1090 mm for R10BMJ40 and 1043 mm for R3BMJ60. Based on this result, the BMJ convection scheme tends to be more effective at removing the instability (i.e. reducing the CAPE) in intense and short-term local episodes, such as in the convective event in Northwestern Niger, (described in Section 5.4.1. R3BMJ60 shows similar behaviors in downdrafts and updrafts with values between 1-2 m/s from 14 to 21 UTC; meanwhile, R10BMJ40 weakly develops vertical velocities during the whole event with updrafts lower than 0.5 m/s and downdrafts lower than 1 m/s.

In explicit runs (i.e. R3NONE100, R3NONE60 and R10NONE40), the CAPE progressively increases during the morning up to 13 UTC. As a consequence of the cold pool outflows and the thunderstorm, rainfall is produced by the three explicit configurations (Figure 5.9d), with daily accumulated values of 370 mm for R3NONE100, 321 mm for R3NONE60 and 190 mm for R10NONE40. Regarding vertical velocities (Figure 5.9f), maximum downdrafts appear at 14 UTC, with 4.8 m/s for R3NONE100 and 4 m/s for R3NONE60; meanwhile, the maximum updrafts appear between 15 and 19 UTC with values of 2.5-3 m/s. R10NONE40 shows a similar behavior in timing and strength of downdrafts, with values between 1-2 m/s, to R3BMJ60, but in its maximum updrafts weaker resolved than R3BMJ60.

All configurations develop cold pool outflows from the mature convective storm as indicated by a drop in the near-surface air temperature (Figure 5.9e). The occurrence of cold pool outflows since 12-13 UTC lead to increase the wind intensity (Figure 5.9a) and emitted dust masses (Figure 5.9b) in R3NONE100 and R3NONE60: up to 0.30 Tg at 16 UTC in R3NONE100, 0.25 Tg at 18 UTC in R3NONE60 as well as 0.28 Tg in R3NONE100 and 0.26 Tg in R3NONE60 at 21 UTC, with mean surface wind speeds ranging from 5.3 to 6.2 m/s (since 13 UTC). Otherwise, the rest of the configurations also develop the large cold pool outflow but later than in both R3NONE100 and R3NONE60: at 15 UTC in R10NONE40, at 16 UTC in R3BMJ60 and at 17-18 UTC in R10BMJ40. Since then, dust emissions increase until 21 UTC in R10NONE40 (0.16 Tg) and R10BMJ40 (0.07 Tg), and until 23 UTC in R3BMJ60 (0.20 Tg), as shown in Figure 5.9b. These dust emissions are driven by an increase in surface wind speeds (on average; Figure 5.9a) that range between 4.6 and 5.2 m/s in R10NONE40, from 4.2 to 6 m/s in R3BMJ60, and from 4 to 5 m/s in R10BMJ40.

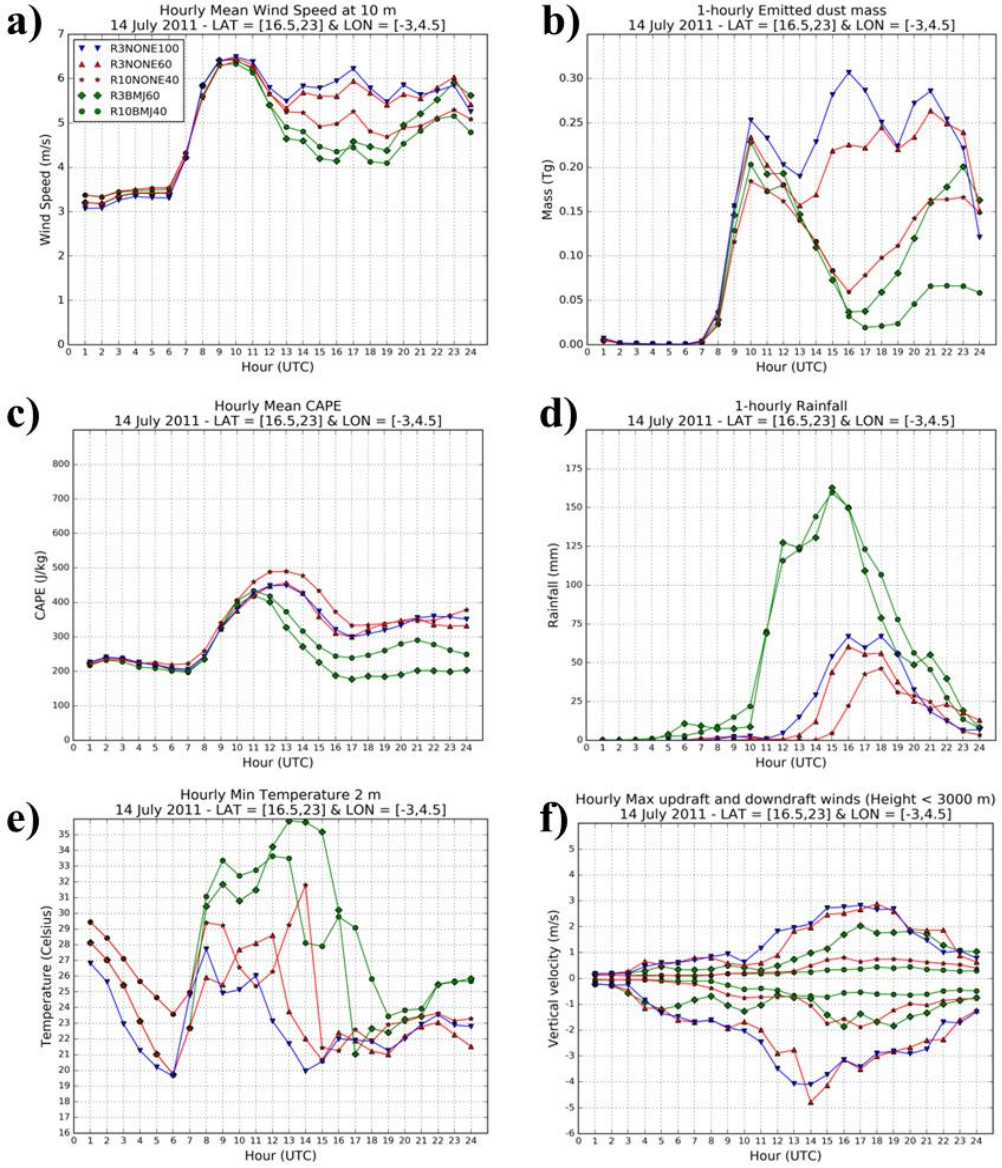

Figure 5.9*: Same as Figure 5.4 but in Northeastern Mali (DOM2; see Figure 5.3).*

Based on surface field maps of dust concentrations, temperatures and wind speeds at 17 UTC (Figure 5.6), all configurations develop cold pool outflows, with associated low temperatures of about 20ºC in explicit runs (i.e. R3NONE100, R3NONE60 and R10NONE40) and about 25ºC in parameterized runs (i.e. R3BMJ60 and R10BMJ40). These cold pools lead to develop gravity currents, with high surface wind speeds of 14-19 m/s in both R3NONE100 and R3NONE60, 14-18 m/s in both R10NONE40 and R3BMJ60 and 8-13 m/s in R10BMJ40, which give rise to generate a haboob (moving west in the shape of an arc), with surface dust concentrations of 20.000-25.000 $\mu g/m^3$ in both R3NONE100 and R3NONE60, 10.000-15.000 $\mu g/m^3$ in both R10NONE40 and R3BMJ60 and less than 10.000 $\mu g/m^3$ in R10BMJ40. Model configurations also differ in the position of their main dust front line, which represents more advancement to the west-northwest and spreads dust over a wider area at higher spatial resolutions for explicit runs, followed by parameterized runs. At 17 UTC, parameterized runs show an early stage in the formation of the haboob and they involved processes. On the other hand, at 21 UTC, R10NONE40, R3BMJ60 and R10BMJ40 show a better development of these haboob processes. These three configuration reproduce an intense cold pool outflow (low temperature values of about 23ºC in the center of the downdraft area), wind speeds of 14-17 m/s in both R10NONE40 and R3BMJ60 and 8-13 m/s in R10BMJ40, and dust concentrations of 20.000-25.000 $\mu g/m^3$ in both R10NONE40 and R3BMJ60 and 7.000-12.000 $\mu g/m^3$ in R10BMJ40.

Vertical cross sections at 19.5ºN in Northeastern Mali for both R3NONE100 and R3NONE60 at 17 UTC (Figure 5.10) show well-developed haboobs with similar features. Both R3NONE100 and R3NONE60 develop similar maximum vertical velocities in downdrafts of about 3 m/s and in updrafts of about 2 m/s. In terms of horizontal wind speed, both R3NONE60 and R3NONE100 show maximum values of 21-26 m/s at 200-500 m in height. Dust concentrations for both R3NONE100 and R3NONE60 are less than 25.000 $\mu g/m^3$ in the haboob's dust body (up to 500 m in height) and 20.000-28.000 $\mu g/m^3$ on the leading edge (up to 1.5 km in height), which decrease progressively with altitude. The whole dust event is long-lived ~11-12 h and spreads over 400-500 km for both R3NONE100 and R3NONE60, as shown in Figure 5.8.

Focusing on the rest of the model configurations (i.e. R10NONE40, R3BMJ60 and R10BMJ40) at 21 UTC, their haboob processes are also identified vertically (Figure 5.11). Both R10NONE40 and R3BMJ60 can develop similar maximum downdrafts of up to 2 m/s, but they differ representing the maximum updrafts, which tend to be higher in R3BMJ60, whit maximum values of 2 m/s, than in R10NONE40, with values lower than 1 m/s. These stronger updrafts in R3BMJ60 are found on the haboob's leading edge where the "wall of blowing dust" develops. R10BMJ60 weakly develops vertical velocities with values that are always lower than 1 m/s. In terms of horizontal wind speed, both R10NONE40 and R3BMJ60 show maximum horizontal wind speeds of 23-28 m/s at around 500 m (on the leading edge); meanwhile, R10NONE40 shows maximum horizontal wind speeds of ~18 m/s at 200-300 m. Dust concentrations are lower than 25.000 $\mu g/m^3$ in the haboob's dust body (up to

500 m in height) in both R10NONE40 and R3BMJ60, although higher values are found up to 28.000 µg/m^3 in R3BMJ60 on the leading edge (up to 1.5 km). R10BMJ40 provides maximum dust concentrations lower than 12.000 µg/m^3 with a low vertical development up to 1 km. The whole dust event spreads over 250-300 km in both R10NONE40 and R3BMJ60 and 200-250 km in R10BMJ40, and dust propagations lasted ~10 h in both R3NONE100 and R3NONE60 and ~8 h in R10BMJ40.

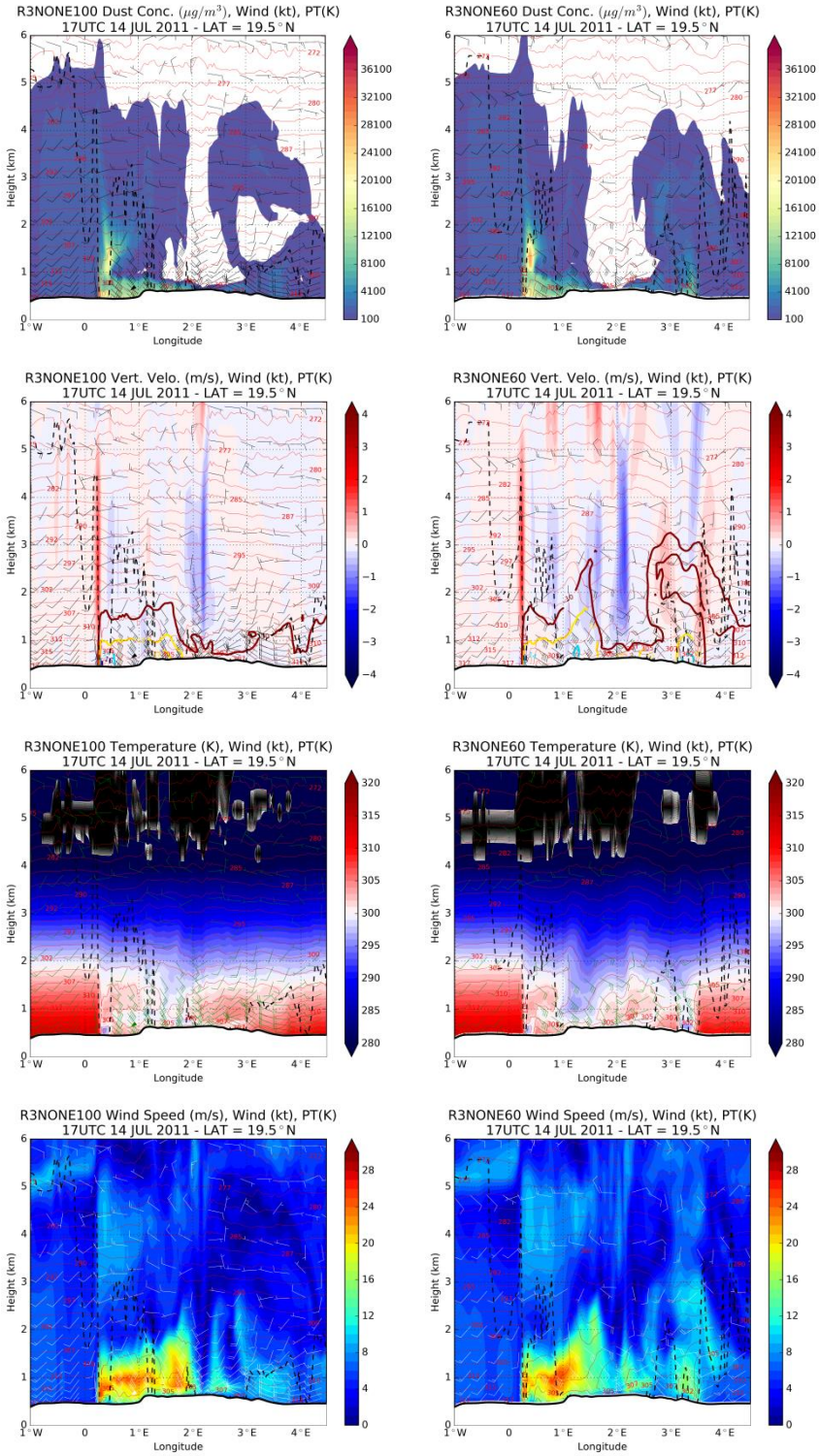

Figure 5.10: *Same as Figure 5.7 but at 19.5ºN and from 1ºW to 4.5ºE (Northeastern Mali; see Figure 5.6) in both R3NONE100 (left panels) and R3NONE60 (right panels).*

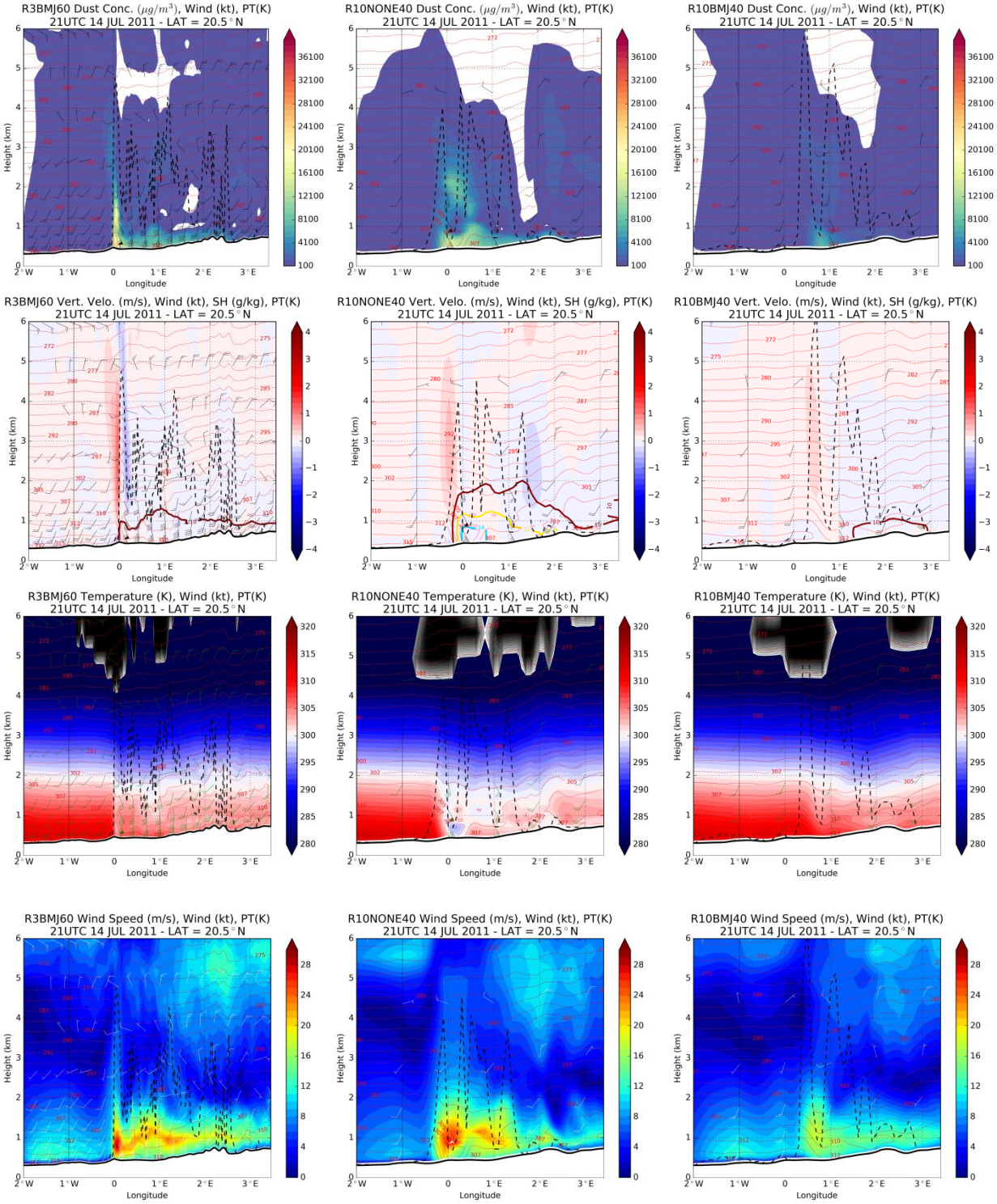

Figure 5.11*: Same as Figure 5.7 but at 21 UTC at 20.5ºN and from 2ºW to 3.5ºE (Northeastern Mali; see Figure 5.8) in R3BMJ60 (left panels), R10NONE40 (middle panels), R10BMJ40 (right panels).*

5.5 Conclusions

The present chapter investigates the model's ability to reproduce haboobs and the meteorological processes they involve. For that purpose, five NMMB/BSC-Dust model runs for both explicit and parameterized convection as well as different (horizontal and vertical) spatial resolutions are tested under a convective situation over Southern Algeria, Northeastern Mali, and Northwestern Niger on 14 July 2011. During this day, a sharp wind speed increase occurs from 6 to 9-10 UTC that is associated with the breakdown of the NLLJ, which all model configurations simulate similarly. After 11 UTC, convective dust storms developed differently depending on the model configuration. The main differences between experiments appear over the haboobs simulated in Northwestern Niger and Northeastern Mali because the genesis of the convective systems developed. In Northwestern Niger, an isolated thunderstorm is originated by orographic convection over the local steep topography. Otherwise, in Northeastern Mali, the storm cell is developed over low topography as a result of intense surface heating, monsoon moist flow, and large-scale lifting by the low-pressure system.

Based on two simulated haboobs in Northwestern Niger and Northeastern Mali, the main processes in haboob formation are moist convection, cold pool outflows, and density currents, which are well-developed in explicit runs, although they intensify and occur earlier at higher spatial resolution. Parameterized runs are more effective at removing vertical instability under orographic convection events, which lead those parameterized runs to practically omit the dust event in Northeastern Niger. Otherwise, comparing explicit and parameterized runs with the same horizontal resolution, we find weaker vertical velocities, later downdrafts, and earlier rainfall initialization, larger spatially distributed precipitation and more than double of rainfall are produced in parameterized runs by removing atmospheric instability.

Explicit runs developed the main meteorological processes associated with haboobs, although the modeling experiments at 0.10ºx0.10º horizontal resolutions are insufficient to properly develop the intense updrafts and vertical dust distribution found on the haboob's leading edge. Increasing vertical layers from 60 to 100 layers in explicit runs at 0.03ºx0.03º horizontal resolutions intensifies convective processes because the model captures more intense transfer of heat near-surface. These results also show that the most important contribution to developing intense convective processes is found in the model horizontal resolution.

For explicit runs at 0.03ºx0.03º horizontal resolution, the resulting simulated haboobs in Northwestern Niger had a duration of ~10 h and associated the main structure of dust of 500 m in height and 100-150 km in extension and maximum surface concentrations between 40.000-50.000 $\mu g/m^3$. Otherwise, in Northeastern Mali, the simulated haboobs for explicit runs at 0.03ºx0.03º horizontal resolution have lifetimes of ~11-12 h and are associated with the main structure of dust of 500 m in height and 400-500 km in extension and maximum surface concentrations of 20.000-28.000 $\mu g/m^3$. Based on previous

studies (i.e. Vukovic et al., 2014; Mamouri et al., 2016; Crouvi et al., 2017), dust concentrations under the presence of a haboob vary from the order of a thousand to a few thousand μg/m^3, although these dust concentrations depend on the region. In some haboob studies, maximum values of PM10 monitored 9.000 μg/m^3 in Phoenix (Vukovic et al., 2014), 1.000–1.500 μg/m^3 in Israel (Crouvi et al., 2017), and 8.000-10.000 μg/m^3 in the Eastern Mediterranean (Mamouri et al., 2016). Although those values are from other events and areas, it indicates that simulated dust concentrations by the NMMB/BSC-Dust model, at explicit runs for both convective events, are possibly higher than the real values.

It is not always straightforward to assume those explicit runs at high resolutions result in improving model results in all convective situations due to the chaotic nature of their associated small-scale phenomena. However, taking into account the present results, further experiments should be conducted to better identify the optimal configuration for reproducing haboob episodes based on quantitative observational data.

Chapter 6

6 Conclusions and future work

Focusing on the description of the dust cycle, one of the most critical challenges is the clarification of the role of smaller-scale meteorological processes on dust emission and their contributions to the global budget. The work presented in this Ph.D. thesis reveals some of the benefits of using a non-hydrostatic multiscale model, the NMMB/BSC-Dust model, to reproduce the physical processes associated with the dust cycle at meteorological scales ranging from sub-synoptic to mesoscale (from 100 up to 3 km spatial resolution) over Northern Africa, the Middle East and Europe (NAMEE). The model behavior at different scales is key to better understand the meteorological processes associated with the dust life cycle and consequently their impacts. The main findings of this Ph.D. thesis are summarized in Section 6.1, while Section 6.2 proposes some recommendations for future tasks raised from the present research.

6.1 Main conclusions

In order to reach the general objective of this Ph.D. thesis, three specific modeling experiments (presented in Chapters 3, 4 and 5) have been performed to assess the skills of a state-of-the-art model to resolve those processes associated with the mineral dust life cycle under a wide range of spatial and meteorological scales. The first experiment analyzes the spatiotemporal scales associated with the dust cycle and demonstrates the model's consistency through a range of spatial scales. The second experiment addresses how the model reproduces the topographic effects on the dust transport of two synoptic dust storms at regional scales with increasing resolution. Finally, the third experiment investigates the model's ability to resolve convective dust storms and the role of convective parameterization in an online dust model.

In Chapter 3, a set of three simulations (that cover global to regional scales, ~100 to 10 km) is analyzed to demonstrate the consistency of the model and discuss the spatiotemporal variability of dust and its meteorological processes. The analysis is done for an entire annual cycle, the year 2011, over NAMEE. The dust cycle and its associated large-scale processes can be represented by the spatial distribution of dust that is in agreement with observations, which demonstrates that the seasonality of dust distributions are well-reproduced by both global and regional scales over the study domain. Regional simulations (~10–30 km) present a more accurate representation of the spatiotemporal variability of dust fields with a better simulation of smaller scale meteorological processes associated with topography and low-level jets (LLJs). However, no significant improvements are observed in the model performance between coarse and fine regional runs in terms of dust concentrations. This is partly linked to the fact that both regional model configurations use the same desert dust source mask, which includes a topographical mask at 0.25º horizontal resolution. Systematic underestimation of strong dust events in the Middle East and during the wet season in the Sahel are associated with

convective storms (i.e. haboobs) that the model is not able to reproduce in the analyzed resolutions. The analysis demonstrates the model's consistency along global and regional scales. This is a fundamental feature that supports the feasibility of future dust/aerosol nesting implementations in the model.

Chapter 4 studies the model's ability to reproduce topographic effects and estimates their impacts on dust transport over complex terrains such as the Middle East. The analysis is based on two runs, one with a high horizontal resolution of 0.03º (~3 km) and another with a coarser horizontal resolution of 0.33º (~30 km). Both model experiments cover two intense dust storms that occurred on 17–20 March 2012 as a consequence of strong northwesterly Shamal winds that spanned thousands of kilometers in the Middle East. The comparison with ground-based (surface weather stations and AERONET sun-photometers) and satellite aerosol observations (Aqua/MODIS and MSG/SEVIRI) shows that despite differences in the magnitude of the simulated dust concentrations, the model is able to reproduce these two dust outbreaks. Differences between both simulations on the dust spread rise on regional dust transport areas in Southwestern Saudi Arabia, Yemen, and Oman. The complex orography there (with peaks higher than 3000 m) has an impact on the transported dust concentration fields over mountain regions. Differences between both model configurations are mainly associated with the channelization of the dust flow through valleys and the differences in the modeled altitude of the mountains that alters the meteorology and blocks the dust fronts limiting the transport of dust. These results demonstrate how the dust prediction in the vicinity of complex terrains improves using high horizontal resolution simulations.

Chapter 5 focuses on the model's ability to reproduce convective dust storms (haboobs) and their involved meteorological processes. For that purpose, model runs at high spatial resolutions are performed using explicit and parameterized convection. The analysis includes five numerical experiments, which are applied for a case study in mid-July 2011 over a small domain in Western Africa. Using parameterized convection in the NMMB/BSC-Dust model reduces or even inhibits the formation of haboob processes, which are practically omitted at coarser grid spacing (~10 km horizontal resolution). The model successfully simulates haboobs and their meteorological processes (e.g. moist convection, cold pool outflows, and gravity currents) at explicit convection configurations, although it requires high spatial resolution (< 4 km horizontal resolution) to properly develop the timing and strength of those involved meteorological processes.

6.2 Recommendations for future research

In the last years, the interest in the study of atmospheric dust at the global and regional scales has increased significantly. In this last section, some future challenges of dust modeling related to the main results of the present research work are highlighted.

Exploring the impact of soil moisture on dust simulations. Soil moisture is a key variable in model runs because it strongly controls the surface fluxes and this affects the near-surface meteorology. Furthermore, soil moisture significantly affects dust emissions (i.e. Fécan et al. 1999). Thus, proper model initialization of soil moisture is critical for modeling dust emissions. Nowadays, dust models tend to use soil moisture data from (re)analysis and even from model outputs from a spinup simulation (over short or long periods). However, these datasets are possibly not representing accurate soil moisture fields at a local scale. Some recent studies (Rüdiger et al., 2014; Kim et al., 2017) present new observational databases based on passive sensors as Soil Moisture and Ocean Salinity (SMOS; Lacava et al. 2012). Rüdiger et al. (2014) show that SMOS soil moisture exhibits better performance than other datasets, such as from reanalysis of the Global Land Data Assimilation System and satellite data of AMSR2.

Using nesting capabilities in dust simulations. Nowadays, some non-hydrostatic models, such as the multi-scale ICON-ART (Rieger et al., 2015) and the regional WRF-Chem (Chapman et al., 2009), include nesting capabilities for multiple parent/children domain interactions in order to progressively increase the horizontal resolution from the outermost domain (with the coarsest horizontal resolution) to the innermost domain (with higher horizontal resolution which can permit convection to explicitly resolve, for example). In recent studies, two-way nest domains (with the innermost domain running with a horizontal resolution of ~2 km) have been used for reproducing haboob dust storms (Kalenderski and Stenchikov, 2016; Gasch et al., 2017; Solomos et al., 2017). These studies were able to reproduce the key processes of specific haboobs (e.g. updrafts, downdrafts and gravity currents), which were not properly reproduced at coarser resolutions. The presented research work demonstrates the consistency of the NMMB-MONARCHv1.0 model results along of a range of spatiotemporal scales. The nesting implementation for aerosols (and particularly for mineral dust) in the model can help to perform high-resolution simulations in specific areas with a minimum requirement of computational resources. This will improve the model results in specific regions for forecasting applications and provide a unique framework to better understand the contribution of the different types of sand and dust storms at regional and global scales.

Implementation of a cold pool parameterization for convective dust storms. Haboobs are omitted in dust forecasts because most of the models neither explicitly resolve nor parameterize them. Simulations with explicit convection (switching off the convection scheme) require high-resolution configurations (below 4 km of grid spacing) that result in highly demanding computational resources particularly for operational forecasting. The main goal of the ERC project Desert Storms (led by Peter Knippertz, KIT/Leed University) was to better understand weather processes related to the emission of mineral dust over West Africa. The different works developed in the framework of this European project included an ideal set of simulations for developing an offline parameterization of convective

dust storms designed for large-scale models. As a result, a new parameterization of near-surface wind gusts and dust emissions generated by cold pools, based on the downdraft mass flux from the convection scheme, was proposed by Pantillon et al. (2015). This new parameterization can be tested in the NMMB-MONARCHv1.0 for coarser model runs (horizontal resolution larger than 10 km) to include the contribution of sand and dust storms associated with convective processes.

Implementation of ensemble modeling techniques in dust forecasts. There are still some limitations in the simulation of the spatiotemporal location and propagation of some sand and dust storms. Convection (one of the mechanisms associated with the strongest sand and dust storms, i.e. haboobs) has a chaotic nature that negatively affects its predictability. In this sense, simulations are very sensitive to the meteorological initial conditions used for the model runs. To overcome this random nature of these events and to improve their predictability, the ensemble forecasts appear to be a potential technique for dust forecasting. Multi-model ensembles (like those produced in ICAP and SDS-WAS) also represent a paradigmatic shift in which offering the best product to the users as a collective scientific community becomes more important than competing to achieve the best forecast as individual centers. This new paradigm fosters collaboration and interaction and, ultimately, results in improvements in the individual models and better final products.

Chapter 7

7 References

Akata, N., Hasegawa, H., Kawabata, H., Chikuchi, Y., Sato, T., Ohtsuka, Y., Kondo, K. and Hisamatsu, S. (2007) 'Deposition of 137Cs in Rokkasho, Japan and its relation to Asian dust', *Journal of Environmental Radioactivity*, 95(1), pp. 1–9.

Al-Yahyai, S. and Charabi, Y. (2014) 'Trajectory Calculation as Forecasting Support Tool for Dust Storms', *Advances in Meteorology*, Vol. 2014(Article ID 698359), pp. 1–6.

Alizadeh-Choobari, O., Zawar-Reza, P. and Sturman, A. (2014) 'The "wind of 120days" and dust storm activity over the Sistan Basin', *Atmospheric Research*, 143, pp. 328–341.

Allen, C. J. T., Washington, R. and Engelstaedter, S. (2013) 'Dust emission and transport mechanisms in the central Sahara: Fennec ground-based observations from Bordj Badji Mokhtar, June 2011', *Journal of Geophysical Research Atmospheres*, 118(12), pp. 6212–6232.

Anderson, J. R., Hardy, E. E., Roach, J. T. and Witmer, R. E. (1976) *A land use and land cover classification system for use with remote sensor data, USGS Professional Paper 964. A revision of the land use classification system as presented in the USGS Circular 671*.

Arakawa, A. and Lamb, V. R. (1977) 'Computational design of the basic dynamical processes of the UCLA general circulation model', *General Circulation Models of the Atmosphere, Methods in Computational Physics*. Edited by J. Chang. Academic Press, 17, pp. 173–265.

Ashpole, I. and Washington, R. (2013) 'Intraseasonal variability and atmospheric controls on daily dust occurrence frequency over the central and western Sahara during the boreal summer', *Journal of Geophysical Research: Atmospheres*, 118(23), pp. 12915–12926.

Badia, A. and Jorba, O. (2015) 'Gas-phase evaluation of the online NMMB/BSC-CTM model over Europe for 2010 in the framework of the AQMEII-Phase2 project', *Atmospheric Environment*, 115, pp. 657–669.

Badia, A., Jorba, O., Voulgarakis, A., Dabdub, D., Pérez García-Pando, C., Hilboll, A., Gonçalves, M. and Janjic, Z. (2016) 'Gas-phase chemistry in the online multiscale NMMB/BSC Chemical Transport Model: Description and evaluation at global scale', *Geoscientific Model Development Discussions*, (2), pp. 1–47.

Badia, A., Jorba, O., Voulgarakis, A., Dabdub, D., Pérez García-Pando, C., Hilboll, A., Gonçalves, M. and Janjic, Z. (2017) 'Description and evaluation of the Multiscale Online Nonhydrostatic AtmospheRe CHemistry model (NMMB-MONARCH) version 1.0: gas-phase chemistry at global scale', *Geoscientific Model Development*, 10(2), pp. 609–638.

Bagnold, R. A. (1941) *The physics of blown sand and desert dunes*. Methuen, London.

Barkan, J., Kutiel, H., Alpert, P. and Kishcha, P. (2004) 'Synoptics of dust intrusion days from the African continent into the Atlantic Ocean', *Journal of Geophysical Research*, 109(D08201), pp. 1–9.

Barnaba, F., Bolignano, A., Di Liberto, L., Morelli, M., Lucarelli, F., Nava, S., Perrino, C., Canepari, S., Basart, S., Costabile, F., Dionisi, D., Ciampichetti, S., Sozzi, R. and Gobbi, G. P. (2017) 'Desert dust contribution to PM10 loads in Italy: Methods and recommendations addressing the relevant European Commission Guidelines in support to the Air Quality Directive 2008/50', *Atmospheric Environment*, 161, pp. 288–305.

Basart, S., Pay, M. T., Jorba, O., Pérez, C., Jiḿnez-Guerrero, P., Schulz, M. and Baldasano, J. M. (2012) 'Aerosols in the CALIOPE air quality modelling system: Evaluation and analysis of PM levels, optical depths and chemical composition over Europe', *Atmospheric Chemistry and Physics*, 12(7), pp. 3363–3392.

Basart, S., Pérez, C., Cuevas, E., Baldasano, J. M. and Gobbi, G. P. (2009) 'Aerosol characterization in Northern Africa, Northeastern Atlantic , Mediterranean Basin and Middle East from direct-sun AERONET observations', *Middle East*, 9(21), pp. 8265–8282.

Betts, A. K. (1986) ‘A new convective adjustment scheme. Part I: Observational and theoretical basis’, *Quarterly Journal of the Royal Meteorological Society*, 112(473), pp. 677–691.

Betts, A. K. and Miller, M. J. (1986) ‘A new convective adjustment scheme. Part II: Single column tests using GATE wave, BOMEX, ATEX and arctic air-mass data sets’, *Quarterly Journal of the Royal Meteorological Society*, 112(473), pp. 693–709.

Bou Karam, D., Flamant, C., Knippertz, P., Reitebuch, O., Pelon, J., Chong, M. and Dabas, A. (2008) ‘Dust emissions over the Sahel associated with the West African monsoon intertropical discontinuity region: A representative case-study’, *Quarterly Journal of the Royal Meteorological Society*. John Wiley & Sons, Ltd., 134(632), pp. 621–634.

Bretl, S., Reutter, P., Raible, C. C., Ferrachat, S., Poberaj, C. S., Revell, L. E. and Lohmann, U. (2015) ‘The influence of absorbed solar radiation by Saharan dust on hurricane genesis’, *Journal of Geophysical Research Atmospheres*, 120(5), pp. 1902–1917.

Bristow, C. S., Hudson-Edwards, K. A. and Chappell, A. (2010) ‘Fertilizing the Amazon and equatorial Atlantic with West African dust’, *Geophysical Research Letters*, 37(14), pp. 3–7.

Cakmur, R. V., Miller, R. L., Perlwitz, J., Geogdzhayev, I. V., Ginoux, P., Koch, D., Kohfeld, K. E., Tegen, I. and Zender, C. S. (2006) ‘Constraining the magnitude of the global dust cycle by minimizing the difference between a model and observations’, *Journal of Geophysical Research Atmospheres*, 111(6), pp. 1–24.

Carrico, C. M., Bergin, M. H., Shrestha, A. B., Dibb, J. E., Gomes, L. and Harris, J. M. (2003) ‘The importance of carbon and mineral dust to seasonal aerosol properties in the Nepal Himalaya’, *Atmospheric Environment*, 37(20), pp. 2811–2824.

Chapman, E. G., Gustafson, W. I., Easter, R. C., Barnard, J. C., Ghan, S. J., Pekour, M. S. and Fast, J. D. (2009) ‘Coupling aerosol-cloud-radiative processes in the WRF-Chem model: investigating the radiative impact of elevated point sources’, *Atmospheric Chemistry and Physics Discussions*, 8(4), pp. 14765–14817.

Chiapello, I., Moulin, C. and Prospero, J. M. (2005) ‘Understanding the long-term variability of African dust transport across the Atlantic as recorded in both Barbados surface concentrations and large-scale Total Ozone Mapping Spectrometer (TOMS) optical thickness’, *Journal of Geophysical Research D: Atmospheres*, 110(18), pp. 1–9.

Chien, L.-C., Lien, Y.-J., Yang, C.-H. and Yu, H.-L. (2014) ‘Acute Increase of Children’s Conjunctivitis Clinic Visits by Asian Dust Storms Exposure - A Spatiotemporal Study in Taipei, Taiwan’, *PLOS ONE*. Public Library of Science, 9(10), pp. 1–10.

Creamean, J. M., Suski, K. J., Rosenfeld, D., Cazorla, A., DeMott, P. J., Sullivan, R. C., White, A. B., Ralph, F. M., Minnis, P., Comstock, J. M., Tomlinson, J. M. and Prather, K. A. (2013) ‘Dust and Biological Aerosols from the Sahara and Asia Influence Precipitation in the Western U.S.’, *Science*, 339(6127), p. 1572 LP-1578.

Crouvi, O., Dayan, U., Amit, R. and Enzel, Y. (2017) ‘An Israeli haboob: Sea breeze activating local anthropogenic dust sources in the Negev loess’, *Aeolian Research*, 24, pp. 39–52.

Cuesta, J., Lavaysse, C., Flamant, C., Mimouni, M. and Knippertz, P. (2010) ‘Northward bursts of the West African monsoon leading to rainfall over the Hoggar Massif, Algeria’, *Quarterly Journal of the Royal Meteorological Society*, 136(SUPPL. 1), pp. 174–189.

Cuevas, E. (2013) ‘Establishing a WMO Sand and Dust Storm Warning Advisory and Assessment System Regional Node for West Asia: Current Capabilities and Needs’, *Publications Board World Meteorological Organization (WMO)*, WM0-1121.

Cuevas, E., Camino, C., Benedetti, A., Basart, S., Terradellas, E., Baldasano, J. M., Morcrette, J. J., Marticorena, B., Goloub, P., Mortier, A., Berjón, A., Hernández, Y., Gil-Ojeda, M. and Schulz, M. (2015) ‘The MACC-II 2007-2008 reanalysis: atmospheric dust evaluation and characterization over northern Africa and the Middle East’, *Atmospheric Chemistry and Physics*, 15(8), pp. 3991–4024.

Cziczo, D. J., Froyd, K. D., Hoose, C., Jensen, E. J., Diao, M., Zondlo, M. a, Smith, J. B., Twohy, C. H. and Murphy, D. M. (2013) 'Clarifying the Dominant Sources and Mechanisms of Cirrus Cloud Formation.', *Science (New York, N.Y.)*, 1320(May), pp. 1–8.

d'Almeida, G. A. (1987) 'On the variability of desert aerosol radiative characteristics', *Journal of Geophysical Research*, 92(D3), p. 3017.

Dee, D. P., Uppala, S. M., Simmons, A. J., Berrisford, P., Poli, P., Kobayashi, S., Andrae, U., Balmaseda, M. A., Balsamo, G., Bauer, P., Bechtold, P., Beljaars, A. C. M., van de Berg, L., Bidlot, J., Bormann, N., Delsol, C., Dragani, R., Fuentes, M., Geer, A. J., Haimberger, L., Healy, S. B., Hersbach, H., Hólm, E. V., Isaksen, L., Kallberg, P., Köhler, M., Matricardi, M., Mcnally, A. P., Monge-Sanz, B. M., Morcrette, J. J., Park, B. K., Peubey, C., de Rosnay, P., Tavolato, C., Thépaut, J. N. and Vitart, F. (2011) 'The ERA-Interim reanalysis: Configuration and performance of the data assimilation system', *Quarterly Journal of the Royal Meteorological Society*, 137(656), pp. 553–597.

DeFlorio, M. J., Goodwin, I. D., Cayan, D. R., Miller, A. J., Ghan, S. J., Pierce, D. W., Russell, L. M. and Singh, B. (2016) 'Interannual modulation of subtropical Atlantic boreal summer dust variability by ENSO', *Climate Dynamics*, 46(1), pp. 585–599.

Dirmeyer, P. A., Cash, B. A., Kinter, J. L., Jung, T., Marx, L., Satoh, M., Stan, C., Tomita, H., Towers, P., Wedi, N., Achuthavarier, D., Adams, J. M., Altshuler, E. L., Huang, B., Jin, E. K. and Manganello, J. (2012) 'Simulating the diurnal cycle of rainfall in global climate models: Resolution versus parameterization', *Climate Dynamics*, 39(1–2), pp. 399–418.

Dubovik, O., Holben, B., Eck, T. F., Smirnov, A., Kaufman, Y. J., King, M. D., Tanré, D., Slutsker, I., Sciences, G. E. and Directorate, E. S. (2002) 'Variability of Absorption and Optical Properties of Key Aerosol Types Observed in Worldwide Locations', *Journal of the Atmospheric Sciences*, 59(3), pp. 590–608.

Dunion, J. P. and Velden, C. S. (2004) 'The impact of the Saharan Air Layer on Atlantic tropical cyclone activity', *Bulletin of the American Meteorological Society*, 85(3), pp. 353–365.

EC (2008) 'Directive 2008/50/EC of the European Parliament and of the Council of 21 May 2008 on ambient air quality and cleaner air for Europe (OJ L 152, 11.6.2008, p. 1–44) (http://eur-lex.europa.eu/LexUriServ/LexUriServ.do?uri=OJ:L:2008:152:0001:0044:EN:PDF)'.

Ek, M. B., Mitchell, K. E., Lin, Y., Rogers, E., Grunmann, P., Koren, V., Gayno, G. and Tarpley, J. D. (2003) 'Implementation of Noah land surface model advances in the National Centers for Environmental Prediction operational mesoscale Eta model', *Journal of Geophysical Research: Atmospheres*, 108(D22), p. 8851.

Engelstaedter, S., Washington, R., Flamant, C., Parker, D. J., Allen, C. J. T. and Todd, M. C. (2015) 'The Saharan heat low and moisture transport pathways in the central Sahara—Multiaircraft observations and Africa-LAM evaluation', *Journal of Geophysical Research: Atmospheres*, pp. 1–26.

Evan, A. T., Dunion, J., Foley, J. A., Heidinger, A. K. and Velden, C. S. (2006) 'New evidence for a relationship between Atlantic tropical cyclone activity and African dust outbreaks', *Geophysical Research Letters*, 33(19), pp. 1–5.

Evan, A. T., Fiedler, S., Zhao, C., Menut, L., Schepanski, K., Flamant, C. and Doherty, O. (2015) 'Derivation of an observation-based map of North African dust emission', *Aeolian Research*. Elsevier B.V., 16, pp. 153–162.

Evan, A. T., Foltz, G. R., Zhang, D. and Vimont, D. J. (2011) 'Influence of African dust on ocean–atmosphere variability in the tropical Atlantic', *Nature Geoscience*. Nature Publishing Group, 4(11), pp. 762–765.

Fairlie, T. D., Jacob, D. J. and Park, R. J. (2007) 'The impact of transpacific transport of mineral dust in the United States', *Atmospheric Environment*, 41(6), pp. 1251–1266.

Fan, S. M. (2013) 'Modeling of observed mineral dust aerosols in the arctic and the impact on winter season low-level clouds', *Journal of Geophysical Research Atmospheres*, 118(19), pp. 11161–11174.

Farquharson, J. S. (1937) ‘Haboobs and instability in the sudan’, *Quarterly Journal of the Royal Meteorological Society*. John Wiley & Sons, Ltd, 63(271), pp. 393–414.

Fécan, F., Marticorena, B. and Bergametti, G. (1999) ‘Parametrization of the increase of the aeolian erosion threshold wind friction velocity due to soil moisture for arid and semi-arid areas’, *Annales Geophysicae*, 17, pp. 149–157.

Fels, S. B. and Schwarzkopf, M. D. (1975) ‘The Simplified Exchange Approximation: A New Method for Radiatic Transfer Calculations’, *Journal of the Atmospheric Sciences*, pp. 1475–1488.

Ferrier, B. S., Jin, Y., Lin, Y., Black, T., Rogers, E. and DiMego, G. (2002) ‘Implementation of a new grid-scale cloud and precipitation scheme in the NCEP Eta Model’, in *19th Conf. on Weather Analysis and Forecasting/15th Conf. on Numerical Weather Prediction*. San Antonio, TX: Amer. Meteor. Soc., pp. 280–283.

Fiedler, S., Schepanski, K., Heinold, B., Knippertz, P. and Tegen, I. (2013) ‘Climatology of nocturnal low-level jets over North Africa and implications for modeling mineral dust emission’, *Journal of Geophysical Research Atmospheres*, 118(12), pp. 6100–6121.

Foltz, G. R. and McPhaden, M. J. (2008) ‘Trends in Saharan dust and tropical Atlantic climate during 1980-2006’, *Geophysical Research Letters*, 35(20), pp. 1–5.

Gama, C., Tchepel, O., Baldasano, J. M., Basart, S., Ferreira, J., Pio, C., Cardoso, J. and Borrego, C. (2015) ‘Seasonal patterns of Saharan dust over Cape Verde – a combined approach using observations and modelling’, *Tellus B*, 67, pp. 1–21.

Garrison, V. H., Shinn, E. a., Foreman, W. T., Griffin, D. W., Holmes, C. W., Kellogg, C. a., Majewski, M. S., Richardson, L. L., Ritchie, K. B. and Smith, G. W. (2003) ‘African and Asian Dust: From Desert Soils to Coral Reefs’, *BioScience*, 53(5), p. 469.

Gasch, P., Rieger, D., Walter, C., Khain, P., Levi, Y. and Vogel, B. (2017) ‘An analysis of the September 2015 severe dust event in the Eastern Mediterranean’, *Atmospheric Chemistry and Physics Discussions*, (in review), pp. 1–37.

Ginoux, P., Chin, M., Tegen, I., Prospero, J. M., Holben, B., Dubovik, O. and Lin, S.-J. (2001) ‘Sources and distributions of dust aerosols simulated with the GOCART model’, *Journal of Geophysical Research: Atmospheres*, 106(D17), pp. 20255–20273.

Ginoux, P., Prospero, J. M., Gill, T. E., Hsu, N. C. and Zhao, M. (2012) ‘Global-scale attribution of anthropogenic and natural dust sources and their emission rates based on MODIS Deep Blue aerosol products’, *Reviews of Geophysics*, 50(RG3005).

Gkikas, A., Basart, S., Hatzianastassiou, N., Marinou, E., Amiridis, V., Kazadzis, S., Pey, J., Querol, X., Jorba, O., Gassó, S. and Baldasano, J. M. (2016) ‘Mediterranean intense desert dust outbreaks and their vertical structure based on remote sensing data’, *Atmospheric Chemistry and Physics*. Copernicus GmbH, 16(13), pp. 8609–8642.

Gleick, P. H. (2014) ‘Water, Drought, Climate Change, and Conflict in Syria’, *Weather, Climate, and Society*, 6(3), pp. 331–340.

Goudie, A. S. (2014) ‘Desert dust and human health disorders’, *Environment International*, 63, pp. 101–113.

Goudie, A. S. and Middleton, N. J. (2006) *Desert Dust in the Global System*. Berlin: Springer.

Haustein, K. (2011) *Development of an atmospheric modeling system for regional and global mineral dust predictions: Application to Northern Africa, Middle East and Europe*. UPC.

Haustein, K., Pérez, C., Baldasano, J. M., Jorba, O., Basart, S., Miller, R. L., Janjic, Z., Black, T., Nickovic, S., Todd, M. C., Washington, R., Müller, D., Tesche, M., Weinzierl, B., Esselborn, M. and Schladitz, A. (2012) ‘Atmospheric dust modeling from meso to global scales with the online NMMB/BSC-Dust model - Part 2: Experimental campaigns in Northern Africa’, *Atmospheric Chemistry and Physics*, 12(6), pp. 2933–2958.

Haustein, K., Washington, R., King, J., Wiggs, G., Thomas, D. S. G., Eckardt, F. D., Bryant, R. G. and Menut, L. (2015) 'Testing the performance of state-of-the-art dust emission schemes using DO4Models field data', *Geoscientific Model Development*, 8(2), pp. 341–362.

Heinold, B., Knippertz, P., Marsham, J. H., Fiedler, S., Dixon, N. S., Schepanski, K., Laurent, B. and Tegen, I. (2013) 'The role of deep convection and nocturnal low-level jets for dust emission in summertime West Africa: Estimates from convection-permitting simulations', *Journal of Geophysical Research Atmospheres*, 118(10), pp. 4385–4400.

Heymsfield, A. J., Bansemer, A., Heymsfield, G. and Fierro, A. O. (2009) 'Microphysics of Maritime Tropical Convective Updrafts at Temperatures from −20° to −60°', *Journal of the Atmospheric Sciences*, 66(12), pp. 3530–3562.

Holben, B. N., Eck, T. F., Slutsker, I., Tanré, D., Buis, J. P., Setzer, A., Vermote, E., Reagan, J. A., Kaufman, Y. J., Nakajima, T., Lavenu, F., Jankowiak, I. and Smirnov, A. (1998) 'AERONET—A Federated Instrument Network and Data Archive for Aerosol Characterization', *Remote Sensing of Environment*, 66(1), pp. 1–16.

Hong, Y.-C., Pan, X.-C., Kim, S.-Y., Park, K., Park, E.-J., Jin, X., Yi, S.-M., Kim, Y.-H., Park, C.-H., Song, S. and Kim, H. (2010) 'Asian Dust Storm and pulmonary function of school children in Seoul', *Science of The Total Environment*, 408(4), pp. 754–759.

Hsu, N. C., Tsay, S.-C., King, M. D. and Herman, J. R. (2004) 'Aerosol properties over bright-reflecting source regions', *IEEE Transactions on Geoscience and Remote Sensing*, pp. 557–569.

Huneeus, N., Basart, S., Fiedler, S., Morcrette, J. J., Benedetti, A., Mulcahy, J., Terradellas, E., Pérez García-Pando, C., Pejanovic, G., Nickovic, S., Arsenovic, P., Schulz, M., Cuevas, E., Baldasano, J. M., Pey, J., Remy, S. and Cvetkovic, B. (2016) 'Forecasting the northern African dust outbreak towards Europe in April 2011: A model intercomparison', *Atmospheric Chemistry and Physics*, 16(8), pp. 4967–4986.

Huneeus, N., Schulz, M., Balkanski, Y., Griesfeller, J., Prospero, J., Kinne, S., Bauer, S., Boucher, O., Chin, M., Dentener, F., Diehl, T., Easter, R., Fillmore, D., Ghan, S., Ginoux, P., Grini, A., Horowitz, L., Koch, D., Krol, M. C., Landing, W., Liu, X., Mahowald, N., Miller, R., Morcrette, J.-J., Myhre, G., Penner, J., Perlwitz, J., Stier, P., Takemura, T. and Zender, C. S. (2011) 'Global dust model intercomparison in AeroCom phase I', *Atmospheric Chemistry and Physics*, 11(15), pp. 7781–7816.

Ibrahim, M. M. and El-gaely, G. A. (2012) 'Short-term effects of dust storm on physiological performance of some wild plants in Riyadh , Saudi Arabia', 7(47), pp. 6305–6312.

IPCC (2013) *Climate Change 2013: The Physical Science Basis. Contribution of Working Group I to the Fifth Assessment Report of the Intergovernmental Panel on Climate Change*. Cambridge, United Kingdom and New York.

Iversen, J. D. and White, B. R. (1982) 'Saltation threshold on Earth, Mars and Venus', *Sedimentology*, 29(1), pp. 111–119.

Janjic, Z. I. (1994) 'The step-mountain eta coordinate model: further developments of the convection, viscous sublayer and turbulence closure schemes', *Mon. Wea. Rev*, 122(5), pp. 927–945.

Janjic, Z. I. (1996) 'The surface layer in the NCEP eta model, 11th Conference on Numerical Weather Prediction, Norfolk, VA, 19–23 August 1996; American Meteorological Society, Boston, MA, 354–355'.

Janjic, Z. I. (2000) 'Comments on "Development and evaluation of a convection scheme for use in climate models"', *J. Atmos. Sci.*, 57, pp. 3686–3686.

Janjic, Z. I. (2001) 'Nonsingular Implementation of the Mellor-Yamada Level 2.5 Scheme in the NCEP Meso model', *NOAA/NWS/NCEP Office Note*, 437, p. 61.

Janjic, Z. I. (2009) 'Further development of the unified multiscale Eulerian model for a broad range of spatial and temporal scales within the new National Environmental Modeling System, EGU General Assembly 2009, held 19–24 April 2009, Wien, Austria, abstract EGU2009-1587, 11'.

Janjic, Z. I. and Gall, R. (2012) 'Scientific documentation of the NCEP nonhydrostatic multiscale model on the B grid (NMMB), Part 1 Dynamics, Tech. rep., NCAR/TN-489+STR, doi:10.5065/D6WH2MZX, availabe at: http://nldr.library.ucar. edu/repository/collections/TECH-NOTE-000-000-000-857'.

Jemmett-Smith, B. C., Marsham, J. H., Knippertz, P. and Gilkeson, C. A. (2015) 'Quantifying global dust devil occurrence from meteorological analyses', *Geophysical Research Letters*, 42(4), pp. 1275–1282.

Jiang, H., Farrar, J. T., Beardsley, R. C., Chen, R. and Chen, C. (2009) 'Zonal surface wind jets across the Red Sea due to mountain gap forcing along both sides of the Red Sea', *Geophysical Research Letters*, 36(19), pp. 1–6.

Jickells, T. D., An, Z. S., Andersen, K. K., Baker, A. R., Bergametti, G., Brooks, N., Cao, J. J., Boyd, P. W., Duce, R. A., Hunter, K. A., Kawahata, H., Kubilay, N., LaRoche, J., Liss, P. S., Mahowald, N., Prospero, J. M., Ridgwell, A. J., Tegen, I. and Torres, R. (2005) 'Global Iron Connections Between Desert Dust, Ocean Biogeochemistry, and Climate', *Science*, 308(5718), p. 67 LP-71.

Jish Prakash, P., Stenchikov, G., Kalenderski, S., Osipov, S. and Bangalath, H. (2015) 'The impact of dust storms on the Arabian Peninsula and the Red Sea', *Atmospheric Chemistry and Physics*, 15(1), pp. 199–222.

Jorba, O., Dabdub, D., Blaszczak-Boxe, C., Pérez, C., Janjic, Z., Baldasano, J., Spada, M., Badia, A. and Gonçalves, M. (2012) 'Potential significance of photoexcited NO 2on global air quality with the NMMB/BSC chemical transport model', *Journal of Geophysical Research*, 117(D13), p. D13301.

Kalenderski, S. and Stenchikov, G. (2016) 'High-resolution regional modeling of summertime transport and impact of African dust over the Red Sea and Arabian Peninsula', *Journal of Geophysical Research: Atmospheres*, 121(11), pp. 6435–6458.

Kalenderski, S., Stenchikov, G. and Zhao, C. (2013) 'Modeling a typical winter-time dust event over the Arabian Peninsula and the Red Sea', *Atmospheric Chemistry and Physics*, 13(4), pp. 1999–2014.

Karami, S., Ranjbar, A., Mohebalhojeh, A. R. and Moradi, M. (2017) 'A rare case of haboob in Tehran: Observational and numerical study', *Atmospheric Research*, 185, pp. 169–185.

Kelley, C. P., Mohtadi, S., Cane, M. A., Seager, R. and Kushnir, Y. (2015) 'Climate change in the Fertile Crescent and implications of the recent Syrian drought', *Proceedings of the National Academy of Sciences*, 112(11), pp. 3241–3246.

Kellogg, C. A., Griffin, D. W., Garrison, V. H., Peak, K. K., Royall, N., Smith, R. R. and Shinn, E. A. (2004) 'Characterization of Aerosolized Bacteria and Fungi From Desert Dust Events in Mali, West Africa', *Aerobiologia*, 20(2), pp. 99–110.

Kim, H., Zohaib, M., Cho, E., Kerr, Y. H. and Choi, M. (2017) 'Development and Assessment of the Sand Dust Prediction Model by Utilizing Microwave-Based Satellite Soil Moisture and Reanalysis Datasets in East Asian Desert Areas', *Advances in Meteorology*, 2017(Article ID 1917372), p. 13.

Klein, H., Nickovic, S., Haunold, W., Bundke, U., Nillius, B., Ebert, M., Weinbruch, S., Schuetz, L., Levin, Z., Barrie, L. A. and Bingemer, H. (2010) 'Saharan dust and ice nuclei over Central Europe', *Atmospheric Chemistry and Physics*, 10(21), pp. 10211–10221.

Klingmüller, K., Pozzer, A., Metzger, S., Stenchikov, G. L. and Lelieveld, J. (2016) 'Aerosol optical depth trend over the Middle East', *Atmospheric Chemistry and Physics*, 16(8), pp. 5063–5073.

Klose, M. and Shao, Y. (2013) 'Large-eddy simulation of turbulent dust emission', *Aeolian Research*, 8, pp. 49–58.

Klose, M. and Shao, Y. (2016) 'A numerical study on dust devils with implications to global dust budget estimates', *Aeolian Research*. Elsevier B.V., 22, pp. 47–58.

Knippertz, P., Deutscher, C., Kandler, K., Müller, T., Schulz, O. and Schütz, L. (2007) 'Dust mobilization due to density currents in the Atlas region: Observations from the Saharan Mineral Dust

Experiment 2006 field campaign', *Journal of Geophysical Research*, 112(D21), p. D21109.

Knippertz, P. and Stuut, J.-B. W. (2014) *Mineral Dust: A Key Player in the Easrt System*. Edited by P. Knippertz and J.-B. W. Stuut. Dordrecht: Springer Netherlands.

Knippertz, P. and Todd, M. C. (2012) 'Mineral dust aerosols over the Sahara: Meteorological controls on emission and transport and implications for modeling', *Rev. Geophys.*, 50(RG1007).

Koch, J. and Renno, N. O. (2005) 'The role of convective plumes and vortices on the global aerosol budget', *Geophysical Research Letters*, 32(18), pp. 1–5.

Kocha, C., Tulet, P., Lafore, J. P. and Flamant, C. (2013) 'The importance of the diurnal cycle of Aerosol Optical Depth in West Africa', *Geophysical Research Letters*, 40(4), pp. 785–790.

Kok, J. F. (2011) 'A scaling theory for the size distribution of emitted dust aerosols suggests climate models underestimate the size of the global dust cycle', *Proceedings of the National Academy of Sciences*, 108(3), pp. 1016–1021.

Kumar, R., Barth, M. C., Pfister, G. G., Naja, M. and Brasseur, G. P. (2014) 'WRF-Chem simulations of a typical pre-monsoon dust storm in northern India: Influences on aerosol optical properties and radiation budget', *Atmospheric Chemistry and Physics*, 14(5), pp. 2431–2446.

Lacava, T., Matgen, P., Brocca, L., Bittelli, M., Pergola, N., Moramarco, T. and Tramutoli, V. (2012) 'A First Assessment of the SMOS Soil Moisture Product With In Situ and Modeled Data in Italy and Luxembourg', *IEEE Transactions on Geoscience and Remote Sensing*, pp. 1612–1622.

Lacis, A. A. and Hansen, J. E. (1974) 'A Parameterization for Absorption of Solar Radiation in the Earth's Atmosphere', *Journal of the Atmospheric Sciences*, pp. 118–133.

Lavaysse, C., Flamant, C., Evan, A., Janicot, S. and Gaetani, M. (2016) 'Recent climatological trend of the Saharan heat low and its impact on the West African climate', *Climate Dynamics*. Springer Berlin Heidelberg, 47(11), pp. 3479–3498.

Levy, R. C., Mattoo, S., Munchak, L. A., Remer, L. A., Sayer, A. M., Patadia, F. and Hsu, N. C. (2013) 'The Collection 6 MODIS aerosol products over land and ocean', *Atmospheric Measurement Techniques*, 6(11), pp. 2989–3034.

Levy, R. C., Remer, L. A., Kleidman, R. G., Mattoo, S., Ichoku, C., Kahn, R. and Eck, T. F. (2010) 'Global evaluation of the Collection 5 MODIS dark-target aerosol products over land', *Atmospheric Chemistry and Physics*, 10(21), pp. 10399–10420.

Levy, R., Hsu, C. and Al., E. (2015) 'MODIS Atmosphere L2 Aerosol Product. NASA MODIS Adaptive Processing System, Goddard Space Flight Center, USA: http://dx.doi.org/10.5067/MODIS/MYD04_L2.006 (Aqua)'.

Li, F. and Ramanathan, V. (2002) 'Winter to summer monsoon variation of aerosol optical depth over the tropical Indian Ocean', *Journal of Geophysical Research*, 107, pp. 1–13.

Litvintseva, A. P., Marsden-Haug, N., Hurst, S., Hill, H., Gade, L., Driebe, E. M., Ralston, C., Roe, C., Barker, B. M., Goldoft, M., Keim, P., Wohrle, R., Thompson, G. R., Engelthaler, D. M., Brandt, M. E. and Chiller, T. (2015) 'Valley fever: Finding new places for an old disease: Coccidioides immitis found in Washington state soil associated with recent human infection', *Clinical Infectious Diseases*, 60(1), pp. e1–e3.

Loveland, T. R. and Belward, A. S. (1997) 'The IGBP-DIS global 1km land cover data set, DISCover: First results', *International Journal of Remote Sensing*, 18(15), pp. 3289–3295.

Mamouri, R. E., Ansmann, A., Nisantzi, A., Solomos, S., Kallos, G. and Hadjimitsis, D. G. (2016) 'Extreme dust storm over the eastern Mediterranean in September 2015: Satellite, lidar, and surface observations in the Cyprus region', *Atmospheric Chemistry and Physics*, 16(21), pp. 13711–13724.

Marcella, M. P. and Eltahir, E. A. B. (2014) 'The role of mineral aerosols in shaping the regional climate of West Africa', *Journal of Geophysical Research Atmospheres*, 119(10), pp. 5806–5822.

Marsham, J. H., Dixon, N. S., Garcia-Carreras, L., Lister, G. M. S., Parker, D. J., Knippertz, P. and Birch, C. E. (2013) 'The role of moist convection in the West African monsoon system: Insights from continental-scale convection-permitting simulations', *Geophysical Research Letters*, 40(9), pp. 1843–1849.

Marsham, J. H., Hobby, M., Allen, C. J. T., Banks, J. R., Bart, M., Brooks, B. J., Cavazos-Guerra, C., Engelstaedter, S., Gascoyne, M., Lima, A. R., Martins, J. V., McQuaid, J. B., O'Leary, A., Ouchene, B., Ouladichir, A., Parker, D. J., Saci, A., Salah-Ferroudj, M., Todd, M. C. and Washington, R. (2013) 'Meteorology and dust in the central Sahara: Observations from Fennec supersite-1 during the June 2011 Intensive Observation Period', *Journal of Geophysical Research Atmospheres*, 118(10), pp. 4069–4089.

Marticorena, B. and Bergametti, G. (1995) 'Modeling the atmospheric dust cycle: 1. Design of a soil-derived dust emission scheme', *Journal of Geophysical Research*, 100(D8), p. 16415.

Marticorena, B., Bergametti, G., Aumont, B., Callot, Y., N'Doumé, C. and Legrand, M. (1997) 'Modeling the atmospheric dust cycle: 2. Simulation of Saharan dust sources', *Journal of Geophysical Research: Atmospheres*, 102(D4), pp. 4387–4404.

Marticorena, B., Chatenet, B., Rajot, J. L., Traoré, S., Coulibaly, M., Diallo, A., Koné, I., Maman, A., Ndiaye, T. and Zakou, A. (2010) 'Temporal variability of mineral dust concentrations over West Africa: Analyses of a pluriannual monitoring from the AMMA Sahelian Dust Transect', *Atmospheric Chemistry and Physics*, 10(18), pp. 8899–8915.

McTainsh, G. H. (1989) 'Quaternary aeolian dust processes and sediments in the Australian region', *Quaternary Science Reviews*, 8(3), pp. 235–253.

McTainsh, G. H. and Pitblado, J. R. (1987) 'Dust storms and related phenomena measured from meteorological records in Australia', *Earth Surface Processes and Landforms*, 12(4), pp. 415–424.

Mellor, G. L. and Yamada, T. (1982) 'Development of a turbulence closure model for geophysical fluid problems', *Reviews of Geophysics*, 20(4), p. 851.

Meng, Z. and Lu, B. (2007) 'Dust events as a risk factor for daily hospitalization for respiratory and cardiovascular diseases in Minqin, China', *Atmospheric Environment*, 41(33), pp. 7048–7058.

Menut, L., Pérez, C., Haustein, K., Bessagnet, B., Prigent, C. and Alfaro, S. (2013) 'Impact of surface roughness and soil texture on mineral dust emission fluxes modeling', *Journal of Geophysical Research Atmospheres*, 118(12), pp. 6505–6520.

Miller, S. D., Kuciauskas, A. P., Liu, M., Ji, Q., Reid, J. S., Breed, D. W., Walker, A. L. and Mandoos, A. Al (2008) 'Haboob dust storms of the southern Arabian Peninsula', *Journal of Geophysical Research Atmospheres*, 113(1), pp. 1–26.

MISR Team (2015) 'Terra/MISR Level 3, Component Global Aerosol Yearly, version 4, Hampton, VA, USA: NASA Atmospheric Science Data Center (ASDC)'.

Mlawer, E. J., Taubman, S. J., Brown, P. D., Iacono, M. J. and Clough, S. A. (1997) 'Radiative transfer for inhomogeneous atmospheres: RRTM, a validated correlated-k model for the longwave', *Journal of Geophysical Research*, 102(D14), pp. 16663–16682.

Monin, A. S. and Obukhov, A. M. (1954) 'Basic laws of turbulent mixing in the surface layer of the atmosphere', *Contrib. Geophys. Inst. Acad. Sci. USSR*, 24(151), pp. 163–187.

Morcrette, J.-J., Boucher, O., Jones, L., Salmond, D., Bechtold, P., Beljaars, A., Benedetti, A., Bonet, A., Kaiser, J. W., Razinger, M., Schulz, M., Serrar, S., Simmons, A. J., Sofiev, M., Suttie, M., Tompkins, A. M. and Untch, A. (2009) 'Aerosol analysis and forecast in the European Centre for Medium-Range Weather Forecasts Integrated Forecast System: Forward modeling', *Journal of Geophysical Research*, 114(D06206).

Morman, S. A. and Plumlee, G. S. (2013) 'The role of airborne mineral dusts in human disease', *Aeolian Research*. Elsevier B.V., 9, pp. 203–212.

Mortier, A., Goloub, P., Derimian, Y., Tanré, D., Podvin, T., Blarel, L., Deroo, C., Marticorena, B., Diallo, A. and Ndiaye, T. (2016) 'Climatology of aerosol properties and clear-sky shortwave radiative effects using Lidar and Sun photometer observations in the Dakar site', *Journal of Geophysical Research: Atmospheres*, 121(11), pp. 6489–6510.

Nadh, G. A., Vijay, S. and Gupta, A. (2014) 'Investigation on the Effects of Dust Accumulation, Transmittace on Glass Plates and Performance of Mono and Poly Crystalline Silica Modules', *International Journal of Renewable Energy Research (IJRER)*, 4(3), pp. 628–634.

Nickovic, S., Cvetkovic, B., Madonna, F., Rosoldi, M., Pejanovic, G., Petkovic, S. and Nikolic, J. (2016) 'Cloud ice caused by atmospheric mineral dust-Part 1: Parameterization of ice nuclei concentration in the NMME-DREAM model', *Atmospheric Chemistry and Physics*, 16(17), pp. 11367–11378.

Nickovic, S., Kallos, G., Papadopoulos, A. and Kakaliagou, O. (2001) 'A model for prediction of desrt dust cycle in the atmosphere', *Journal of Geophysical Research*, 106, p. 18113.

Notaro, M., Yu, Y. and Kalashnikova, O. V. (2015) 'Regime shift in Arabian dust activity, triggered by persistent Fertile Crescent drought', *Journal of Geophysical Research: Atmospheres*, 120(19), pp. 10229–10249.

Ortiz-Martínez, M. G., Rodríguez-cotto, R. I., Ortiz-rivera, M. A., Pluguez-turull, C. W. and Jiménez-vélez, B. D. (2015) 'Linking Endotoxins , African Dust PM10 and Asthma in an Urban and Rural Environment of Puerto Rico', *Mediators of Inflammation*, 2015(Article ID 784212), p. 14.

Otani, S., Onishi, K., Mu, H., Yokoyama, Y., Hosoda, T., Okamoto, M. and Kurozawa, Y. (2012) 'The relationship between skin symptoms and allergic reactions to Asian dust', *International Journal of Environmental Research and Public Health*, 9(12), pp. 4606–4614.

Otto, S., de Reus, M., Trautmann, T., Thomas, A., Wendisch, M. and Borrmann, S. (2007) 'Atmospheric radiative effects of an in situ measured Saharan dust plume and the role of large particles', *Atmospheric Chemistry and Physics*, 7(18), pp. 4887–4903.

Pandolfi, M., Martucci, G., Querol, X., Alastuey, A., Wilsenack, F., Frey, S., O'Dowd, C. D. and Dall'Osto, M. (2013) 'Continuous atmospheric boundary layer observations in the coastal urban area of Barcelona during SAPUSS', *Atmospheric Chemistry and Physics*, 13(9), pp. 4983–4996.

Pantillon, F., Knippertz, P., Marsham, J. and Birch, C. (2015) 'A parameterization of convective dust storms for models with mass-flux convection schemes', *Journal of the Atmospheric Sciences*, (2014), p. 150407121742006.

Papayannis, A., Balis, D., Amiridis, V., Chourdakis, G., Tsaknakis, G., Zerefos, C., Castanho, A. D., Nickovic, S., Kazadzis, S. and Grabowski, J. (2005) 'Measurements of Saharan dust aerosols over the Eastern Mediterranean using elastic backscatter-Raman lidar, spectrophotometric and satellite observations in the frame of the EARLINET project', *Atmospheric Chemistry and Physics Discussions*, 5(2), pp. 2075–2110.

Parker, D. J., Burton, R. R., Diongue-Niang, A., Ellis, R. J., Felton, M., Taylor, C. M., Thorncroft, C. D., Bessemoulin, P. and Tompkins, A. M. (2005) 'The diurnal cycle of the West African monsoon circulation', *Quarterly Journal of the Royal Meteorological Society*. John Wiley & Sons, Ltd., 131(611), pp. 2839–2860.

Parolari, A. J., Li, D., Bou-Zeid, E., Katul, G. G. and Assouline, S. (2016) 'Climate, not conflict, explains extreme Middle East dust storm', *Environmental Research Letters*, 11(114013), pp. 1–8.

Pérez, C., Haustein, K., Janjic, Z., Jorba, O., Huneeus, N., Baldasano, J. M., Black, T., Basart, S., Nickovic, S., Miller, R. L., Perlwitz, J. P., Schulz, M. and Thomson, M. (2011) 'Atmospheric dust modeling from meso to global scales with the online NMMB/BSC-Dust model - Part 1: Model description, annual simulations and evaluation', *Atmospheric Chemistry and Physics*, 11(24), pp. 13001–13027.

Pérez, C., Nickovic, S., Pejanovic, G., Baldasano, J. M. and Özsoy, E. (2006) 'Interactive dust-

radiation modeling: A step to improve weather forecasts', *Journal of Geophysical Research Atmospheres*, 111(D16206).

Pérez García-Pando, C., Stanton, M. C., Diggle, P. J., Trzaska, S., Miller, R. L., Perlwitz, J. P., Baldasano, J. M., Cuevas, E., Ceccato, P., Yaka, P. and Thomson, M. C. (2014) 'Soil dust aerosols and wind as predictors of seasonal meningitis incidence in niger', *Environmental Health Perspectives*, 122(7), pp. 679–686.

Pey, J., Querol, X., Alastuey, A., Forastiere, F. and Stafoggia, M. (2013) 'African dust outbreaks over the Mediterranean Basin during 2001-2011: PM10 concentrations, phenomenology and trends, and its relation with synoptic and mesoscale meteorology', *Atmospheric Chemistry and Physics*, 13(3), pp. 1395–1410.

Pope, R. J., Marsham, J. H., Knippertz, P., Brooks, M. E. and Roberts, A. J. (2016) 'Identifying errors in dust models from data assimilation', *Geophysical Research Letters*, 43(17), pp. 9270–9279.

Prospero, J. M. (1996) 'Saharan dust transport over the North Atlantic Ocean and Mediterranean: An overview', *Impact of Desert Dust across the Mediterranean*, pp. 133–151.

Prospero, J. M. (2002) 'Environmental characterization of global sources of atmospheric soil dust identified with the NIMBUS 7 Total Ozone Mapping Spectrometer (TOMS) absorbing aerosol product', *Reviews of Geophysics*, 40(1), p. 1002.

Prospero, J. M. (2003) 'African Droughts and Dust Transport to the Caribbean: Climate Change Implications', *Science*, 302(5647), pp. 1024–1027.

Redl, R., Fink, A. H. and Knippertz, P. (2015) 'An Objective Detection Method for Convective Cold Pool Events and Its Application to Northern Africa', *Monthly Weather Review*, 143(12), pp. 5055–5072.

Reinfried, F., Tegen, I., Heinold, B., Hellmuth, O., Schepanski, K., Cubasch, U., Huebener, H. and Knippertz, P. (2009) 'Simulations of convectively-driven density currents in the Atlas region using a regional model: Impacts on dust emission and sensitivity to horizontal resolution and convection schemes', *Journal of Geophysical Research Atmospheres*, 114(8), pp. 1–13.

Remer, L. a., Tanré, D., Kaufman, Y. J., Ichoku, C., Mattoo, S., Levy, R. C., Chu, D. A., Holben, B., Dubovik, O., Smirnov, A., Martins, J. V., Li, R.-R. and Ahmad, Z. (2002) 'Validation of MODIS aerosol retrieval over ocean', *Geophysical Research Letters*, 29(12), pp. 2–5.

Rezazadeh, M., Irannejad, P. and Shao, Y. (2013) 'Climatology of the Middle East dust events', *Aeolian Research*. Elsevier B.V., 10, pp. 103–109.

Ridley, D. A., Heald, C. L. and Ford, B. (2012) 'North African dust export and deposition: A satellite and model perspective', *Journal of Geophysical Research: Atmospheres*, 117(D02202), pp. 1–21.

Rieger, D., Bangert, M., Bischoff-Gauss, I., Förstner, J., Lundgren, K., Reinert, D., Schröter, J., Vogel, H., Zängl, G., Ruhnke, R. and Vogel, B. (2015) 'ICON-ART 1.0 - A new online-coupled model system from the global to regional scale', *Geoscientific Model Development*, 8(6), pp. 1659–1676.

Rodríguez, S., Alastuey, A., Alonso-Pérez, S., Querol, X., Cuevas, E., Abreu-Afonso, J., Viana, M., Pérez, N., Pandolfi, M. and de la Rosa, J. (2011) 'Transport of desert dust mixed with North African industrial pollutants in the subtropical Saharan Air Layer', *Atmospheric Chemistry and Physics*, 11(13), pp. 6663–6685.

Rodríguez, S., Querol, X., Alastuey, A., Kallos, G. and Kakaliagou, O. (2001) 'Saharan dust contributions to PM10 and TSP levels in Southern and Eastern Spain', *Atmospheric Environment*, 35(14), pp. 2433–2447.

Rüdiger, C., Walker, J. P., Kerr, Y. H., Kim, E. J., Hacker, J. M., Gurney, R. J., Barrett, D. and Marshall, J. L. (2014) 'Toward Vicarious Calibration of Microwave Remote-Sensing Satellites in Arid Environments', *IEEE Transactions on Geoscience and Remote Sensing*, pp. 1749–1760.

Ryder, C. L., Highwood, E. J., Lai, T. M., Sodemann, H. and Marsham, J. H. (2013) 'Impact of

atmospheric transport on the evolution of microphysical and optical properties of Saharan dust', *Geophysical Research Letters*, 40(10), pp. 2433–2438.

Schepanski, K., Tegen, I., Laurent, B., Heinold, B. and Macke, A. (2007) 'A new Saharan dust source activation frequency map derived from MSG-SEVIRI IR-channels', *Geophysical Research Letters*, 34(18), pp. 1–5.

Schepanski, K., Tegen, I. and Macke, A. (2012) 'Comparison of satellite based observations of Saharan dust source areas', *Remote Sensing of Environment*, 123, pp. 90–97.

Schepanski, K., Tegen, I., Todd, M. C., Heinold, B., Bönisch, G., Laurent, B. and Macke, A. (2009) 'Meteorological processes forcing Saharan dust emission inferred from MSG-SEVIRI observations of subdaily dust source activation and numerical models', *Journal of Geophysical Research*, 114(D10201), pp. 1–18.

Schmetz, J., Pili, P., Tjemkes, S., Just, D., Kerkmann, J., Rota, S. and Ratier, A. (2002) 'An introduction to Meteosat Second Generation (MSG)', *Bulletin of the American Meteorological Society*, 83(7), pp. 977–992.

Schroedter-Homscheidt, M., Oumbe, A., Benedetti, A. and Morcrette, J. J. (2013) 'Aerosols for concentrating solar electricity production forecasts: Requirement quantification and ECMWF/MACC aerosol forecast assessment', *Bulletin of the American Meteorological Society*, 94(6), pp. 903–914.

Schulz, M., Balkanski, Y. J., Guelle, W. and Dulac, F. (1998) 'Role of aerosol size distribution and source location in a three-dimensional simulation of a Saharan dust episode tested against satellite-derived optical thickness', *Journal of Geophysical Research: Atmospheres*, 103(D9), pp. 10579–10592.

Seinfeld, J. H. and Pandis, S. N. (2016) *Atmospheric Chemistry and Physics: From Air Pollution to Climate Change*. New York: John Wiley and Sons.

Shao, Y. (2008) *Erosion, Physics and Modelling of Wind*. Springer Netherlands.

Shao, Y., Wyrwoll, K. H., Chappell, A., Huang, J., Lin, Z., McTainsh, G. H., Mikami, M., Tanaka, T. Y., Wang, X. and Yoon, S. (2011) 'Dust cycle: An emerging core theme in Earth system science', *Aeolian Research*. Elsevier B.V., 2(4), pp. 181–204.

Shettle, E. P. (1986) 'Optical and radiative properties of a desert aerosol model, in: Presented at the International Radiation', in *Symposium on Current Problems in Atmospheric Radiation*. Perugia, Italy, 1984.

Shirkhani-Ardehjani, S. (2012) 'I.R. of Iran National Report on Regional Action Plan to combat dust and sand storm', in *International Cooperative for Aerosol Prediction (ICAP) 4th Workshop: Aerosol Emission and Removal Processes*. Frascati, Italy: ESA/ESRIN.

Simmons, A. J. and Burridge, D. M. (1981) 'An Energy and Angular-Momentum Conserving Vertical Finite-Difference Scheme and Hybrid Vertical Coordinates', *Monthly Weather Review*, pp. 758–766.

Slinn, W. G. N. (1982) 'Predictions for particle deposition to vegetative canopies', *Atmospheric Environment (1967)*, 16(7), pp. 1785–1794.

Slinn, W. G. N. (1984) *Precipitation Scavenging*. OSTI. Edited by D. Randerson. Oak Ridge: Atmospheric Science and Power Production.

Smirnov, A., Holben, B. N., Eck, T. F., Dubovik, O. and Slutsker, I. (2000) 'Cloud-Screening and Quality Control Algorithms for the AERONET Database', *Remote Sensing of Environment*, 73(3), pp. 337–349.

Smith, D. J., Griffin, D. W., McPeters, R. D., Ward, P. D. and Schuerger, A. C. (2011) 'Microbial survival in the stratosphere and implications for global dispersal', *Aerobiologia*, 27(4), pp. 319–332.

Smith, D. J., Timonen, H. J., Jaffe, D. A., Griffin, D. W., Birmele, M. N., Perry, K. D., Ward, P. D. and Roberts, M. S. (2013) 'Intercontinental dispersal of bacteria and archaea by transpacific winds', *Applied and Environmental Microbiology*, 79(4), pp. 1134–1139.

Solomos, S., Ansmann, A., Mamouri, R., Binietoglou, I. and Patlakas, P. (2017) 'Remote sensing and modelling analysis of the extreme dust storm hitting the Middle East and eastern Mediterranean in September 2015', 17, pp. 4063–4079.

Solomos, S., Kallos, G., Mavromatidis, E. and Kushta, J. (2012) 'Density currents as a desert dust mobilization mechanism', *Atmospheric Chemistry and Physics*, 12(22), pp. 11199–11211.

Spada, M., Jorba, O., Pérez García-Pando, C., Janjic, Z. and Baldasano, J. M. (2015) 'On the evaluation of global sea-salt aerosol models at coastal/orographic sites', *Atmospheric Environment*, 101, pp. 41–48.

Spada, M., Jorba, O., Pérez García-Pando, C., Janjic, Z. and M. Baldasano, J. (2013) 'Modeling and evaluation of the global sea-salt aerosol distribution: sensitivity to emission schemes and resolution effects at coastal/orographic sites', *Atmospheric Chemistry and Physics*, 13(23), pp. 11735–11755.

Sprigg, W. A., Nickovic, S., Galgiani, J. N., Pejanovic, G., Petkovic, S., Vujadinovic, M., Vukovic, A., Dacic, M., DiBiase, S., Prasad, A. and El-Askary, H. (2014) 'Regional dust storm modeling for health services: The case of valley fever', *Aeolian Research*, 14, pp. 53–73.

Stanelle, T., Bey, I., Raddatz, T., Reick, C. and Tegen, I. (2014) 'Anthropogenically induced changes in twentieth century mineral dust burden and the associated impact on radiative forcing', *Journal of Geophysical Research : Atmospheres*, 119(13), pp. 526–546.

Stefanski, R. and Sivakumar, M. V. K. (2009) 'Impacts of sand and dust storms on agriculture and potential agricultural applications of a SDSWS', in *IOP Conference Series: Earth and Environmental Science*.

Stephens, G. L., L'Ecuyer, T., Forbes, R., Gettlemen, A., Golaz, J. C., Bodas-Salcedo, A., Suzuki, K., Gabriel, P. and Haynes, J. (2010) 'Dreary state of precipitation in global models', *Journal of Geophysical Research Atmospheres*, 115(24), pp. 1–14.

Strong, C. L., Parsons, K., McTainsh, G. H. and Sheehan, A. (2011) 'Dust transporting wind systems in the lower Lake Eyre Basin, Australia: A preliminary study', *Aeolian Research*, 2(4), pp. 205–214.

Su, J., Huang, J., Fu, Q., Minnis, P., Ge, J. and Bi, J. (2008) 'Estimation of Asian dust aerosol effect on cloud radiation forcing using Fu-Liou radiative model and CERES measurements', *Atmospheric Chemistry and Physics Discussions*, 8(1), pp. 2061–2084.

Sutton, L. J. (1925) 'Haboobs', *Quarterly Journal of the Royal Meteorological Society*. John Wiley & Sons, Ltd, 51(213), pp. 25–30.

Takemi, T. (1999) 'Structure and Evolution of a Severe Squall Line over the Arid Region in Northwest China', *Monthly Weather Review*, 127(6), pp. 1301–1309.

Takemi, T. (2005) 'Explicit Simulations of Convective-Scale Transport of Mineral Dust in Severe Convective Weather', *Journal of the Meteorological Society of Japan*, 83A, pp. 187–203.

Tegen, I., Harrison, S. P., Kohfeld, K., Prentice, I. C., Coe, M. and Heimann, M. (2002) 'Impact of vegetation and preferential source areas on global dust aerosol: Results from a model study', *Journal of Geophysical Research Atmospheres*, 107(D21), p. 4576.

Tegen, I. and Lacis, A. A. (1996) 'Modeling of particle size distribution and its influence on the radiative properties of mineral dust aerosol', *Journal of Geophysical Research: Atmospheres*, 101(D14), pp. 19237–19244.

Tegen, I., Schepanski, K. and Heinold, B. (2013) 'Comparing two years of Saharan dust source activation obtained by regional modelling and satellite observations', *Atmospheric Chemistry and Physics*, 13(5), pp. 2381–2390.

Teller, A. and Levin, Z. (2005) 'The effects of aerosols on precipitation and dimensions of subtropical clouds; a sensitivity study using a numerical cloud model', *Atmospheric Chemistry and Physics Discussions*, 5(4), pp. 7211–7245.

Thalib, L. and Al-Taiar, A. (2012) 'Dust storms and the risk of asthma admissions to hospitals in

Kuwait', *Science of The Total Environment*, 433, pp. 347–351.

Thomson, M. C., Molesworth, A. M., Djingarey, M. H., Yameogo, K. R., Belanger, F. and Cuevas, L. E. (2006) 'Potential of environmental models to predict meningitis epidemics in Africa', *Tropical Medicine and International Health*, 11(6), pp. 781–788.

Todd, M. C. and Cavazos-Guerra, C. (2016) 'Dust aerosol emission over the Sahara during summertime from Cloud-Aerosol Lidar with Orthogonal Polarization (CALIOP) observations', *Atmospheric Environment*, 128, pp. 147–157.

Todd, M. C., Washington, R., Raghavan, S., Lizcano, G. and Knippertz, P. (2008) 'Regional model simulations of the Bodélé low-level jet of Northern Chad during the Bodélé dust experiment (BoDEx 2005)', *Journal of Climate*, 21(5), pp. 995–1012.

Di Tomaso, E., Schutgens, N. A. J., Jorba, O. and García-Pando, C. P. (2017) 'Assimilation of MODIS Dark Target and Deep Blue observations in the dust aerosol component of NMMB-MONARCH version 1.0', *Geoscientific Model Development*, 10(3), pp. 1107–1129.

Tsamalis, C., Chédin, A., Pelon, J. and Capelle, V. (2013) 'The seasonal vertical distribution of the saharan air layer and its modulation by the wind', *Atmospheric Chemistry and Physics*, 13(22), pp. 11235–11257.

Vickery, K. J., Eckardt, F. D. and Bryant, R. G. (2013) 'A sub-basin scale dust plume source frequency inventory for southern Africa, 2005-2008', *Geophysical Research Letters*, 40(19), pp. 5274–5279.

Vinoj, V., Rasch, P. J., Wang, H., Yoon, J.-H., Ma, P.-L., Landu, K. and Singh, B. (2014) 'Short-term modulation of Indian summer monsoon rainfall by West Asian dust', *Nature Geosci*. Nature Publishing Group, 7(4), pp. 308–313.

Vukovic, A., Rajkovic, B. and Janjic, Z. (2010) 'Land Ice Sea Surface Model: Short Description and Verification', *2010 International Congress on Environmental Modelling and Software Modelling for Environment's Sake, Fifth Biennial Meeting, Ottawa, Canada, 5–8 July 2010*.

Vukovic, A., Vujadinovic, M., Pejanovic, G., Andric, J., Kumjian, M. R., Djurdjevic, V., Dacic, M., Prasad, A. K., El-Askary, H. M., Paris, B. C., Petkovic, S., Nickovic, S. and Sprigg, W. A. (2014) 'Numerical simulation of "an American haboob"', *Atmospheric Chemistry and Physics*, 14(7), pp. 3211–3230.

Wang, R., Balkanski, Y., Bopp, L., Aumont, O., Boucher, O., Ciais, P., Gehlen, M., Peñuelas, J., Ethé, C., Hauglustaine, D., Li, B., Liu, J., Zhou, F. and Tao, S. (2015) 'Anthropogenic aerosol deposition reduces the sensitivity of oceanic productivity to warming', *Geophysical Research Letters*, 42, p. 10,745–10,754.

Wang, W., Evan, A., Flamant, C. and Lavaysse, C. (2015) 'On the Decadal Scale Correlation between African Dust and Sahel Rainfall: the Role of Saharan Heat Low-Forced Winds', *Science Advances*, 1(e1500646), pp. 1–5.

White, B. R. (1979) 'soil transport by winds on Mars', *Journal of Geophysical Research*, 84, pp. 4643–4651.

WHO (2005) *WHO air quality guidelines global update 2005, Report on a working group meeting*. Bonn, Germany.

Wijayratne, U. C., Scoles-Sciulla, S. J. and Defalco, L. a. (2009) 'Dust Deposition Effects on Growth and Physiology of the Endangered Astragalus jaegerianus (Fabaceae)', *Madroño*, 56(2), pp. 81–88.

Xi, X. and Sokolik, I. N. (2016) 'Quantifying the anthropogenic dust emission from agricultural land use and desiccation of the Aral Sea in Central Asia', *Journal of Geophysical Research: Atmospheres*, 121, p. 12,270-12,281.

Yamauchi, M. (2012) 'Secondary wind transport of radioactive materials after the Fukushima accident', *Earth, Planets and Space*, 64(1), pp. e1–e4.

Yu, H., Chin, M., Yuan, T., Bian, H., Remer, L. A., Prospero, J. M., Omar, A., Winker, D., Yang, Y.,

Zhang, Y., Zhang, Z. and Zhao, C. (2015) 'The fertilizing role of African dust in the Amazon rainforest: A first multiyear assessment based on data from Cloud-Aerosol Lidar and Infrared Pathfinder Satellite Observations', *Geophysical Research Letters*, 42(6), pp. 1984–1991.

Zender, C. S., Bian, H. and Newman, D. (2003) 'Mineral Dust Entrainment and Deposition (DEAD) model: Description and 1990s dust climatology', *Journal of Geophysical Research*, 108(D14), pp. 1–19.

Zhang, L., Gong, S., Padro, J. and Barrie, L. (2001) 'A size-segregated particle dry deposition scheme for an atmospheric aerosol module', *Atmospheric Environment*, 35(3), pp. 549–560.

Zhang, X., Zhao, L., Tong, D., Wu, G., Dan, M. and Teng, B. (2016) 'A Systematic Review of Global Desert Dust and Associated Human Health Effects', *Atmosphere*, 7(158), pp. 1–30.

List of Figures

List of Tables